IVW - Schriftenreihe Band 103
Institut für Verbundwerkstoffe GmbH - Kaiserslautern

Ruijuan Zhou

Nanoparticle-Filled Thermoplastics and Thermoplastic Elastomer: Structure-Property Relationships

Bibliografische Information Der Deutschen Bibliothek

Die Deutsche Bibliothek verzeichnet diese Publikation in der Deutschen Nationalbibliografie; detaillierte bibliografische Daten sind im Internet über <http://dnb.ddb.de> abrufbar.

Bibliographic information published by Die Deutsche Bibliothek

Die Deutsche Bibliothek lists this publication in the Deutsche Nationalbibliografie; detailed bibliographic data is available in the Internet at <http://dnb.ddb.de>.

Herausgeber: Institut für Verbundwerkstoffe GmbH
Prof. Dr.-Ing. Ulf Breuer
Erwin-Schrödinger-Straße
TU Kaiserslautern, Gebäude 58
67663 Kaiserslautern
http://www.ivw.uni-kl.de

Verlag: Institut für Verbundwerkstoffe GmbH

Druck: Technische Universität Kaiserslautern
ZBT – Abteilung Foto-Repro-Druck

D 386

Als Manuskript gedruckt. Printed in Germany.
ISSN 1615-021X
ISBN 978-3-934930-99-5

Nanoparticle-Filled Thermoplastics and Thermoplastic Elastomer:

Structure-Property Relationships

Vom Fachbereich für Maschinenbau und Verfahrenstechnik
der Technischen Universität Kaiserslautern
zur Verleihung des akademischen Grades

Doktor-Ingenieur (Dr.-Ing.)

genehmigte Dissertation
von
Dipl.-Chem. Ruijuan Zhou
aus Weifang, China

Tag der mündlichen Prüfung: 09. Juli 2012

Prüfungsvorsitzender:	Prof. Dr.-Ing. Paul L. Geiß
1. Berichterstatter:	Prof. Dr.-Ing. Martin Maier
2. Berichterstatter:	Prof. Dr. rer. nat. Werner R. Thiel

Acknowledgements

The present work was completed between July 2007 and Mai 2011 at the Institute for Composite Materials (Institut für Verbundwerkstoffe GmbH in Kaiserslautern, IVW) of the Technical University of Kaiserslautern, Germany.

First and foremost, I would like to express my special gratitude to my supervisor Prof. Dr.-Ing. Martin Maier for his kind support on my work. Especially I would like to express my appreciation for the scientific support and constant interest to Dr. rer. nat. Thomas Burkhart. Our fruitful discussions on polymer science and technology during my PhD work at IVW broadened my knowledge and enlightened the perspectives in this field. I am very thankful to Prof. Dr. rer. nat. Werner R. Thiel for accepting the examination of this PhD thesis. I would also like to extend my gratitude to Prof. Dr.-Ing. Paul L. Geiß for accepting the presidency of the examination committee.

I would like to thank the German Science Foundation (DFG) for the financial support. I am very grateful to IVW for providing me the opportunity of working in an outstanding environment from the scientific and technical point of view. The support of the colleagues at the IVW is grateful acknowledged during my work. Many thanks to Mr. Rolf Walter, Dr. Nicole Knör, Miss Irene Hassinger, Mr. Hermann Giertzsch, Mrs. Pia Eichert, Mr. Ralf Schimmele and to all other colleagues for their kind help and support. I also gratefully thank Prof. Dr.–Ing. Alois K. Schlarb for his support on my work.

Many thanks to Zhong Nan for his contribution to this research work.

I would like to convey my special thanks to my parents and my friends who constantly supported and encouraged me during my PhD work.

Abstract

The present work focuses on the structure-property relationships of particulate-filled thermoplastics and thermoplastic elastomer (TPE). In this work two thermoplastics and one TPE were used as polymer matrices, i.e. amorphous bisphenol-A polycarbonate (PC), semi-crystalline isotactic polypropylene (iPP), and a block copolymer poly(butylene terephthalate)-block-poly(tetramethylene glycol) TPE(PBT-PTMG). For PC, a selected type of various Aerosil® nano-SiO_2 types was used as filler to improve the thermal and mechanical properties by maintaining the transparency of PC matrix. Different types of SiO_2 and TiO_2 nanoparticles with different surface polarity were used for iPP. The goal was to examine the influence of surface polarity and chemical nature of nanoparticles on the thermal, mechanical and morphological properties of iPP composites. For TPE(PBT-PTMG), three TiO_2 particles were used, i.e. one grade with hydroxyl groups on the particle surface and the other two grades are surface-modified with metal and metal oxides, respectively. The influence of primary size and dispersion quality of TiO_2 particles on the properties of TPE(PBT-PTMG)/TiO_2 composites were determined and discussed.

All polymer composites were produced by direct melt blending in a twin-screw extruder via masterbatch technique. The dispersion of particles was examined by using scanning electron microscopy (SEM) and micro-computerized tomography (μCT). The thermal and crystalline properties of polymer composites were

characterized by using thermogravimetric analysis (TGA) and differential scanning calorimetry (DSC). The mechanical and thermomechanical properties were determined by using mechanical tensile testing, compact tension and Charpy impact as well as dynamic-mechanical thermal analysis (DMTA).

The SEM results show that the unpolar-surface modified nanoparticles are better dispersed in polymer matrices as iPP than polar-surface nanoparticles, especially in case of using Aeroxide® TiO_2 nanoparticles. The Aeroxide® TiO_2 nanoparticles with a polar surface due to Ti-OH groups result in a very high degree of agglomeration in both iPP and TPE matrices because of strong van der Waals interactions among particles (hydrogen bonding). Compared to unmodified Aeroxide® TiO_2 nanoparticles, the other grades of surface modified TiO_2 particles are very homogenously dispersed in used iPP and TPE(PBT-PTMG). The incorporation of SiO_2 nanoparticles into bisphenol-A PC significantly increases the mechanical properties of PC/SiO_2 nanocomposites, particularly the resistance against environmental stress crazing (ESC). However, the transparency of PC/SiO_2 nanocomposites decreases with increasing nanoparticle content and size due to a mismatch of infractive indices of PC and SiO_2 particles. The different surface polarity of nanoparticles in iPP shows evident influence on properties of iPP composites. Among iPP/SiO_2 nanocomposites, the nanocomposite containing SiO_2 nanoparticles with a higher degree of hydrophobicity shows improved fracture and impact toughness compared to the other iPP/SiO_2 composites. The TPE(PBT-PTMG)/TiO_2 composites show much better thermal

and mechanical properties than neat TPE(PBT-PTMG) due to strong chemical interactions between polymer matrix and TiO_2 particles. In addition, better dispersion quality of TiO_2 particles in used TPE(PBT-PTMG) leads to dramatically improved mechanical properties of TPE(PBT-PTMG)/TiO_2 composites.

Kurzfassung

Die vorliegende Arbeit beschäftigt sich mit den Struktur-Eigenschafts-Beziehungen von mit sphärischen Nanopartikeln gefüllten Thermoplasten und thermoplastischen Elastomeren (TPE). In dieser Arbeit wurden zwei verschiedene Thermoplaste und ein TPE als Polymermatrix ausgewählt: ein amorphes Bisphenol-A Polycarbonat (PC), ein teil-kristallines, isotaktisches Polypropylen (iPP) und ein Blockcopolymer Poly(butylenterephthalat)-block-poly(tetramethylenglykol) (PBT-PTMG) Polymer. In PC wurden SiO_2 Nanopartikel eincompoundiert, um die thermischen und mechanischen Eigenschaften der Matrix - unter Beibehaltung der Transparenz - zu erhöhen. Unterschiedliche Typen von SiO_2 und TiO_2 Nanopartikel mit unterschiedlicher Oberflächenpolarität wurden in iPP eingesetzt. Das Ziel war es, den Einfluss von Partikelzugabe, Oberflächenpolarität, sowie chemischem Eigenschaftsprofil der Partikel auf die thermischen und mechanischen Eigenschaften von iPP zu analysieren. Für TPE(PBT-PTMG) wurden drei Typen von TiO_2 Partikel eingesetzt, davon eine Type mit Hydroxylgruppen (OH-Gruppen) auf der Partikeloberfläche, die anderen zwei Typen sind oberflächenmodifiziert mit Metallen/Metalloxiden bzw. Polyalkoholen. Der Einfluss von primärer Partikelgröße und Dispergierqualität der Partikel auf die Eigenschaften von TPE(PBT-PTMG)/TiO_2 Kompositen wurde studiert und diskutiert.

Alle Komposite wurden über Doppelschneckenextrusion, dem sogenannten Masterbatch-Verfahren, hergestellt. Die Dispergierqualität von Partikeln in dem

jeweiligen Polymer wurde über Rasterelektronenmikroskopie (REM) und Mikro-Computertomograf (µCT) untersucht. Die thermischen Eigenschaften, sowie die Kristallinität der hergestellten Komposite wurden mittels Thermogravimetrie (TGA) und dynamischer Differenzkalorimetrie (DSC) charakterisiert. Die Bestimmung der mechanischen und thermomechanischen Eigenschaften der polymeren Komposite erfolgte unter anderem durch quasistatische Zugversuche, Compact Tension (CT), Schlagzähigkeitsversuche und dynamisch-mechanisch- thermische Analyse (DMTA).

Das Ergebnis der REM Untersuchungen zeigte, dass im Falle von TiO_2 die oberflächenmodifizierten Nanopartikel besser in polymere Matrices z.B. TPE(PBT-PTMG) eindispergiert werden können als die nicht oberflächenmodifizierten Nanopartikel; dies besonders im Falle von Aeroxide® TiO_2 Nanopartikeln. Die nicht modifizierten Aeroxide® TiO_2 Partikel weisen aufgrund von starken Van der Waals Wechselwirkungen (H-Brücken), starke Agglomerationen auf, sowohl in iPP als auch in TPE(PBT-PTMG). Im Gegensatz dazu liegen die modifizierten TiO_2 Partikel sehr homogen in iPP und TPE(PBT-PTMG) dispergiert vor. Die Zugabe von SiO_2 Nanopartikel in PC führte zu einer signifikanten Erhöhung der mechanischen Eigenschaften von PC/SiO_2 Nanokompositen, besonders wurde die Spannungsrissbeständigkeit von PC erheblich verbessert. Jedoch wurde die Transparenz von PC/SiO_2 Kompositen nach der Partikelzugabe wegen nicht optimal passender Berechungszahlen von beiden Phasen vermindert. Die Oberflächenpolarität von Nanopartikel in iPP

zeigte einen deutlichen Einfluss auf die mechanischen Eigenschaften von iPP Komposite. Die iPP/SiO_2 Komposite, bei welchen die SiO_2 Partikel eine höhere Hydrophobizität aufweisen, zeigen eine bedeutend höhere Bruchzähigkeit und Schlagzähigkeit als die iPP/SiO_2 Komposite, bei welchen hydrophilere SiO_2-Typen eingesetzt wurden. Die TPE(PBT-PTMG)/TiO_2 Komposite zeigen im Vergleich zu reinem TPE(PBT-PTMG) aufgrund chemischer Wechselwirkungen zwischen Matrix und TiO_2 Partikeln deutlich verbesserte thermische und mechanische Eigenschaften. Die bessere Dispergierqualität von TiO_2 Partikeln in TPE(PBT-PTMG) führte zu einer signifikanten Erhöhung der mechanischen Eigenschaften von TPE(PBT-PTMG)/TiO_2 Komposite.

List of Abbreviations and Symbols

Abbreviations

Al	Aluminium
Al_2O_3	Aluminium oxide
Au	Gold
CNT	Carbon nanotube
Cu	Copper
DSC	Differential scanning calorimetry
DMTA	Dynamic mechanical thermal analysis
ESC	Environmental stress crazing
Fe	Iron
PA	Polyamide
PBT	Poly(butylene terephthalate)
PC	Polycarbonate
PE	Polyethylene
PET	Poly(ethylene terephthalate)
PMMA	Poly(methyl methacrylate)
PP	Polypropylene
PS	Polystyrene
PTMG	Poly(tetramethylene glycol)
rpm	Revolution per minute
SiO_2	Silicon dioxide
SEM	Scanning electron microscopy
TiO_2	Titanium dioxide
TGA	Thermogravimetric analysis
TPE	Thermoplastic elastomer
TTS	Time temperature superposition

WLF	Williams-Landel-Ferry
Vol.-%	Volume fraction

Symbols

a_T	[1]	Shift factor
C	[1]	Constant factor
D	[mm]	Diameter
E*	[MPa]	Complex modulus
E', E"	[MPa]	Storage- and loss modulus
G_{IC}	[kJ·m^{-2}]	Energy release rate
ΔH	[kJ/mol]	Crystalline enthalpy
J	[GPa^{-1}]	Creep compliance
K_{IC}	[MPa·m$^{1/2}$]	specific fracture toughness
L	[mm]	Length
L/D	[1]	Length/diameter ratio
n	[1]	Refractive index
R	[J·K^{-1}·mol^{-1}]	Universal gas constant
r	[mm]	Radius
T, T_0	[°C]	Actual- and reference temperature
T_g, T_c	[°C]	Glass transition- and crystalline temperature
T_m	[°C]	Melting temperature
t	[s]	Time
tanδ	[1]	Mechanical loss factor
X_c	[%]	Crystallinity

Greek symbols

ε	[%]	Strain
σ	[MPa]	Stress
δ	[1]	Phase angle shift

γ	[mN/m]	Surface tension
φ_f	[Vol.-%]	Volume fraction of fillers
φ_e	[Vol.-%]	Effective volume fraction of fillers
Φ	[1]	Light flux
v	[1]	Poisson's ratio

1 State of the Art

1.1 Introduction

Since the first commercial hybrids polyamide 6 nanocomposites were developed in the mid 80's by Toyota research group [1], the development of polymer nanocomposites is rapidly increasing by potential applications in different industry sectors. Nowadays, polymer-based composites have attracted great attention in both industry and academia. Polymers can be modified with different fillers, which enhance the mechanical, thermal and wear resistance properties of polymer matrix. Polycarbonate (PC) is classified as an amorphous engineering thermoplastic widely used in many fields of applications because of its convincing mechanical and optical properties [2-5]. Transparency is a key property of PC. The optical properties, combined with the material toughness, strength, and resistance to UV light, make PC an alternative material towards glass in many applications. For example, PC has been used in the medical market regarding its transparency and unique mechanical properties, such as filter housings, tubing connectors and surgical staplers [6]. However, it has been found that PC exhibits stress-crazing (cracking) under influence of stress in some environments (ESC) [7-11]. This may lead to disastrous consequences during applications. It is known that addition of inorganic fillers to PC can achieve some improvements of mechanical and electrical properties [12-15], but studies of filler influence on ESC of PC are still rare.

Polypropylene (PP) is one of the most widely used polyolefins due to its attractive properties and low cost. These attributes resulted in significant growth of PP production in recent years for application in automotive, food packaging, and home appliance industries. One of the major shortcomings of PP is the low toughness or resistance to fracture, especially at high deformation rate and at low temperatures. Besides, the stiffness of PP is also relative low compared to other most used plastics [16]. Many studies have shown that the mechanical properties of PP can be improved when inorganic fillers are well dispersed in PP matrix [17-28]. Chan et al. [29] have reported that the Izod impact strength of PP/$CaCO_3$ nanocomposites was drastically increased by approximately 300% and the notched impact toughness obtained by J-integral tests increased even by 500%. In the work of Thio et al. [30], the mechanical properties of PP composites containing $CaCO_3$ particles with average diameters of 0.07, 0.7 and 3.5 μm were evaluated. The authors found that the addition of 0.7 μm diameter particles improved Izod impact energy up to four times in comparison with neat PP. Huang et al. [31] have investigated the mechanical properties of nanosilica filled PP composites. They found that both the tensile strength and the notched impact toughness of PP composites were markedly enhanced after surface treatment of nanosilica.

Thermoplastic elastomers (TPEs) are materials which exhibit a unique combination of strength, flexibility and processability due to their phase-separated microstructure. One important class of TPEs are co-poly(ether ester)s. The

commercial polyester elastomers are mostly copolymers based on poly(butylene terephthalate) (PBT) as rigid segment and poly(tetramethylene glycol) (PTMG) as flexible segment. Many researchers concluded that the PBT-PTMG system after crystallization can be described by a two-phase model: a crystalline PBT phase and a homogenous amorphous PTMG phase mixed with non-crystalline PBT segments [32-34]. In recent years, the crystallization process, the microstructure and phase behaviour of PBT-PTMG systems have been studied in detail [35-39]. El Fray and co-workers investigated the influence of chemical composition on the phase structure and structure-property relationships of polyester-based TPEs [40]. Interesting results are reported on the basis of studies on the influence of chemical composition and molecular weight of PTMG segments on the mechanical properties of PBT-PTMG block copolymers [41, 42]. Over the last years, nano-reinforcement strategies have been exhaustively adopted for polymers of both thermoplastics and thermoset types. However, thermoplastic elastomers are scarcely studied [43].

In this study, particulate-filled polymer composites based on thermoplastics and thermoplastic elastomer were systematically investigated. The influences of particle loading, particle surface polarity, particle content and particle size on the properties of polymer composites were characterized. Furthermore, the structure-property relationships of produced polymer composites were evaluated and discussed.

1.2 Background

1.2.1 Thermoplastics and thermoplastic elastomer (TPE)

Thermoplastics are polymers that melt to liquid when heated and solidify again when cooled. Most of thermoplastics are high molecular-weight polymers whose chains associate through weak Van der Waals forces such as polyethylene, or through stronger dipole-dipole interactions and hydrogen bonding such as nylon, or even stacking of aromatic rings as polystyrene. Thermoplastics are classified as noncrystallizable amorphous plastics and crystallizable semi-crystalline resins. The amorphous polymers are frequently used in applications where clarity is important. Typical amorphous thermoplastics are poly(methyl methacrylate) (PMMA), polystyrene (PS), and polycarbonate (PC). Such materials are elastic and flexible above a glass transition temperature (T_g). In general, amorphous polymers are less chemically resistant and can be subjected to stress cracking. Conversely, semi-crystalline thermoplastics are more resistant to solvents and other chemicals. In addition, semi-crystalline polymers are usually hazy or opaque due to large crystallites, for example, polyethylene (PE), poly(butylene terephthalate) (PBT), and polypropylene (PP). Such polymers become less brittle above T_g.

Polycarbonate (PC)

Polycarbonates are tough, strong, high-performance amorphous engineering thermoplastics which find widespread use in industry. They are polymers having

functional groups linked together by carbonate groups in a long molecular chain. Polycarbonates are ideal engineering plastics since they can be injection moulded and extruded. According to chemical structures, polycarbonates can be divided into poly(aromatic carbonate)s and poly(aliphatic carbonate)s. The most common type of polycarbonates is bisphenol-A polycarbonate (BPA-PC) which chemical structure is shown in Figure 1.2.1. A standard, natural, uncoloured PC typically shows high transparency to visible light with the following optical properties according to ASTM D 1003: light transmittance 89.0%, haze 1.0% and yellowness index 0.24. Although PC has very good mechanical properties such as high impact resistance and fracture toughness, it often exhibits unexpected cracking in chemical environments due to stress corrosion (ESC). Furthermore, PC usually shows an obvious discoloration after extruding process due to thermal degradation or hydrolysis of its carbonate groups, which are very sensitive to high temperature and hydroxyl groups [44, 45]. PC has a glass transition temperature of about 150 °C, so it softens gradually above this temperature and flows above 300 °C.

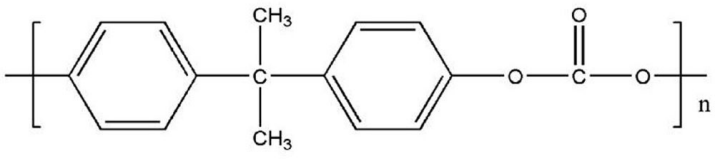

Figure 1.2.1: Chemical structure of bisphenol-A PC [2].

Polypropylene (PP)

PP is one of the most important commodity plastics, number two besides polyethylene (PE) in terms of global production [46]. Initially, PP was produced commercially about 50 years ago after the successful development of a stereo-specific Ziegler-Natta catalyst, which allowed the control of stereochemistry of polymers during polymerization process [47]. According to the position of methyl groups with respect to the backbone chains of PP, three stereoisomers can be obtained, i.e. isotactic PP (iPP), syndiotactic PP (sPP) and atactic PP (aPP) [48-51]. “Isotactic” means that all the methyl groups are on the same side of the PP back-bone chain. When the position of the side group alternates, it is called “syndiotactic”. Atactic means that the methyl groups are randomly placed on both sides of long polymer chain. Figure 1.2.2 shows all three tacticities of PP. The tacticity can significantly affect the crystallization behaviour and other polymeric properties. Both iPP and sPP are crystallizable whereas aPP is noncrystallizable, soft and tacky with very poor thermal and mechanical properties. The most commercially important stereoisomer of PP is iPP which shows good physical, mechanical and thermal properties.

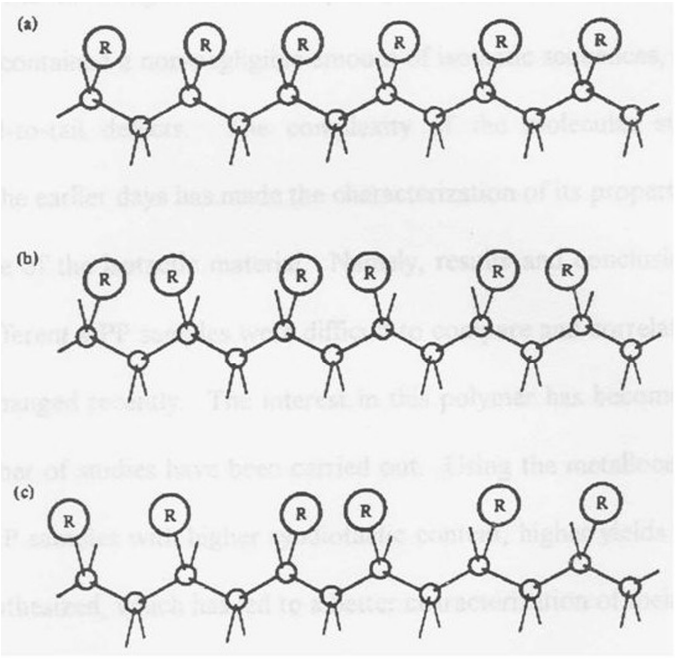

Figure 1.2.2: Different tacticities of PP: (a) iPP, (b) sPP, and (c) aPP [48-51].

Homopolymer iPP is semi-crystalline and contains both crystalline and amorphous phases as shown in Figure 1.2.3. The relative amount of each phase depends on structural and stereochemical characteristics of the polymer chains and the conditions under which the polymer is produced. In the crystalline phase, there are three possible crystalline forms of PP, i.e. the monoclinic α-form, the hexagonal β-form and the triclinic γ-form [52], in which the α form is the dominant crystal form with a melting temperature of about 160 °C [53]. The β and γ-forms are less stable.

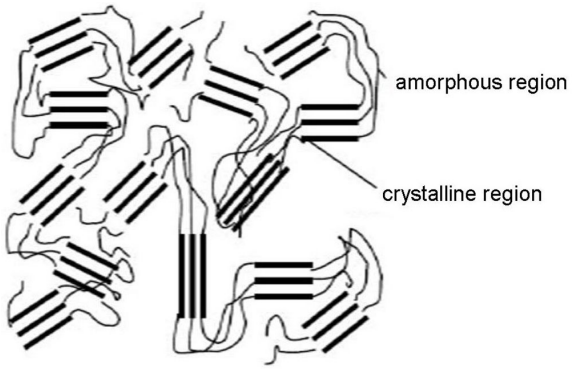

Figure 1.2.3: Macromolecular structure of a semi-crystalline iPP [48].

Thermoplastic elastomer (TPE)

Thermoplastic elastomers are copolymers composed of two different types of segments, namely a hard crystalline phase and a soft rubbery phase. Strength of elastomers is provided by the hard phase, while the elastomeric behaviour arises from the soft phase. The TPEs are processed at a high temperature when the hard phase melts and flows. In the molten state, the hard and soft segments form a homogenous mixed phase. Upon cooling, the hard segments crystallize and act as physical crosslinks in the copolymers as shown in Figure 1.2.4.

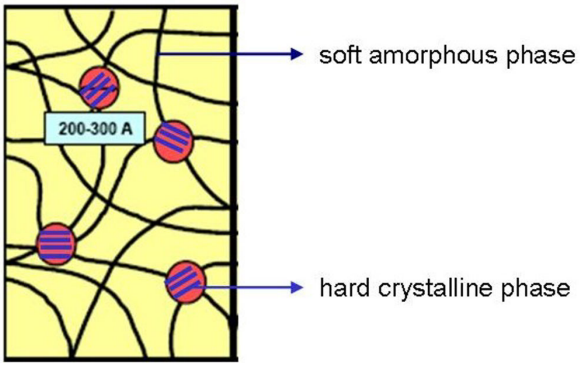

Figure 1.2.4: Phase-separated microstructure of TPEs [32].

The crystallization process of hard phase is the driving force for the phase separation in TPEs [38, 39, 54]. Generally, TPEs are low modulus, flexible materials that can be stretched repeatedly to at least twice their original length at room temperature with an ability to return to their approximate original length when the stress is released. TPEs have already proven their performance for a wide variety of applications in automotive, electrical/electronic and various other industrial and consumer products.

Among variety of TPEs synthesized and studied so far, poly(ether ester)s have attracted special attention such as PBT-PTMG block copolymer. The first poly(ether ester) copolymers obtained by modification of poly(ethylene terephthalate) with up to 20 wt% of poly(ether) were described by Coleman [55]. After that, the Dupont Co. developed poly(ether ester) elastomers which were commercially introduced in 1972 under the trade name Hytrel®. Nowadays, the polyester-based TPEs are widely produced and used in many applications. Figure 1.2.5 shows the chemical- and phase-structure of a PBT-PTMG block copolymer in which PBT acts as the hard crystalline phase whereas PTMG is the soft amorphous phase. The major driving force for phase separation in this copolymer is the crystallization of hard PBT segments. The service temperature of the PBT-PTMG copolymer lies between the glass transition temperature of soft PTMG phase (about -50 °C for homopolymer [35-37]) and the crystalline melting temperature of hard PBT phase. The molecular weight and the weight percentage of a single composition in PBT-PTMG copolymer can strongly affect the thermal

properties of both compositions [38].

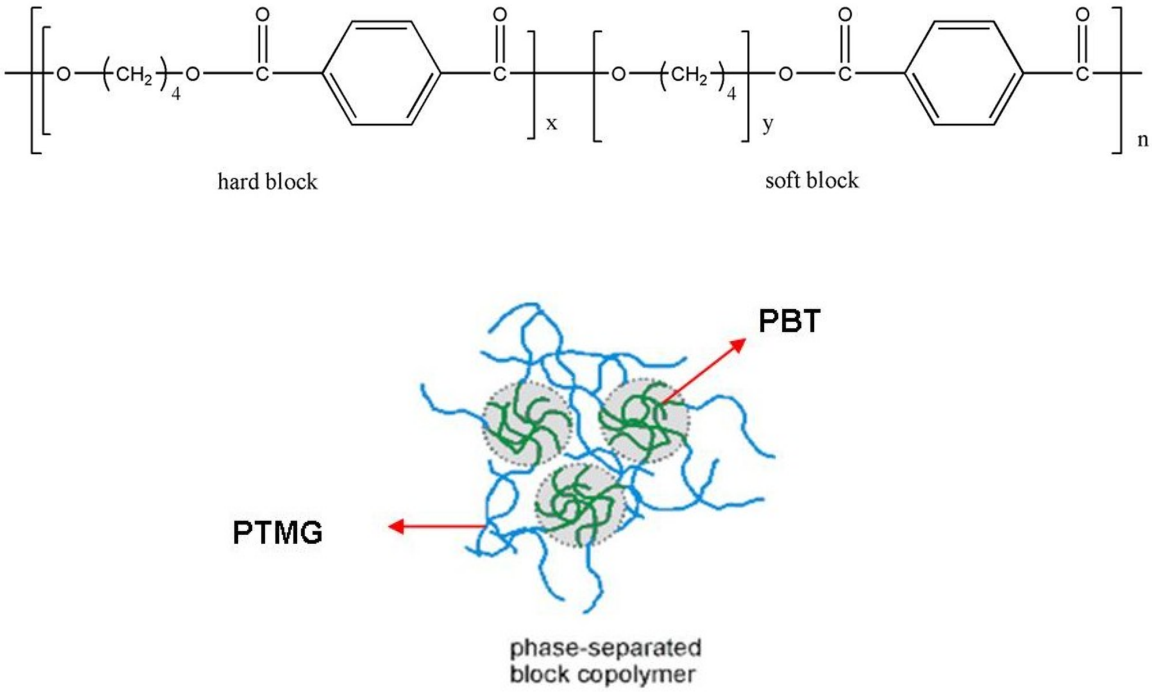

Figure 1.2.5: Chemical- and phase-structure of PBT-PTMG block copolymer [32-33].

1.2.2 Nanofillers

In the last decade, methods have been developed to prepare and characterize nanomaterials of different chemical compositions and aspect ratios (length/width ratio) with nano-size in either three dimensions (3D: particles as silica, carbon black, etc.), two dimensions (2D: carbon nanotubes – CNTs, needle-like clays, glass fibres, etc.) or one dimension (1D: lamellar inorganics such as layered silicates, clays, phosphates, etc.) as shown in Figure 1.2.6 [56, 57].

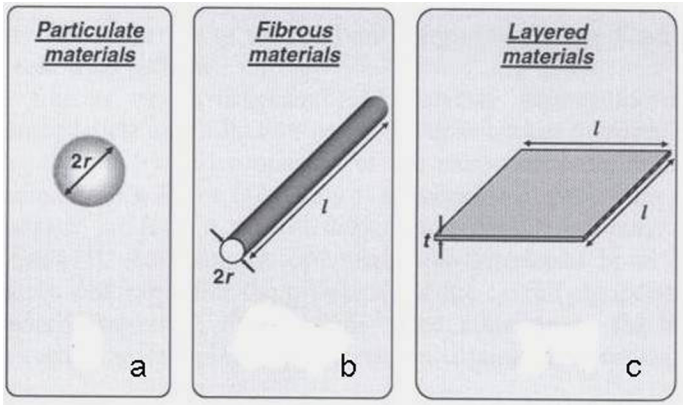

Figure 1.2.6: Classification of common nanostructured materials according to their geometries: (a) particulate material, (b) fibrous material, and (c) layered material [56, 57].

In the case of nanoparticles with a small aspect ratio of 1, inorganic nanofillers such as metals (Fe, Au, Cu, etc.), metal oxides (TiO_2, ZrO_2, Al_2O_3, etc.) and non-metal oxides (e.g. SiO_2) have been used as reinforcements in different polymers. The incorporation of nanoparticles in polymers can result in a dramatic change in the material properties depending on the size and surface nature of used nanofillers. The surface area of nanoparticles plays an important role in polymer/nanoparticle composites influencing the interfacial properties, the agglomeration behaviour and the physical and mechanical properties of composites. The smaller the particle diameter, the greater is the surface area of particles per unit volume [58]. The selection of nanoparticles depends on the desired material properties, such as improvement in mechanical, thermal, electrical or barrier properties. For example, metal fillers can improve the creep

properties at high temperatures; TiO_2 can be used as a white pigment due to its brightness and flame retardant for many polymers while SiO_2 nanoparticles are often used because of their “extremely” high thermal stability [59-61].

Aerosil® SiO_2 and TiO_2 nanoparticles and particle surface modification

Gas-phase synthesis (flame hydrolysis) is a well-known technique for the production of an extensive variety of nanoparticles. The commercial nanoparticles produced by this method comprise the largest share of the market e.g. as reinforcing fillers, for rheology control and as pigments. Examples are the pyrogenic silica, titania, alumina and industrial carbon black produced by Evonik, Germany. The nanosized powders are manufactured in gas phase at temperature up to 10000 Kelvin. The manufacturing process and conditions determine the size and morphology of the nanoparticles and hence their application properties [62]. In industrial products, primary nanoscale particles are normally not isolated but build up aggregates and agglomerates. In aggregates, the primary particles contact each other at surface or edges and they cannot be broken down further by shear forces applied by application [63]. Agglomerates are formed when aggregates and/or primary particles contact each other as shown in Figure 1.2.7.

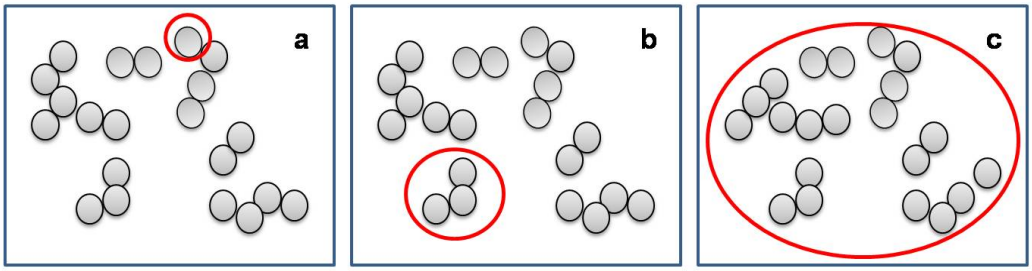

Figure 1.2.7: Schematical Illustration of nanoparticles in different forms: (a) primary particle, (b) aggregate and (c) agglomerate [63].

In the case of fumed silica or titania nanoparticles, the surfaces of nanoparticles contain a certain amount of hydroxyl groups formed during processing. These hydroxyl groups can build up hydrogen bonding among particles, resulting in a temporary, three-dimensional lattice structure as shown in Figure 1.2.8. Such hydrogen bonds belong to relative strong interactions with bond energy of about 20 kJ/mol and are very difficult to be broken down [64].

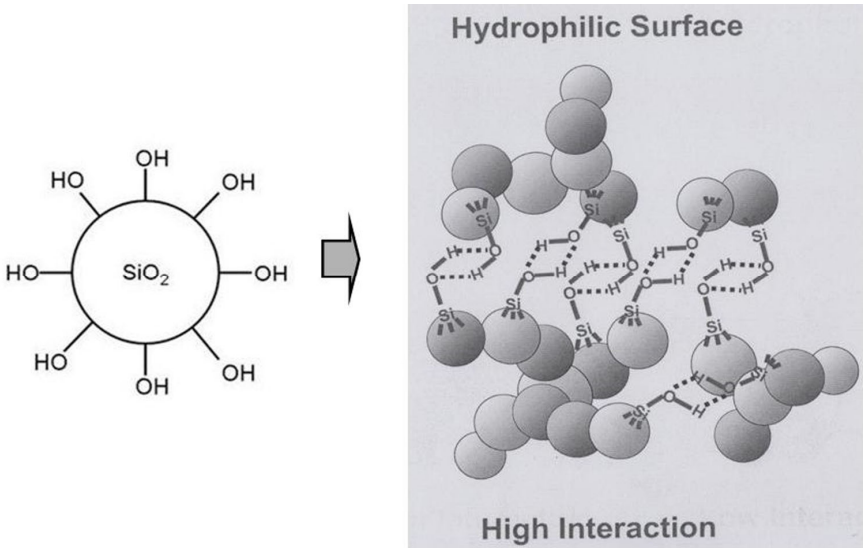

Figure 1.2.8: Schematically description of aggregate formation between fumed silica nanoparticles through hydrogen bonding [picture taken from technical information of particle supplier Evonik Co, Germany].

The great differences in the properties of polymer matrix and inorganic nanoparticles can often cause phase separation. Therefore, the interfacial interaction between two phases in nanocomposites is the most decisive factor affecting the properties of achieved nanocomposites. A variety of methods have been used to enhance the compatibility between hydrophobic polymer matrix and hydrophilic nanoparticles. The most frequently used method is to modify the surface of inorganic nanoparticles. There are two advantages regarding chemical surface modification of nanoparticles. One is the steric stabilization of nanoparticles towards agglomeration and the other is to improve the compatibility between particle surface and polymer matrix. Figure 1.2.9 shows schematically the surface modification process of polar silica or titania nanoparticles with

silanes [65].

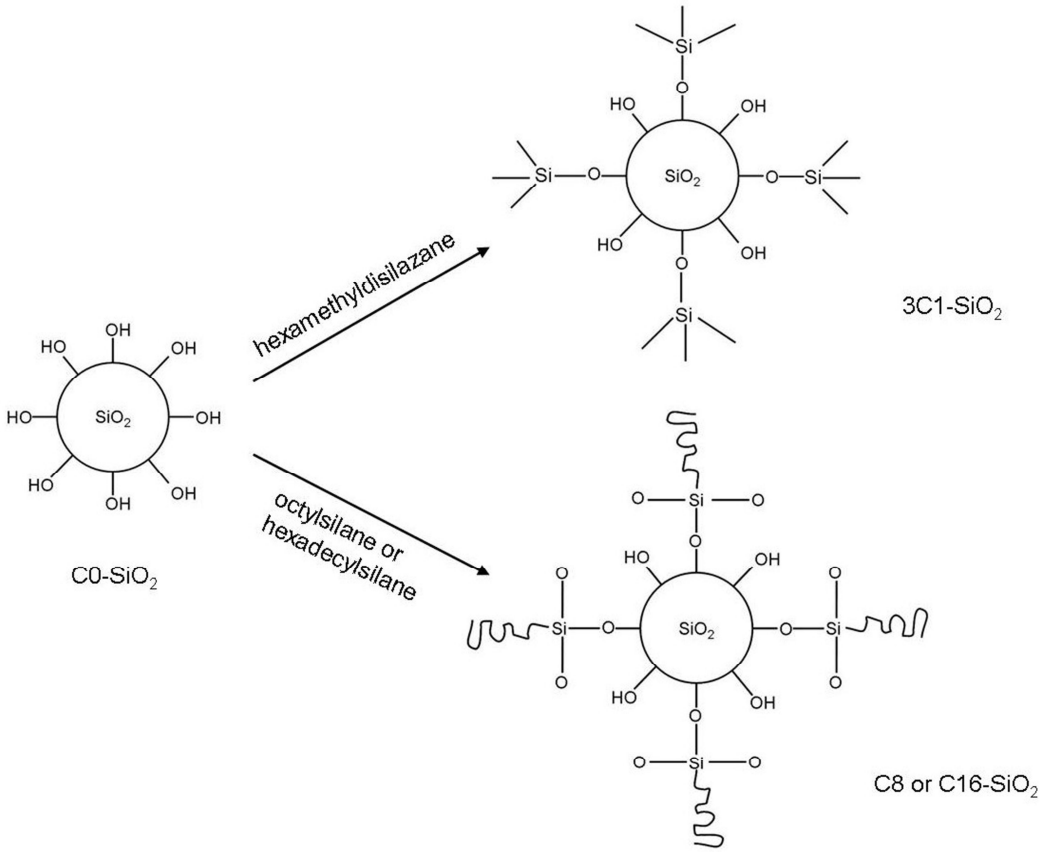

Figure 1.2.9: Schematic illustration of surface modification of silica nanoparticles with different silanes [65].

After this chemical treatment, alkyl chains with different chain length and structure will be bound via Si-O-SiO_2 (or Si-O-TiO_2) bridge linkages on particle surface, increasing the hydrophobicity of SiO_2 or TiO_2 nanoparticles. On the other hand, the alkyl chains on particle surface can significantly reduce the formation of hydrogen bonds due to steric hindrance, decreasing the degree of particle agglomeration as shown in Figure 1.2.10.

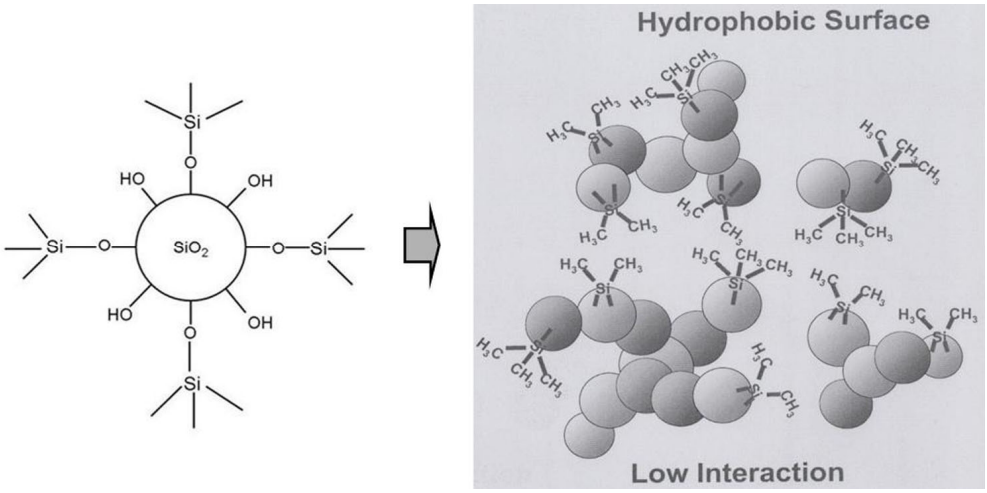

Figure 1.2.10: Low interaction between SiO_2 nanoparticles after surface modification [picture taken from technical information of particle supplier Evonik Co, Germany].

1.2.3 Polymer composites and compounding techniques

Interfacial tension and adhesion in iPP/SiO_2 (TiO_2) nanocomposites

Among the various factors which determine the final performance of a polymer composite, the interfacial adhesion between nanoparticles and polymer matrix plays a very important role. Thermodynamic wetting of the nanoparticle surface by the polymer matrix is a necessary condition for particle-matrix adhesion and is determined by the free energies of the components [66, 67]. Application of surface energy criteria is practicable because the surface energy may be determined independently using wetting and surface tension measurements [68, 69]. Generally, surface tensions (γ) of polymers vary linearly with temperature following the Guggenheim equation [70]:

$$\gamma = \gamma_0 (1 - \frac{T}{T_c})^{11/9} \qquad (1.1)$$

Where γ_0 is the surface tension at T= 0 Kelvin and T_c is the critical temperature. Table 1.1 shows some polymers with their γ_0 and T_c values [71].

Table 1.1: Values of γ_0 and T_c of some polymers

polymer	γ_0 [mN/m]	T_c [Kelvin]
PE	53.71	1032
PP	47.16	914
polyisobutylene	53.74	918
PS	63.31	967
PMMA	65.09	935

For iPP, γ_0 is 47.16 mN/m and T_c is 914 K. Thus, the surface tension of iPP at 220 °C (493 K) can be calculated as 18.29 mN/m according to equation (1.1). As already known, iPP is a nonpolar polymer with relative low surface tension. By contrast, the untreated SiO_2 and TiO_2 nanoparticles are polar materials with OH-groups on the particle surface. The surface tensions of SiO_2 and TiO_2 nanoparticles at 1500 K are 300 mN/m and 500 mN/m, respectively [72], indicating that the TiO_2 nanoparticles have much higher surface polarity than the SiO_2 nanoparticles. Furthermore, the polarity of materials is independent of temperature [73, 74]. The greater the polarity difference between two mixed phases, the greater will be their interfacial tension [71]. Therefore, the following relation can be obtained:

$$\gamma_{iPP-TiO_2} >> \gamma_{iPP-SiO_2} \quad (1.2)$$

This indicates that the interfacial tension between iPP matrix and TiO_2 nanoparticles is much larger than the value between iPP matrix and SiO_2 nanoparticles. According to [75], higher interfacial tension results in lower interfacial adhesion. Thus, the interfacial adhesion in iPP/SiO_2 (untreated) composites is better than that in iPP/TiO_2 (untreated) composites.

The surface tension of a solid material can be divided into two parts, i.e. the dispersive (γ^d) component and the polar (γ^p) component, as suggested by Fowkes [76, 77]:

$$\gamma = \gamma^d + \gamma^p \quad (1.3)$$

After surface modification of SiO2 and TiO2 nanoparticles with silanes, the polar component (γ^p), which is partly caused by hydrogen bond, decreases due to introduction of hydrophobic alkyl chains onto particle surface, leading to decreased surface tension of respective nanoparticles and subsequent decreased interfacial tension between iPP matrix and surface-modified nanoparticles. For example, Table 1.2 shows the contact angles against water of some SiO_2 and TiO_2 nanoparticles from company Evonik [78].

Table 1.2: Contact angles against water at 20°C of some SiO_2 and TiO_2 nanoparticles [78]

nanoparticles	contact angle against water [degree°]
Aerosil® 200	19.13 ± 0.12
Aerosil® R805 (surface modified based on Aerosil® 200)	136.10 ± 5.19
Aerosil® 300	16.30 ± 0.40
Aerosil® R812 (surface modified based on Aerosil® 300)	84.73 ± 1.68
Aeroxide® TiO_2 P25	23.31 ± 1.82
Aeroxide® TiO_2 R805	143.10 ± 5.44

For a given liquid with its own surface tension properties, it is water in this case, the lower the contact angles, the higher the specific surface tension/energy of the solid material. Conversely, the higher the contact angle, the lower the specific surface tension/energy of the solid material [79]. From Table 1.2, it is evident that the silane-modified SiO_2 and TiO_2 nanoparticles exhibit much lower surface tension than respective unmodified nanoparticles.

As introduced above, the interfacial adhesion is weaker in iPP/SiO_2 (TiO_2) composites filled with polar unmodified nanoparticles because of larger interfacial tension. After surface modification of nanoparticles, the introduced alkyl chains on the particle surface can act as bridge to link polar particles and non-polar polymer matrix such as iPP. This helps to transfer the stresses between polymer matrix

and particles, thus improving the interfacial interaction in polymer composites. According to different adhesion mechanisms, the coupling forms include covalent bonds (>200 kJ/mol), dipole-dipole bonds, hydrogen bonds (~20 kJ/mol), and van der Waals forces (London forces, <16 kJ/mol) [63]. Covalent bonds are formed by the reaction of two chemical groups and typically result in the highest “adhesion”. Dipole-dipole interactions occur when the positive end of one polar molecule is attracted to the negative end of another polar group. The hydrogen bonding can only be formed when the hydrogen atom is connected to an electronegative atom such as nitrogen or oxygen. In the interphase between iPP and surface-modified nanoparticles, the alkyl groups have very limited polarity resulting in neither dipolar bonding nor hydrogen bonding. However, the surface-modified SiO_2 or TiO_2 nanoparticles can be well adhered in the iPP matrix due to chain entanglement in the interphase (van der Waals forces). Chain entanglement occurs either at elevated temperatures at which the organic molecules are highly mobile such as during extrusion process or in concentrated solution. Figure 1.2.11 schematically describes the different interfacial interactions in surface-modified and unmodified particle-filled iPP/SiO_2 composites.

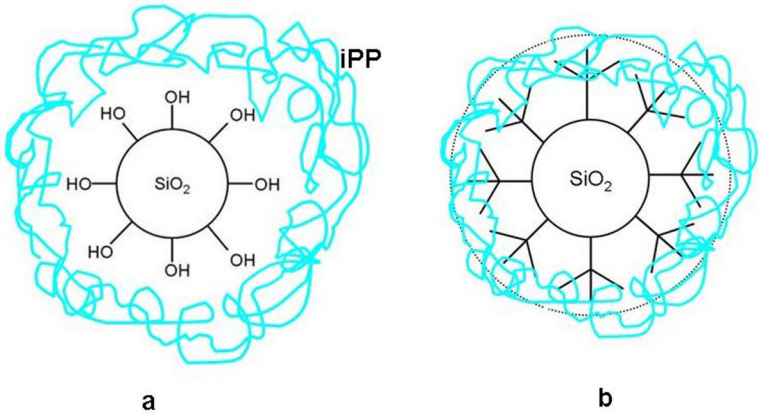

Figure 1.2.11: Different interfacial interactions between iPP matrix and unmodified SiO_2 nanoparticles (a) or silane-modified SiO_2 nanoparticles (b).

Interfacial interactions in TPE(PBT-PTMG)/TiO_2 composites

Metal oxide nanoparticles such as TiO_2 can interact with acidic functionalities of polymers, increasing the particle-matrix interaction. As schematically illustrated in Figure 1.2.12, different bonding modes between carboxylate group in PBT-PTMG copolymer and TiO_2 particle are reported [80, 81].

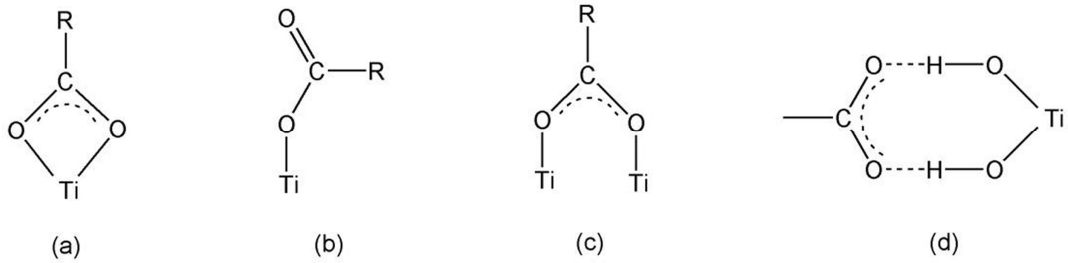

Figure 1.2.12: Binding modes between carboxylate group and TiO_2 nanoparticles: (a) chelating bidentate, (b) monodentate, (c) bridging dentate, and (d) hydrogen bonding [80, 81].

In the first case, carboxylate is bounded to one Ti (IV) center in a chelating bidentate mode (a). The carboxylate could also be bounded to one Ti (IV) atom in a monodentate (ester-like linkage) mode (b) and next, the carboxylate group could bind with each of its oxygen atoms to two Ti (IV) atoms yielding the bridging bidentate mode (c). These three binding modes are the dominant bond structures with bond energy of about 100 kJ/mol. Besides these three direct binding modes, carboxylate could also build up hydrogen bonding with hydroxyl groups on the titania surface as shown in mode (d). According to [81], the hydrogen binding comprises about 3% of the total binding modes, the ester-like monodentate accounts for 63% and the chelating together with bridging modes account for 34%. All these chemical bonds provide excellent adhesion between polymer matrix and TiO_2 particles, influencing the morphological, thermal and mechanical properties of TPE(PBT-PTMG)/TiO_2 composites.

Compounding techniques for polymer composites

The main difficulty in the mixing process is always the effective dispersion of the nanoparticles, because they usually exist as agglomerates/aggregates due to Van der Waals forces among the particles (large specific surface area). To prepare polymer nanocomposites different methods have been applied, such as in-situ polymerization, solvent-assisted techniques and direct melt blending techniques [82]. In-situ polymerization allows adjusting the chemistry to optimize the affinity between nanofillers and polymer matrix. Different types of

polymerization methods have been used to prepare polymer composites, such as in solution [83], in suspension [84], and in emulsion [85]. Latex- or water-mediated melt compounding is a promising technique to prepare polymer composites in which latex or water is used as dispersing assistants for nanofillers. The latex- or water slurry containing nanofillers can be introduced into polymer melt during melt compounding process [59]. Among various compounding methods, the direct melt compounding method is usually more practical and economical than other methods [86]. Different direct melt blending techniques with increasing shear forces like simple laboratory dissolver stirrers generate only small mechanical forces while high speed stirrers (up to 25000 rpm) and high pressure homogenizers (up to 10^8 Pa) enable a pronounced deagglomeration of nanoparticles. These techniques can be applied at composite viscosities below 10 Pa·s [87]. Mixer-kneader and extruders allow for the processing of high viscous polymer melts. In the latter case the resulting shear forces depend also on the configuration of the used extruder screws.

In the industry, twin-screw extrusion is one of the most commonly used techniques for compounding of fillers and additives into polymers. This technique offers the possibility of continuous production. Depending upon the direction of rotation of the twin screws as shown in Figure 1.2.13, the extruders are divided into co- and counter-rotating extruders. In contrast to the counter-rotating twin screw extruder which forms closed chambers, conveying of the polymer melt in the co-rotating twin screw extruder is a result of the drag flow and pressure flow.

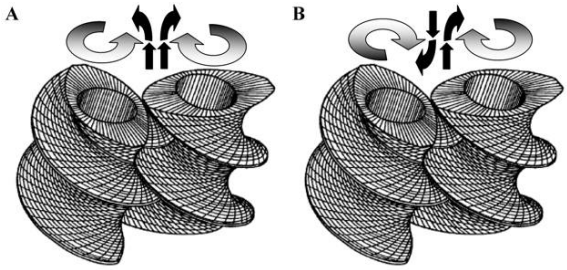

Figure 1.2.13: Schematic illustration of screw rotations in a twin-screw extruder: (A) counter-rotation, and (B) co-rotation (picture taken from [46]).

During processing the polymer melt is moving from one screw to the other so that the material melt cannot stick in the channel-grounds. There are different screw elements with different geometries available for conveying, mixing, and kneading function as shown in Figure 1.2.14, so that different screw configurations can be adapted for different process tasks. Figure 1.2.15 gives a schematic illustration of a twin-screw extruder.

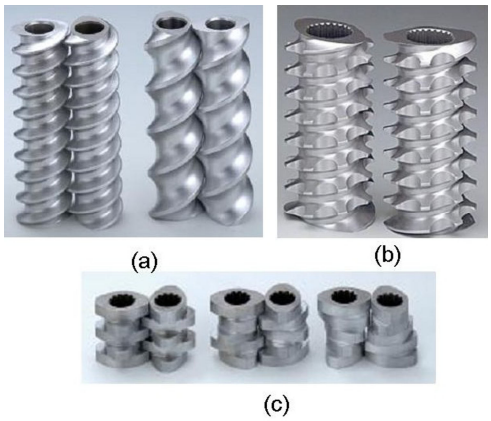

Figure 1.2.14: Screw elements: (a) conveying elements, (b) mixing elements, and (c) kneading blocks.

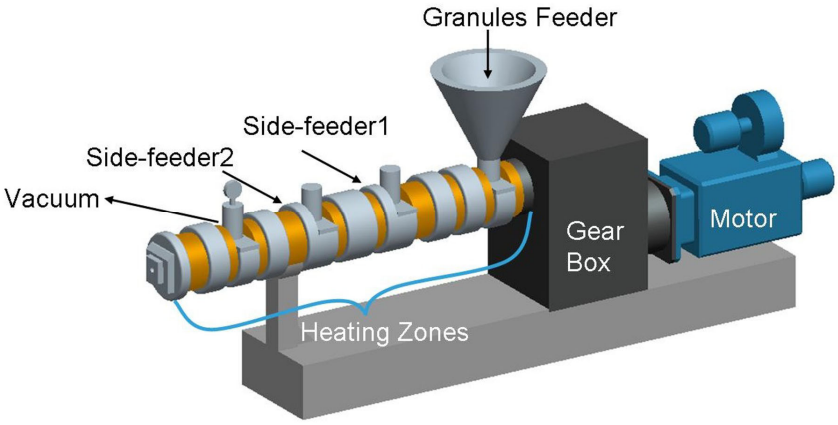

Figure 1.2.15: Schematic illustration of a twin-screw extruder.

1.2.4 Behaviour analysis of polymer composites

Optical properties of materials

The typical parameters characterizing the transparency of a material are the light transmittance, the haze, and the clarity. Figure 1.2.16 illustrates some dimensionless parameters that are commonly measured in order to characterize the optical properties of materials.

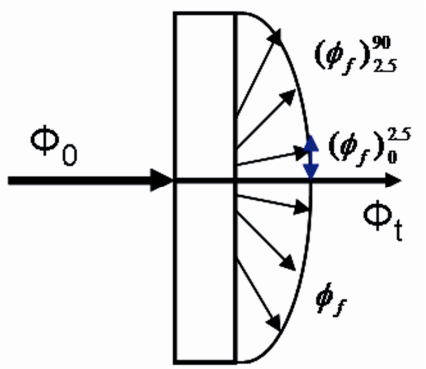

Figure 1.2.16: Parameters used to characterize the transparency of materials [88].

As shown in figure 1.2.16, a light beam Φ_0 is incident upon a sample, and a diminished undeviated transmitted beam Φ_t emerges on the far side. The forward-scattered light flux denoted by Φ_f may be subdivided into two ranges of scattering angle, namely from 0° to 2.5° ($(\phi_f)_0^{2.5}$) and from 2.5° to 90° ($(\phi_f)_{2.5}^{90}$). The light transmittance and haze are defined as follows [88]:

$$L_D = \frac{\phi_t}{\phi_0}$$

$$L_T = \frac{\phi_t + \phi_f}{\phi_0} \qquad (1.4)$$

$$H = \frac{\left(\phi_f\right)_{2.5}^{90}}{\phi_t + \phi_f}$$

where L_D, L_T and H are the direct light transmittance, the total light transmittance, and the haze, respectively. Different from the test situation for haze and light transmittance, where the standard measurement is widely used and almost universally accepted, there are several methods for characterization of clarity, which differ in principle and detail [89]. Small-angle scattering method is often used to determine the clarity of materials. By using this method, small-angle scattering deflects the light beam into small angles, so that the light intensity is concentrated within this narrow angular range and detected.

In general, light losses are mainly due to reflection at the outer surface of samples and at the interfaces between polymeric matrix and dispersed particles. This reflection occurs because of the difference in the refractive indices between different media. The reflection coefficient R is given by Fresnel's equation [90]:

$$R = \left(\frac{n_1 - n_2}{n_1 + n_2}\right)^2 \qquad (1.5)$$

where n_1 and n_2 are the refractive indices of polymeric matrix and particles, respectively. From equation (1.5), the larger the difference in refractive indices of media, the more light will be reflected (lost).

Time-temperature superposition

Polymers, because of their viscoelastic nature, exhibit behaviour during deformation which is both temperature and time (frequency) dependent. For example, polymers can slowly deform under constant loading at room temperature. This phenomenon is creep. It occurs because the polymers under a load undergo molecular rearrangement in an attempt to minimize localized stresses. This time and temperature dependent behaviour is an important characteristic of polymers which affects the life-time of end-use products. It was pointed out that the effects of time and temperature are equivalent [91]. That means high temperature and long time have similar effect on the polymers. Accordingly, the large drawback of long-term creep test can be overcome by shifting curves measured at different temperatures over short time periods. This method is called **T**ime-**t**emperature **s**uperposition (TTS). Using TTS method the long-term creep behaviour of materials can be predicted based on short-term creep tests at higher temperatures [92-95].

In general, the creep compliance J(t) can be described as the ratio of strain (ε) to stress (σ) at a certain time (t) [95]:

$$J(T,t) = \frac{\varepsilon(T,t)}{\sigma} \tag{1.6}$$

The curves of creep compliance obtained at different temperatures can be superposed by horizontal shifting along the logarithmic time scale to obtain the master curve as shown in Figure 1.2.17. The degree of horizontal shifting (time) is called shift factor which can be mathematically described with respect to

temperature.

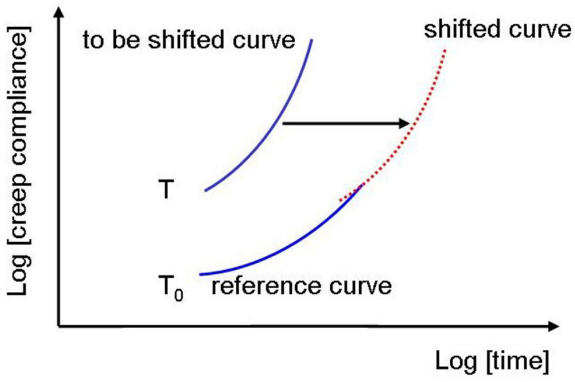

Figure 1.2.17: Schematic description of time-shift procedure [93].

The first empirical model to describe the relation between temperature and shift factor is the Williams-Landel-Ferry (WLF) equation [96]:

$$\log a_T = \frac{-C_1(T - T_0)}{C_2 + (T - T_0)} \tag{1.7}$$

where α_T is the horizontal shift factor, T and T_0 are the experimental and reference temperatures in Kelvin (K), C_1 and C_2 are constants. For many amorphous polymers, T_0 is usually taken as the glass transition temperature T_g. The WLF equation is typically used to describe the time-temperature behaviour of polymers in the glass transition region.

The other model which is commonly used to relate the shift factors with respect to temperature is the Arrhenius equation [97]:

$$\log a_T = \frac{E}{R}\left(\frac{1}{T} - \frac{1}{T_0}\right) \tag{1.8}$$

where E is the activation energy associated with the relaxation transition, R is the common gas constant (R = 8.314 J/mol). The Arrhenius equation is typically used to describe the viscoelastic events associated with β and γ relaxation transitions or for the glass transitions associated with semi-crystalline polymers.

Fracture mechanics of polymer composites: Linear Elastic Fracture mechanism (LEFM)

In modern materials science, fracture mechanics is an important tool in improving the mechanical performance of materials and components. It applies the physics of stress and strain, in particular the theories of elasticity and plasticity, to the microscopic crystallographic defects found in real materials in order to predict the macroscopic mechanical failure of materials. In the case of brittle materials, for example, fibre or particle-filled polymer composites, the linear elastic fracture mechanism or LEFM is usually applied to determine the fracture behaviour of these materials. However, there are some conditions to be taken into consideration by using the LEFM, i.e. [98]

- Crack has been initiated in the material.
- Material is linearly elastic and isotropic.
- Plastic zone near the crack tip is very small.

There are three ways of applying a force to enable a crack to propagate as described as follows and shown in Figure 1.2.18:

Mode I----Tension, normal to the faces of the crack (opening mode)

Mode II----Shear, normal to the crack front in the plane of the crack (edge sliding mode).

Mode III----Shear, parallel to the crack front (tearing mode).

The most commonly found failures are due to cracks propagating predominantly in mode I, and for this reason materials are generally characterized by their resistance to fracture in mode I.

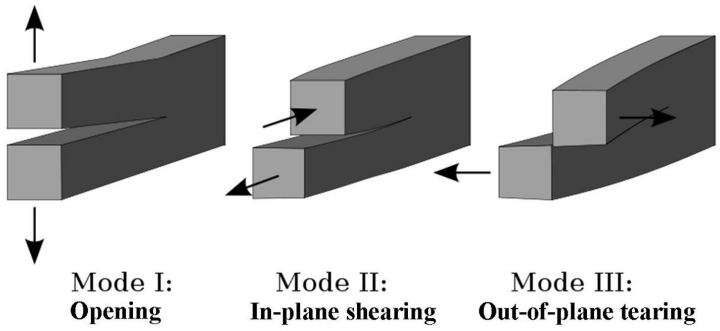

Figure 1.2.18: Different fracture modes in a real material [98].

In order to describe the linear elastic area in front of the crack tip, a parameter K; the stress intensity factor, is used. According to LEFM concept, the stress intensity factor K; can be described as:

$$K_i = \sigma\sqrt{\pi \cdot a} \cdot f(\varphi) \tag{1.9}$$

$$\varphi = \frac{a}{W} \tag{1.10}$$

Where the term $f(\varphi)$ is a non-dimensional correction factor and usually expressed as a ratio of crack length to any convenient local characteristic dimension in the plane of the component. σ is the stress in front of the crack tip, *a* and *W* are the crack length and the ligament length of studied sample, respectively, *i* relates to the fracture mode I, II and III.

For a compact tension sample with initiated pre-crack a_0 and ligament length W, the correction factor $f(\varphi)$ can be calculated as follows:

$$f(\varphi) = \frac{2+\varphi_0}{1-\varphi_0^{3/2}} \cdot (0.886 + 4.64 \cdot \varphi_0 - 13.32 \cdot \varphi_0^2 + 14.72 \cdot \varphi_0^3 - 5.6 \cdot \varphi_0^4) \quad (1.11)$$

$$\varphi_0 = \frac{a_0}{W} \quad (1.12)$$

The pre-crack in sample starts to propagate when the stress intensity factor K_i attains a critical value K_{ic}, i.e. the condition for crack propagation is $K_i \geq K_{ic}$. The parameter K_{ic} is called fracture toughness and depends on the material, temperature, strain rate, environment, and thickness of material.

Depending on the thickness of materials, the plastic deformation and crack propagation can be divided into two types, i.e. plane stress and plane strain. In plane stress conditions, the plastic zone at the crack tip is produced by shear deformation through the thickness of the specimen. Such deformation is enhanced if the thickness of the specimen is reduced. If the specimen thickness is increased, the additional constraint on through-thickness yielding produces a triaxial stress distribution so that approximate plane strain deformation occurs with shear in the xy plane. There is usually a transition from plane stress to plane strain conditions as the specimen thickness is increased as illustrated in Figure 1.2.19 [99].

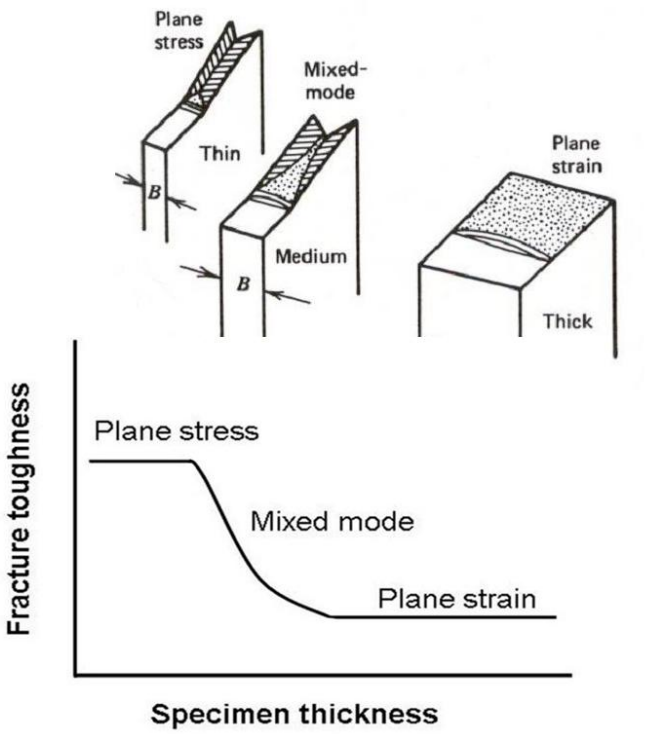

Figure 1.2.19: Influence of specimen thickness on fracture toughness and related stress states [99].

For a plane strain fracture in mode I, the fracture toughness K_{IC} is considered as a true material property independent of sample thickness. In order to determine the fracture toughness K_{Ic}, the following condition by sample preparation should be fulfilled according to ASTM D5045-99 and ASTM E399-90 standards: $0.45 < a_0/W < 0.55$.

The incorporation of rigid nanoparticles into polymer matrix leads to differences in the overall processes of crack propagation and fracture. The fracture process starts with the plastic deformation of the polymer matrix ahead of the initial crack.

The toughening of polymer plastics using inorganic particles has some rather complicated aspects, in which the crack front bowing mechanism has been treated as the major toughening mechanism in inorganic particle filled thermosets. The crack bowing mechanism was first proposed by Lange [100]. According to this mechanism, the rigid particles in polymer composites will resist the propagation of the crack. The initial primary crack has to be bent between particles (bowing). The bowed secondary crack has more elastic energy stored than the straight unbowed crack. Therefore, more energy is needed for crack propagation in composites. This mechanism has successfully explained the toughening of polymers in many cases [101, 102]. However, the applicability of this mechanism is questionable in the case where the rigid particles in the order of 50 nm or less, because such small particles may not be able to resist the propagation of the crack [103].

Besides crack bowing mechanism, the micro mechanism regarding plastic deformation and particle debonding is widely accepted. In particulate-filled polymer nanocomposites, the micromechanisms leading to the plastic deformation are the debonding of particles (creating dimples) and the further plastic flow of the matrix zones, which are locally stretched until rupture by tearing. In general, the failure sequence can be briefly described in two steps as shown in Figure 1.2.20, i.e. formation of voids (debonding) and subsequent coalescence of voids under imposed load [104]. Assuming a poor adhesion between matrix and particles, the particles detach easily from the polymer matrix by creating voids.

With further plastic deformation, these voids grow in stress direction, forming dimple-like holes around the particles (step I). In the next stage of loading, the rest of the matrix deforms under shear conditions until the previous holes coalesce and final fracture occurs (Step II). The debonding in step I obviously depends on the filler shape (stress concentration effect) and on the filler-matrix adhesion. The strain levels in step II are considerably reduced by increasing filler volume fraction, and thus with decreasing interparticle distance [105].

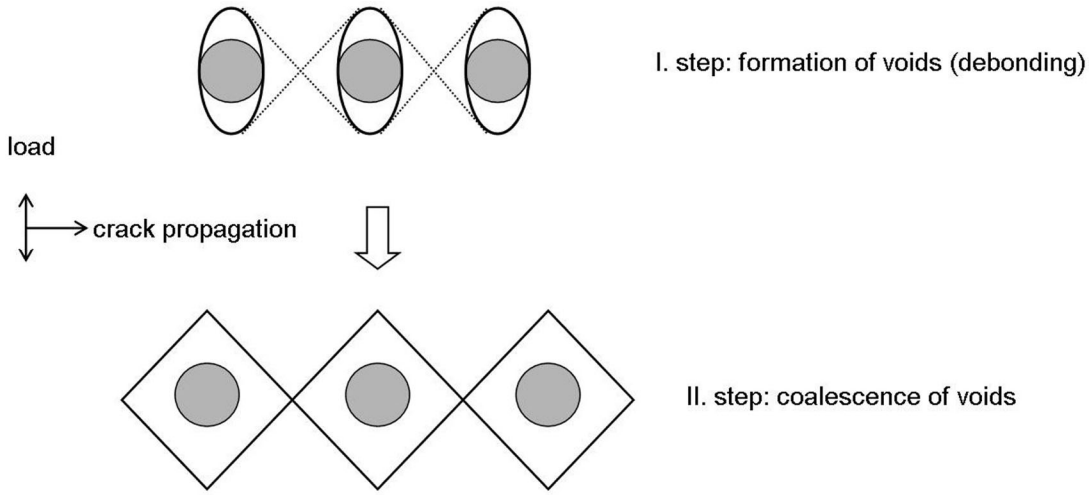

Figure 1.2.20: Stages of crack formation and propagation around rigid particles in a ductile matrix.

Interphase analysis and interfacial interactions

The mechanical properties of polymer composites depend crucially upon the efficiency of stress transfer from the polymer matrix to the fillers which will be influenced by the interphase. The interphase in composites is the boundary layer

between filler surface and polymer matrix which exhibits local properties different from those of the bulk matrix. Unlike fiber-reinforced composites, the interfacial behaviours in particulate-filled polymer composites are difficult to measure directly. Sumita and co-workers [106] used the energy dissipation in dynamic mechanical analysis (DMA) to identify the effective volume fraction (φ_e) of dispersed phase as well as the interphase thickness (Δr). In this case, the effective volume fraction of dispersed particles composes of the filler volume plus the region of the "immobilized" matrix associated with the interfaces as described in a simplified mode in Figure 1.2.21.

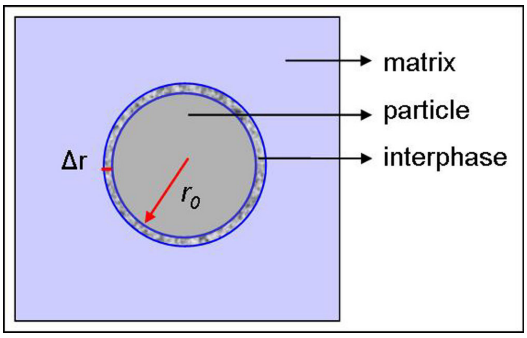

Figure 1.2.21: Scheme of interphase between polymer matrix and reinforcing particles [106].

It is thought that the interphase does not contribute to energy dissipation. Accordingly, the ratio of energy dissipated per cycle of vibration in a unit volume for the composite (W_c) to the unfilled system (W_0) is approximately:

$$\frac{W_c}{W_0} = \frac{1}{1-\varphi_e} \tag{1.13}$$

(W_C/W_0) is approximately equal to the ratio of loss modulus (E_c''/E_0''). A parameter *B* is used to describe the relationship of the effective volume (φ_e) and the real volume fraction (φ_f) of the filler. Thus, the equation (1.9) can be described as:

$$\frac{W_c}{W_0} = \frac{E_c''}{E_0''} = \frac{1}{1-\varphi_e} = \frac{1}{1-\varphi_f \cdot B} \tag{1.14}$$

$$B = (1+\frac{\Delta r}{r})^3 \tag{1.15}$$

where r is the radius of a dispersed single nanoparticle. Using these equations the effective volume fraction of particles as well as the interphase thickness in polymer composite can be determined.

Rong et al. [8] have used another model developed by Pukánszky and co-workers to predict the interfacial interactions in composites filled with particles:

$$\frac{\sigma_c}{\sigma_0} = \frac{1-\varphi_f}{1+2.5\cdot\varphi_f}\exp(B_f \cdot \varphi_f) \tag{1.16}$$

where σ_c and σ_0 are the tensile strengths of the polymer composite and the neat matrix, respectively, B_f is a parameter characterizing the interfacial interactions between polymer matrix and particles.

2 Objectives of the Study

In this study, two thermoplastics, i.e. amorphous polycarbonate and semi-crystalline polypropylene and one polyester-based thermoplastic elastomer (TPE) were used as polymer matrices. The composites filled with different spherical nanoparticles were produced by direct melt blending in a twin-screw extruder and then injection moulded. The morphological, thermal, mechanical and optical properties of all produced polymer composites were characterized.

The following objectives were considered:

1. Selected SiO_2 nanoparticles were incorporated into amorphous polycarbonate to enhance the thermal and mechanical properties of PC. Besides improvements in thermal and mechanical properties, the optical properties of PC should be maintained.
2. Surface-modified and unmodified SiO_2 and TiO_2 nanoparticles were introduced into semi-crystalline iPP. The goal was to investigate the influence of particle loading, particle surface polarity, particle content, and the chemical nature of particles on thermal and mechanical properties of iPP composites.
3. Different kinds of hydrophilic TiO_2 particles in different sizes were used as reinforcing fillers for TPE(PBT-PTMG). The objective was to study the effect of TiO_2 particles as a function of particle content and particle size on thermal and mechanical properties of TPE(PBT-PTMG)/TiO_2 composites.

According to the final results achieved, the structure-property relationships in respective polymer composites were investigated and discussed. An overview of the studied polymer composites is given in Figure 2.1.

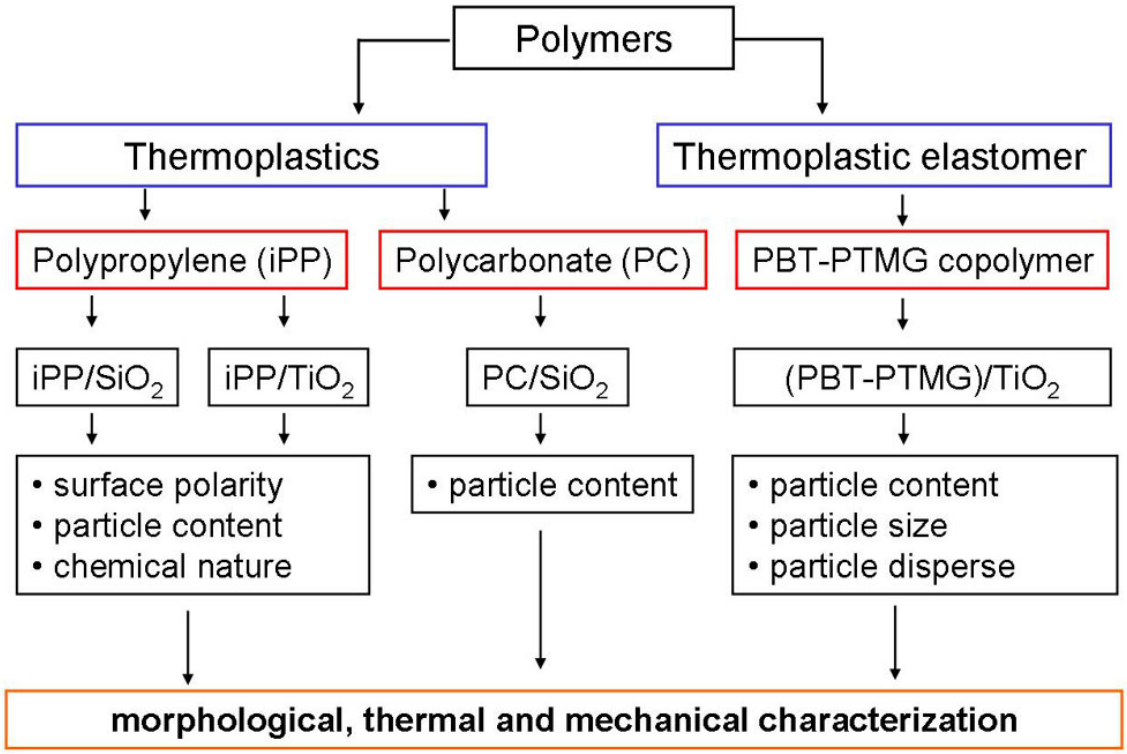

Figure 2.1: Overview of the studied polymer composites in this work.

3 Experimental

3.1 Materials

3.1.1 Polymer matrices

Granulated bisphenol-A PC was provided by Bayer AG, Germany (Makrolon 3105). Its melt flow rate and density are 6.0 g/10min and 1.20 g/cm^3, respectively. The refractive index at 589 nm light wavelength is 1.587. The chemical structure of this PC is shown in Figure 1.2.1 (chapter 1.2.1).

Homopolymer iPP granules were purchased from Lyondell-Basell Polymers (Moplen-HP 400R). The melt flow rate and the density of this iPP are 25 g/10min and 0.89 g/cm^3, respectively. The chemical structure of iPP is shown in Figure 3.1.

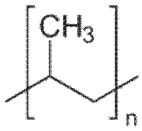

Figure 3.1: Chemical structure of iPP [48].

The granules of TPE(PBT-PTMG) block copolymer were friendly provided by Allod Werkstoff GmbH & Co. KG (Germany). The weight percent and molecular weight of soft PTMG segment in this copolymer are about 50% and 1000 g/mole, respectively. The chemical structure of this material is shown in Figure 1.2.4 (chapter 1.2.1).

3.1.2 Reinforcing particles

Aerosil® SiO_2 and Aeroxide® TiO_2 nanoparticles

Gas-phase synthesized SiO_2 and TiO_2 nanoparticles were provided from Evonik GmbH, Germany. The important characteristics of used nanoparticles are given in

Table 3.1.

Table 3.1: Important characteristics of Aerosil® SiO_2 and Aeroxide® TiO_2 nanoparticles

particle types	surface area [m^2/g]	primary diameter [nm]	carbon content [wt%]	Surface property
Aerosil® R106 (D4-SiO_2)	250	7	1.5-3.0	octamethylcyclotetrasiloxane-modified
Aerosil® 150 (C0-SiO_2)	150	14	0	unmodified, hydrophilic
Aerosil® R8200 (3C1-SiO_2)	160	12	2.0-4.0	hexamethyldisilazane-modified
Aerosil® R805 (C8-SiO_2)	150	12	4.5-6.5	octylsilane-modified
Aerosil® R816 (C16-SiO_2)	190	12	0.9-1.8	hexadecylsilane-modified
Aeroxide® P25 (C0-TiO_2)	50	21	0	unmodified, hydrophilic
Aeroxide® T805 (C8-TiO_2)	50	21	2.7-3.7	octylsilane-modified

The unmodified SiO_2 and TiO_2 nanoparticles (indicated as C0-particles) have hydrophilic nature with OH-groups on particle surface. After surface modification with silanes, the nanoparticles become more hydrophobic because of introduction of alkyl chains on the particle surface. Figure 3.2 shows the morphology of C0-SiO_2 and C0-TiO_2 nanoparticles before compounding into polymer matrices. It is evident that the small nanoparticles result in agglomeration in powder form. The surface-modified nanoparticles (indicated as D4-, 3C1-, C8-, and C16-particles according to the number and length of alkyl chains on particle surfaces) show similar size and spherical shape as C0-particles.

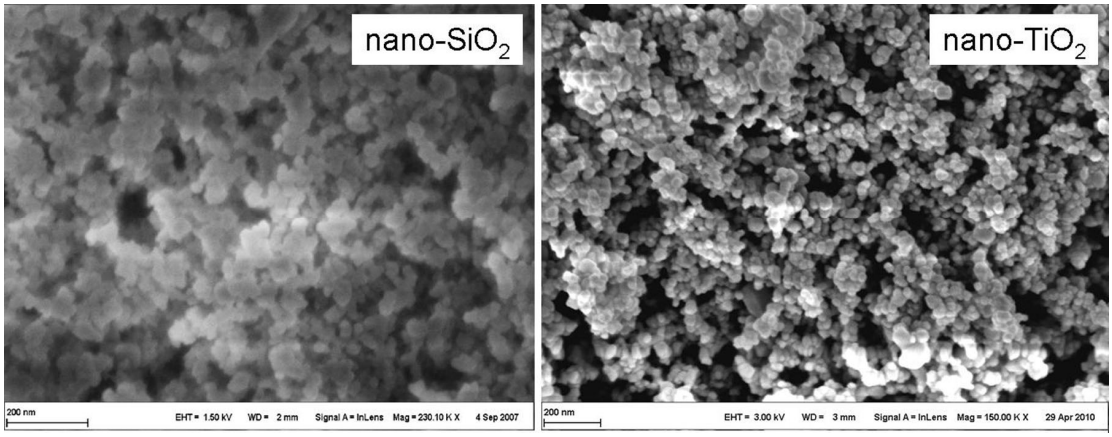

Figure 3.2: SEM micrographs of C0-SiO_2 and C0-TiO_2 nanoparticles before loading (scale: 200 nm).

TiO_2 (15 nm) particles

The TiO_2 (15 nm) nanoparticles were used as filler for TPE(PBT-PTMG). This type of nanoparticles was supplied by Sachtleben Chemie GmbH (Germany) under the trade name of HOMBITEC RM 300. According to supplier's information, HOMBITEC RM 300 is coated with Al_2O_3 and also includes an additional surface treatment (polyalcohol) to enhance dispersibility. The important characteristics of this nanoparticle type are listed in Table 3.2. The morphology of this particle type is shown in Figure 3.3. It can be seen that the nanoparticles result in agglomeration in powder form.

TiO_2 (300 nm) particles

In order to study the effect of particle size on thermal and mechanical properties of TPE(PBT-PTMG) composites, the TiO_2 (300 nm) particles under the trade name of Kronos® 2310 were used (Kronos International Inc. Germany). The TiO_2 (300 nm) particles were pre-treated with metal and metal oxides (total 4.0% Al_2O_3, 0.6% SiO_2

and 0.5% ZrO_2 in wt% referring to TiO_2 particle mass) before supplying. The important characteristics of this particle type are given in Table 3.2. Figure 3.3 shows the morphology of these particles before compounding into TPE(PBT-PTMG) matrix.

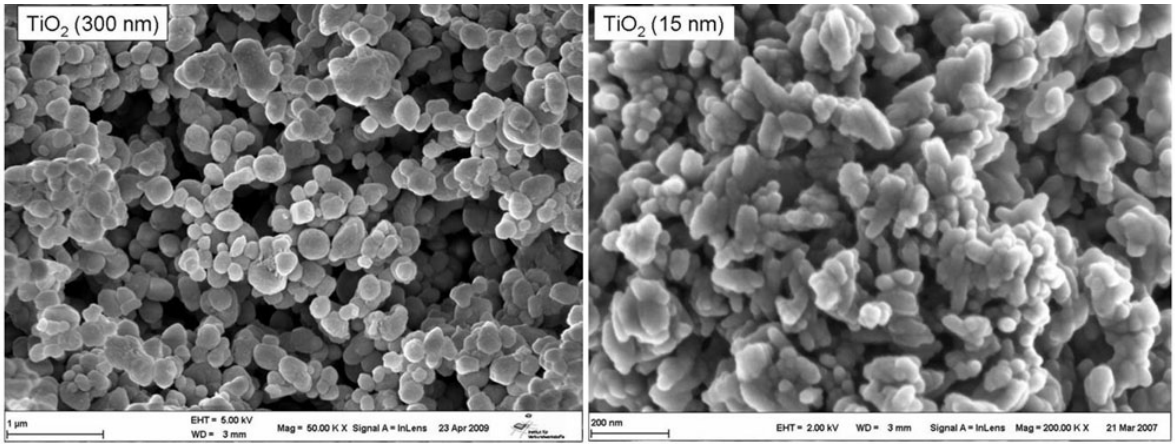

Figure 3.3: SEM micrographs of TiO_2 (300 nm) and TiO_2 (15 nm) particles.

Table 3.2: Important characteristics of different TiO_2 particles used for TPE(PBT-PTMG)

Particle type	C0-TiO_2 (21 nm)	TiO_2 (15 nm)	TiO_2 (300 nm)
TiO_2 content [wt%]	99.5	87	92.5
Crystal structure	rutile	rutile	rutile
Primary particle size	21 nm	15 nm	300 nm
Density [g/cm^3]	3.8	1.47	4.0
Specific surface area [m^2/g]	50	70	17
Surface treatment	no	Al_2O_3, polyalcohol	Al_2O_3, SiO_2
Surface nature	hydrophilic	hydrophilic	hydrophilic

3.1.3 Other materials used

The chemical solvents isopropanol (IPA, pro analysis), potassium permanganate, sulphuric acid (98%), and phosphoric acid (85%) were purchased from Merck KGaA Germany. Toluene (≥ 99.8%) was purchased from Fisher Scientific, United Kingdom. Methanol (99.5%) was purchased from Th. Geyer GmbH, Germany.

3.2 Preparation techniques for polymer composites

3.2.1 Direct melt compounding

Before compounding process, the polymer matrices and all particles were pre-dried in an oven at 80 °C for 48 h. The blending process was applied in a co-rotating twin-screw extruder (ZE-25A UTX, KraussMaffei Berstorff GmbH, Germany) with a screw-configuration as shown in Figure 3.4. The diameter of the screws was 25 mm and the length/diameter ratio (L/D) was 44.

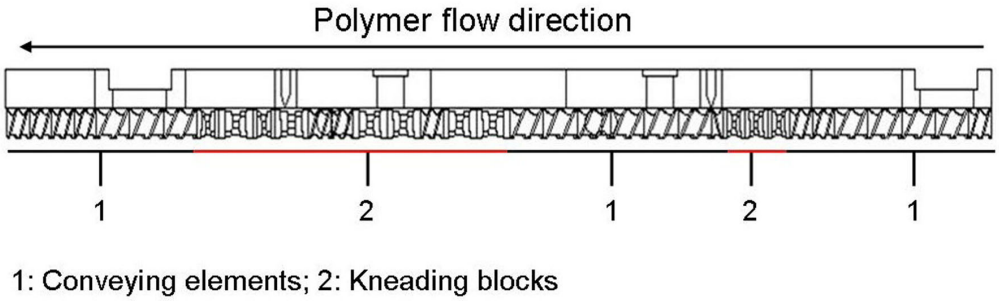

Figure 3.4: Screw-configuration for Berstorff co-rotating twin-screw extruder.

Firstly, the particles were blended into respective polymer melts to make a masterbatch with higher particle content. The masterbatches were twice extruded to ensure a better dispersion quality of particles. The composites with desired particle contents were then diluted from the respective masterbatches. That means all composites were three times extruded through twin-screw extruder as shown in Figure 3.5. Finally, the real particle contents in respective composites were determined using thermogravimetric analysis (TGA). All processing parameters and composites produced in this way are listed in Table 3.3.

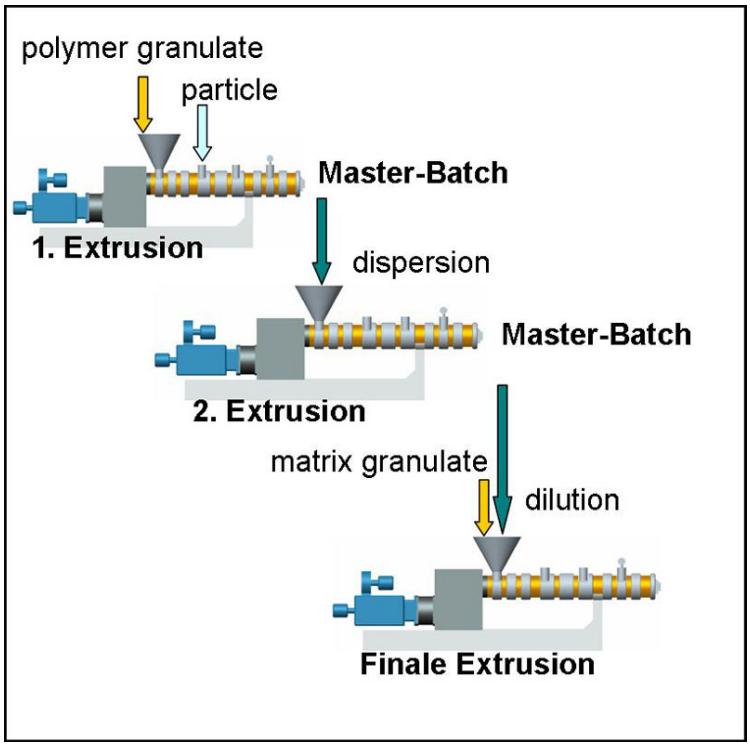

Figure 3.5: Schematical illustration of masterbatch technique by extrusion process.

Table 3.3: All materials prepared in this work

Sample designation	Particle content [Vol.-%]	Process temperature [°C]	Screw-speed [rpm]
neat PC	0	260-280	300
PC/D4-SiO_2	0.5 ~ 10	260-280	300
neat iPP	0	200-220	150
C0-iPP/SiO_2	2.3	200-220	150
3C1-iPP/SiO_2	2.3	200-220	150
C8-iPP/SiO_2	2.3	200-220	150
C16-iPP/SiO_2	2.3	200-220	150
C0-iPP/TiO_2	0.4, 0.8, 1.3, 2.3	200-220	150
C8-iPP/TiO_2	0.4, 0.8, 1.3, 2.3	200-220	150
neat TPE(PBT-PTMG)	0	200-210	250
TPE(PBT-PTMG)/TiO_2 (21 nm)	1.3, 2.6, 4.9	200-210	250
TPE(PBT-PTMG)/TiO_2 (300 nm)	2.6, 3.8	200-210	250
TPE(PBT-PTMG)/TiO_2 (15 nm)	2.6, 3.8, 4.9	200-210	250

3.2.2 Injection moulding

All composites produced in extruder were dried at 80 °C for 24 h before injection moulding process. The injection moulding was applied in an injection moulding machine (320 S 500-150, Arburg, Germany) as shown in Figure 3.6. The screw diameter was 35 mm and the length/diameter ration was 17. The parameters used by injection moulding for composites were the same ones as used by extruding process.

Figure 3.6: Arburg injection moulding machine and used mold templates.

3.3 Structural/morphological characterization

3.3.1 Scanning electron microscopy (SEM)

The dispersion of nanoparticles and the fractured surfaces of test specimens were examined by using SEM (JEOL JSM-6300 and Hitachi S5200). The size and structure of iPP spherulites in neat matrix and composites were also studied using SEM. The samples were etched before SEM examination in an etchant composed of 1 wt% potassium permanganate in a mixture of concentrated sulphuric acid and phosphoric acid in a 3:2 volume ratio. The etch time was 3 h at room temperature. After etching, the samples were cleaned in distilled water and acetone and then dried. All sample surfaces were sputtered with a thin gold film prior to SEM examination.

3.3.2 Optical microscopy

Optical microscopy (Highlight 3000, Olympus Europe) with a low magnification was used for some cases, such as to examine the fracture surfaces and the craze initiation behaviour in polymer composites.

3.3.3 Micro-computerized tomography (µCT)

The spacial dispersion of respective particles in polymer matrices was determined by means of µCT method (Phoenix x-ray systems + services GmbH, Wunstorf, Germany). Using this method, a three-dimensional dispersion of particles in polymer matrix was obtained. The maximum resolution of this instrument is 500 nm.

3.3.4 Image analysis software

Based on SEM images, the distribution of particles in the polymer matrix and the amount percentage of particles in each distributive range are determined using Image

analysis software (Olympus SIS).

3.4 Hydrophobicity measurements of surface-treated nanoparticles

The nanoparticles, whose surfaces are modified with non hydrolyzable organic groups, will usually not be wetted by water. However, these nanoparticles can be wetted by a methanol/water mixture. The weight percentage of methanol in this methanol/water mixture is a measure for the hydrophobicity of nanoparticles [107]. Accordingly, the relative hydrophobicity of modified SiO_2 and TiO_2 nanoparticles used in this work was measured as follows: 200 mg nanoparticles and 50 g water were mixed in a 250 ml beaker. If the particles are hydrophobic enough, they will remain on the water surface. Then methanol (99.5%) was slowly added into the liquid phase of the mixture using an injection needle. During addition of methanol, the mixture in beaker was constantly stirred. A direct contact between the nanoparticles and pure methanol should be avoided. The process was finished when the nanoparticles were totally dispersed in the methanol/water phase and a relative clear suspension was obtained. The hydrophobicity of respective nanoparticles indicated by methanol-wettability can be calculated using the following equation:

$$\frac{m_m}{m_m + m_{H_2O}} \cdot 100\% \tag{3.1}$$

where m_m is the amount of methanol used in gram, and m_{H_2O} is the mass of water (50 g).

3.5 Thermal and thermo-mechanical characterization

3.5.1 Differential Scanning Calorimetry (DSC)

DSC measurements were performed using a DSC 821 instrument (Mettler-Toledo GmbH, Giessen, Germany) under nitrogen atmosphere. The following procedure was used for iPP composites: each sample was heated from 50 °C to 200 °C at a heating rate of 10 °C/min and then held at 200 °C for 5 min to ensure an identical thermal history. The specimen was subsequently cooled down to room temperature at a cooling rate of 10 °C/min. For TPE(PBT-PTMG) samples, the same procedure was used except that the temperature range varied from -100 °C to 250 °C. The melting temperature T_m, the crystallization temperature T_c and the crystalline enthalpy ΔH_m of materials were obtained from the maximum and the area under the exothermic peaks, respectively. The crystallinity X_c of iPP was determined as:

$$X_c = \frac{\Delta H_m}{\Delta H_m^0} \times 100\% \tag{3.2}$$

where ΔH_m^0 is the theoretical crystalline enthalpy for 100% crystalline iPP which is taken to be 209 J/g [108].

3.5.2 Thermogravimetric analysis (TGA)

All samples were dried at 80 °C in an oven for 24 h prior to TGA analysis. The tests were performed using a DTG-60 instrument (SHIMADZU Corp.) under nitrogen atmosphere in a temperature range from 50 °C to 550 °C at a heating rate of 15 °C/min for all samples. In the given temperature range, only organic substances could decompose, the inorganic particles would remain in the residue because of their decomposition temperatures higher than 1000 °C according to supplier's information. The thermal stability and the weight loss of respective samples were obtained.

3.5.3 Dynamic mechanical thermal analysis (DMTA)

DMTA tests were carried out using a Gabo Qualimetrer Explexor 25N machine under tension mode. The tests were run with a frequency of 10 Hz and heating rate of 2 °C/min for all samples. The specimens were prepared in a dimension of 10 x 30 x 4 mm^3 (width x length x thickness). The temperature ranges for respective polymer matrices were set as follows: from -20 °C to 140 °C for iPP samples, from -100 °C to 150 °C for TPE(PBT-PTMG) samples and from -30 °C to 180 °C for PC samples. After DMTA tests, the storage- and loss modulus (E', E"), the loss factor tanδ and the glass transition temperatures T_g were obtained.

3.6 Mechanical characterization

3.6.1 Tensile test

The tensile test was performed using a universal testing machine (Zwick 1474, Roell, Germany) at room temperature. Dog-bone-shaped specimens were prepared according to DIN EN ISO 527-2-1A as shown in Figure 3.7. The crosshead speed was 4 mm/min for all samples. The tensile modulus E was determined by using a clip-on extensometer between 0.05% and 0.25% linear elongation.

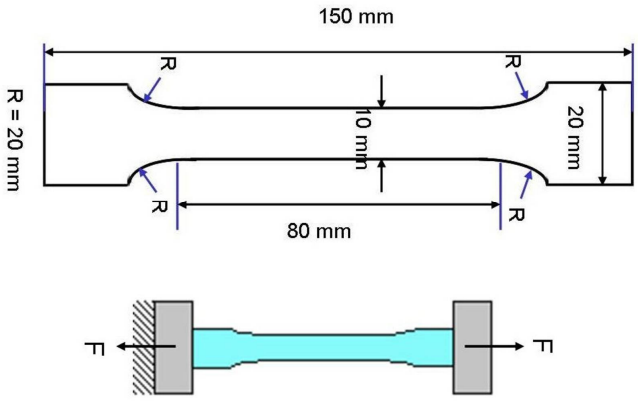

Figure 3.7: Dimension of tensile specimens and direction of tensile force.

3.6.2 Three-point bending test

The flexural properties of some samples were examined by using three-point bending test according to standards DIN 53452 and DIN EN ISO 178 at the same universal testing machine Zwick 1474 (Roell Ulm, Germany) at room temperature in air. The bend direction with respect to samples by testing is shown in Figure 3.8. The distance between two supports is 64 mm. All tests were run at a cross-head speed of 1 mm/min. The related flexural modulus, flexural strength at yield and flexural elongation at yield were determined.

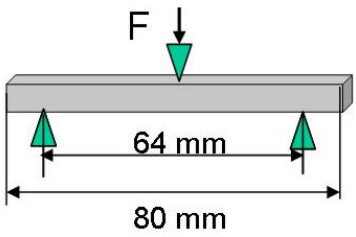

Figure 3.8: Dimension of three-point bending specimens and direction of bend force.

3.6.3 Charpy impact test

Charpy impact test was performed at room temperature by using an impact tester (AFS-MK fracto scope of Ceast, Torino, Italy) equipped with a pendulum hammer of 1 kg in weight. The striker energy and velocity at impact point were 4 J and 2.9 m/s, respectively. The support distance was 40 mm. The samples were prepared according to ISO 179 with a dimension of 10 x 4 x 80 mm^3 (thickness x width x length). The V-shaped notch in the middle of the samples was 1.5 mm in depth. The dimension of the samples and the direction of impact force with respect to the notch are shown in Figure 3.9.

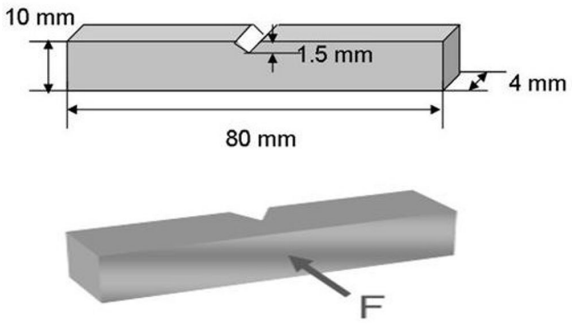

Figure 3.9: Dimension of impact specimens and direction of impact force with respect to the notch.

3.6.4 Compact tension test (CT)

CT examination was performed at room temperature using the same Zwick testing machine mentioned above. The testing rate was 0.3 mm/min for all samples. The test specimens were prepared according to ASTM D5045-99 and ASTM E399-90 standards (36 x 36 x 4 mm^3) as shown in Figure 3.10.

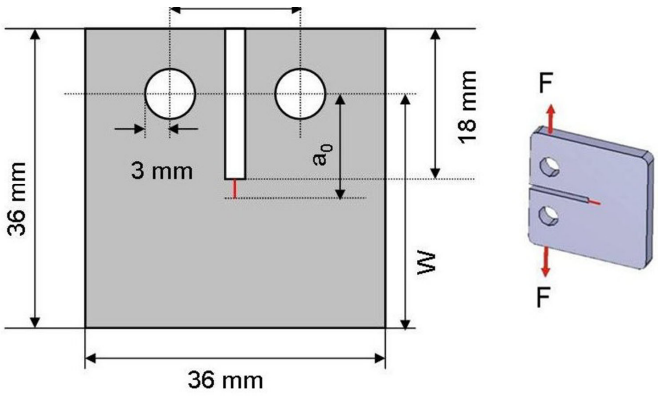

Figure 3.10: Dimension of CT samples prepared according to respective standards.

The sharp pre-crack was made by knocking a razor-blade into the samples saw slot. The initial crack length a_0 and the ligament length W should be prepared in such a way that the condition $0.45 < a_0/W < 0.55$ was satisfied for plane-strain condition

according to above standards. The specific fracture toughness K_{IC} and the energy release rate G_{IC} were calculated as [109, 110]:

$$K_{IC} = \frac{F_{Q,\max}}{B \cdot \sqrt{W}} \cdot f(a_0/W) \tag{3.3}$$

$$G_{IC} = \frac{(1-\upsilon^2)K_{IC}^2}{E'} \tag{3.4}$$

where $f(a_0/W)$ is a tabulated correction function according to ISO 13586, *B, W* and a_0 are specimen dimensions (thickness, ligament length and pre-crack length, respectively), $F_{Q,\max}$ is the maximum force in the force-displacement curve, v is the Poisson coefficient which were taken as 0.35 for PC [111] and 0.45 for PP [112]. E' is the storage modulus obtained from DMTA tests.

3.6.5 Resistance against environmental stress cracking (ESC)

In order to investigate the crack propagation behavior and the rupture time (lifetime) of neat PC and PC/D4-SiO_2 composites in different environments, a crack opening displacement (COD) method was applied by using a developed creep machine equipped with an environmental chamber allowing complete immersion of pre-crack in samples in environment as shown in Figure 3.11. The samples for COD tests were exactly prepared as the CT samples with the dimension shown in Figure 3.10. The static loading was constant of 80 N. The crack opening distance, the load force and the test time were automatically recorded using an extensometer throughout each test. For comparison, isopropanol (IPA) and toluene were used as chemical environments due to their different diffusion rates in PC [113]. All tests were run at 23 °C.

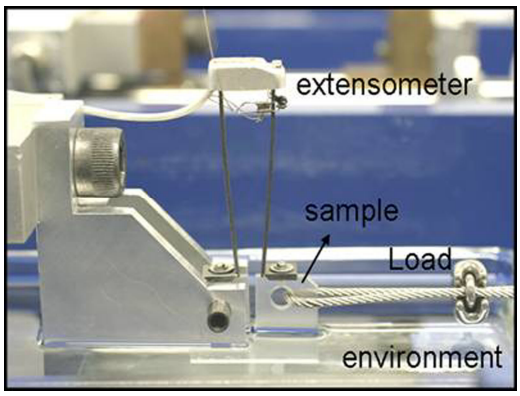

Figure 3.11: Equipment for COD test of PC samples under static constant loading in different environments.

3.6.6 Bent strip test

In order to study the craze initiation behaviour in polymer composites, a bent strip test was performed according to ISO 4599. The sample strips prepared according to ISO 179 standard (80 x 10 x 4 mm^3) were fixed on bending-templates with a radius of 96 mm as shown in Figure 3.12.

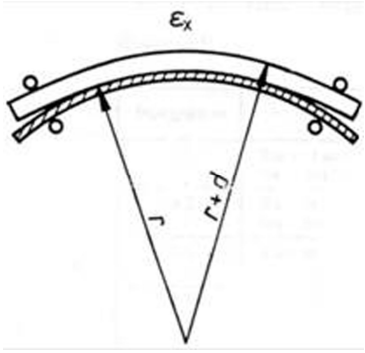

Figure 3.12: Scheme of bent strip test with defined strain in outer surface of samples.

The constant outer surface strain of samples is 2.0% calculated using the following equation:

$$\varepsilon = \frac{d}{2r + d} \tag{3.5}$$

where ε and d are the outer surface strain and the thickness of sample strips, respectively, r is the radius of bending-templates. The tests were run at 23 °C for 72 h.

3.6.7 Creep test

Short-term creep tests were performed for TPE(PBT-PTMG) composites using a DMA Q800 apparatus under tension mode at temperatures ranging from 0 °C to 80 °C. Isothermal tests were run by increasing the temperature stepwise of 10 °C. Before the creep measurements, each specimen was equilibrated at each temperature for 5 min and then tested for 12 min. The tensile stress for all samples was 0.5 MPa which was derived from a test series checking the presence of linear isochronous deformation. The specimens dimension was 10 x 2 x 30 mm^3 (thickness x width x length). The creep compliance was obtained as a function of time and temperature. In order to get long-term creep behaviour of materials, the time-temperature superposition (TTS) principle was adopted.

3.7 Optical characterization

The optical properties of PC samples were determined according to ASTM D1003 and ASTM D1044 standards using a testing instrument from BYK-Gardner GmbH, Germany. The samples were prepared with a dimension of 60 x 60 x 2 mm^3 (length x width x thickness). The light wavelength used was 589 nm. The total light transmittance, the haze and the clarity of PC samples were obtained.

At least five specimens were tested for all measurements. Finally, the average values were taken and discussed.

4 Results and Discussion

4.1 Properties of PC/D4-SiO_2 nanocomposites

According to supplier's information, the octamethylcyclotetrasiloxane-modified Aerosil® SiO_2 (D4-SiO_2) type is very suitable as filler in transparent polymers such as PC to maintain the transparency of matrix. The refractive indices of used PC and D4-SiO_2 nanoparticles are 1.58 and 1.45, respectively. The properties of PC/D4-SiO_2 composites were characterized and discussed as follows.

4.1.1 Particle dispersion of D4-SiO_2 nanoparticles in PC matrix

SEM examination was performed in this work to investigate the dispersion quality of nanoparticles in polymer matrix. As already mentioned in chapter 1, the primary nanoscale particles are due to strong von Walls forces not isolated to each other but building up aggregates and agglomerates which cannot be broken down easily by shear forces applied by application. The SEM micrographs in Figure 4.1.1 show the surface morphology of PC/D4-SiO_2 composites filled with 2- and 4 Vol.-% of nanoparticles.

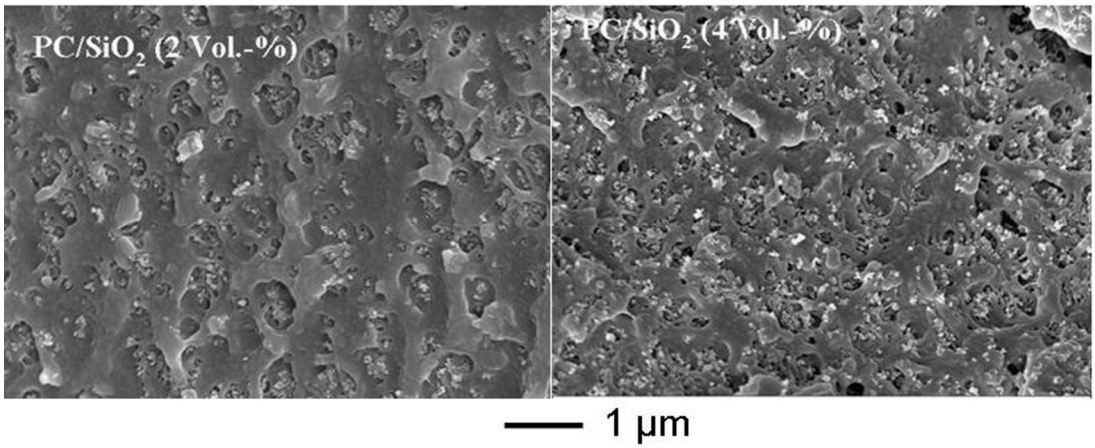

Figure 4.1.1: SEM micrographs of PC/D4-SiO_2 composites containing 2- and 4 Vol.-% of SiO_2 nanoparticles.

It can be seen that the nanoparticles and their small agglomerates (< 500nm) are well distributed in PC matrix. The nanoparticles/agglomerates are mainly dispersed within nanoscale range (< 100nm). According to SEM examination, the number of D4-SiO_2 agglomerates increases with increasing particle content as expected. On the cryofracture surfaces of composite samples as shown in Figure 4.1.1, the nanoparticles/agglomerates are easily debonded from PC matrix indicating relative poor adhesion between PC matrix and D4-SiO_2 particles. A potential explanation is that the dispersability of D4-SiO_2 nanoparticles in PC is strongly affected by different chemical nature of PC matrix and particles, because bisphenol-A PC show a more hydrophilic nature due to polar carbonate groups in molecules, whereas D4-SiO_2 nanoparticles are hydrophobic after surface modification with siloxanes. On the other hand, the presence of agglomerates shows that the shear forces during melt compounding process were not effective enough to break down such particle agglomerates.

4.1.2 TGA results

The thermal stability of PC and its composites are determined by TGA. The respective data such as the onset temperature for decomposition of matrix molecules, and the temperatures regarding 20% and 50% weight loss are listed in Table 4.1. Obviously, the incorporation of D4-SiO_2 nanoparticles in PC significantly increases the thermal resistance of PC composites indicated by increased T_{onset} values of PC nanocomposites. Furthermore, the thermal stability of PC/D4-SiO_2 composites increases with increasing particle content. At 5.0 Vol.-% of D4-SiO_2 nanoparticles, the improvement in T_{onset} of composite is by 14.8 °C, and the improvements in $T_{20\%}$ and $T_{50\%}$ also attain 14.8 °C and 12.4 °C, respectively.

Table 4.1: Thermal stability of neat PC and PC/D4-SiO_2 composites obtained by TGA

Samples	T_{onset} [°C]	$T_{20\%}$ [°C]	$T_{50\%}$ [°C]
neat PC	510.3	517.3	538.1
PC/D4-SiO_2 (0.5 Vol.-%)	511.6	519.6	539.4
PC/D4-SiO_2 (1.0 Vol.-%)	513.8	521.0	539.5
PC/D4-SiO_2 (2.5 Vol.-%)	517.5	527.1	545.9
PC/D4-SiO_2 (5.0 Vol.-%)	525.1	532.1	550.5

4.1.3 DMTA results

The DMTA was used to investigate the dynamic-mechanical thermal properties of polymer composites. Figure 4.1.2 shows the DMTA results of neat PC and

PC/D4-SiO_2 composites.

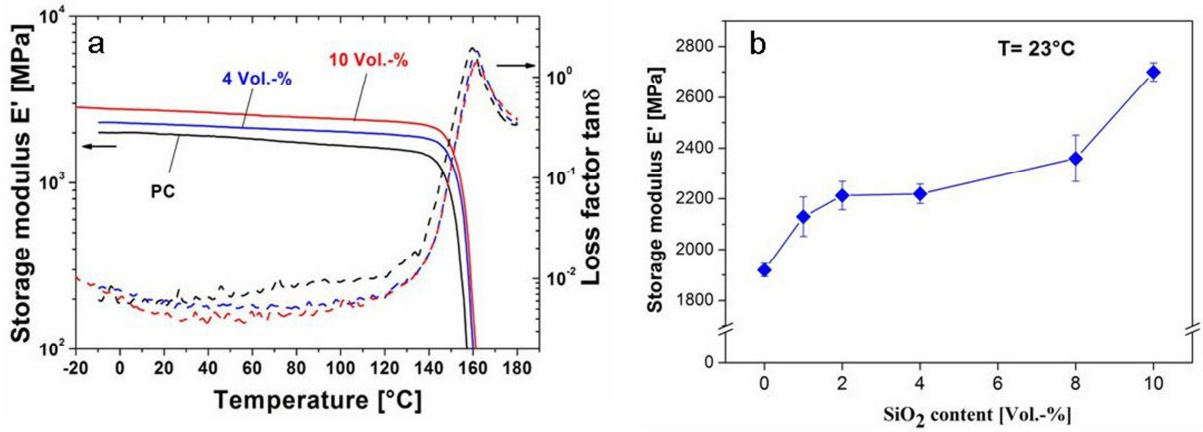

Figure 4.1.2: DMTA results: (a) the storage modulus E' and the loss factor tanδ as a function of temperature, (b) the storage modulus E' at 23 °C as a function of D4-SiO_2 particle content.

From Figure 4.1.2a, it is evident that the incorporation of D4-SiO_2 nanoparticles into PC significantly increases the storage modulus E' of matrix over the whole temperature range, indicating a stiffening effect of D4-SiO_2 nanoparticles. The E' value of PC composites increases with increasing nanoparticle content as shown in Figure 4.2b. For example, by incorporating 10 Vol.-% of nanoparticles, the storage modulus E' at 23 °C is improved by 40% compared to neat PC. On the other hand, the maximum peaks in tanδ curves of PC composites also shift to higher temperatures in comparison to neat PC. The glass transition temperatures T_g of composites, which are derived from the maximum peak values of loss factor tanδ, are overall increased up to 2 °C. The elevation of T_g can be related to the reduction in mobility of macromolecular chains of PC matrix caused by nanoparticles, but the improvements in T_g of PC/D4-SiO_2 composites are small concerning the relative poor adhesion between PC and D4-SiO_2 nanoparticles.

4.1.4 Mechanical properties

Tensile properties

The tensile properties of PC/D4-SiO_2 composites are shown in Figures 4.1.3 (a-c).

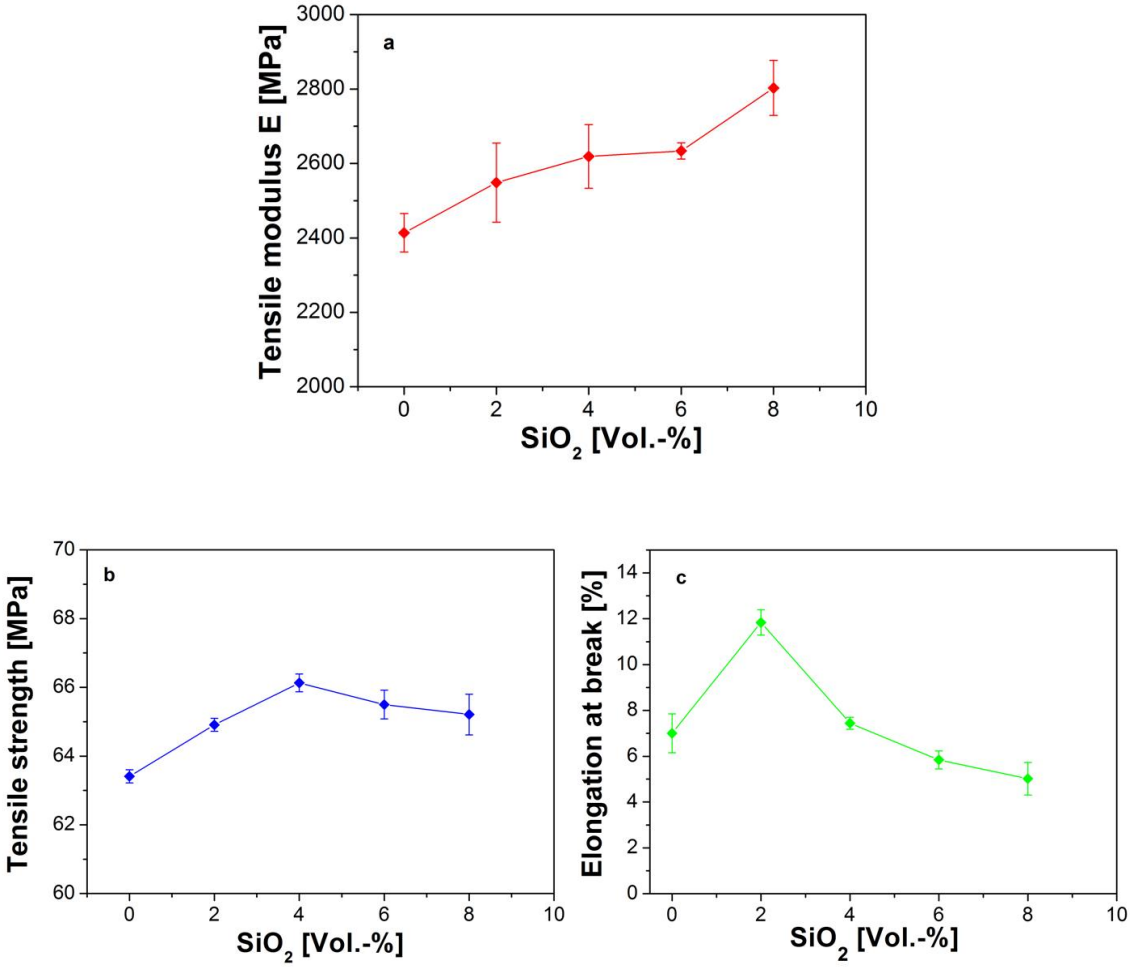

Figure 4.1.3: Tensile properties of PC/D4-SiO_2 composites as a function of particle content: (a) tensile modulus, (b) tensile strength and (c) elongation at break.

From Figure 4.1.3a, the tensile modulus E increases with increasing particle content due to stiffening effect of D4-SiO_2 nanoparticles. At 8 Vol.-% of particles, the improvement of tensile modulus is only about 14% due to the low matrix-particle interaction. The tensile strength as a function of nanoparticle content is displayed in

Figure 4.1.3b. Firstly, the tensile strength of composites increases with increasing particle content up to 4 Vol.-%, and then decreases with higher particle loading. All composites show improved tensile strength compared to neat PC. According to [114], the dependence of tensile strength on particle content is attributed to increasing number of particle agglomerates with increasing particle content in PC matrix, which can cause a higher degree of failures under imposed loading due to stress concentration effects of particles. Generally, the ductility of polymers should be reduced by incorporation of inorganic fillers, especially as agglomerates, indicated by a decrease of elongation at break [115]. However, the values of elongation at break of PC/D4-SiO_2 composites containing 2- and 4 Vol.-% of D4-SiO_2 particles are increased compared to neat PC, especially at 2 Vol.-% at which the improvement in elongation at break is by 69% as shown in Figure 4.1.3c. This can be explained that the nanoparticles are well-distributed in PC matrix acting as “plasticizers”, by what the ductility of polymer composites will be increased [116]. On the other hand, increasing particle content leads to decreased elongation at break of PC/D4-SiO_2 composites due to increased stiffness of composites. The results of tensile tests are listed in Table 4.2.

Table 4.2: Summarized results of tensile tests of PC/D4-SiO_2 nanocomposites

Particle content (Vol.-%)	Tensile modulus E (MPa)	Tensile Strength σ (MPa)	Elongation at break ε (%)
0	2413.91 ± 52.01	63.41 ± 0.19	7.00 ± 0.85
2	2548.60 ± 106.37	64.91 ± 0.20	11.84 ± 0.55
4	2619.15 ± 85.30	66.13 ± 0.26	7.44 ± 0.26
6	2672.40 ± 102.17	65.50 ± 0.42	5.84 ± 0.39
8	2803.03 ± 73.66	65.21 ± 0.59	5.02 ± 0.71

Fracture toughness K_{IC} and morphology

The typical load-displacement curves of neat PC and PC/D4-SiO_2 composites are shown in Figure 4.1.4a. It can be seen that the nanocomposite filled with 4 Vol.-% of particles exhibits the highest load maximum. Compared to neat PC, the displacement at force maximum of PC/D4-SiO_2 composites is clearly increased at 2- and 4 Vol.-% of D4-SiO_2 particles, whereas the displacement at maximum force is decreased at 8 Vol.-% of particles. Correspondingly, the fracture toughness K_{IC} and the energy release rate G_{IC}, which were calculated from the load maximum, show slight increases at low nanoparticle contents (1- and 2 Vol.-%) compared to neat PC as shown in Figure 4.1.4b. At 4 Vol.-% of D4-SiO_2 particles, the PC/D4-SiO_2 composite shows the maximum improvements of K_{IC} and G_{IC} by 43% and 86%, respectively. A further increase of particle content at 8 Vol.-% does not lead to a further improvement in fracture toughness.

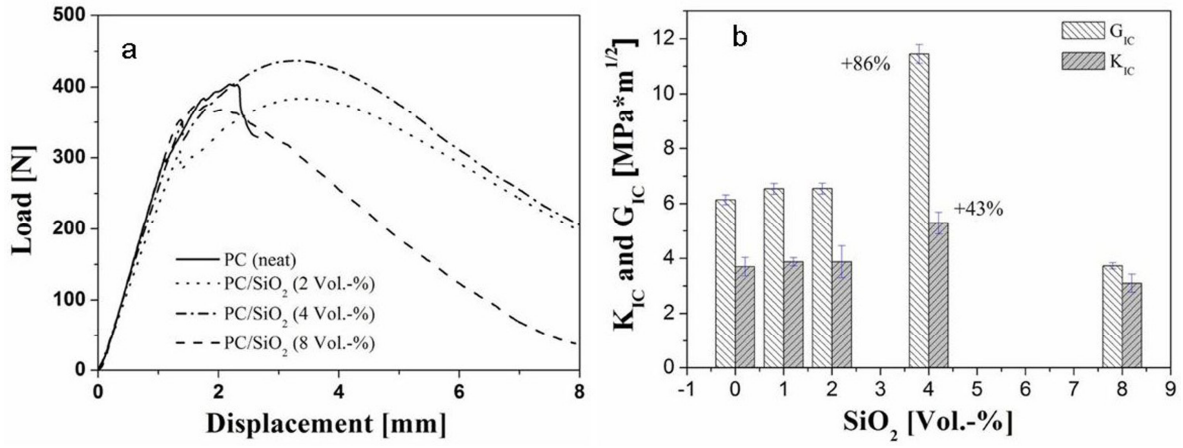

Figure 4.1.4: Results of CT tests: (a) load-displacement curves, (b) fracture toughness and energy release rate as a function of particle content.

SEM fractographs of failed CT-specimens give detailed information on the fracture mechanisms and might explain the change of PC fracture toughness after addition of D4-SiO_2 nanoparticles. Figure 4.1.5 shows the fracture surfaces of neat PC and PC/SiO_2 nanocomposite containing 4 Vol.-% of particles. Near the crack tip on the fracture surface of neat PC, intensive deformation of matrix and river-like crack arrest lines are observed. The regular crack arrest lines are typical features for a fracture surface of neat PC (Figures 4.1.5 a-b) [117]. By contrast, numerous dimples occur near the crack tip on the fracture surfaces of all PC/D4-SiO_2 composites as shown in Figure 4.1.5c. In the centre of such dimples, particles/agglomerates are found as marked in Figure 4.1.5d-e, which might serve as stress concentrators in polymer matrix, promoting the formation of those dimples [118, 119]. The formation of such dimples in polymer composites is accompanied by energy dissipation events, such as localized micro-deformation of polymer matrix and particle debonding [119]. This extra energy dissipation during fracture process leads to improvements in fracture

toughness of polymer composites containing proper particle contents [120].

It is also observed that the density of dimples on the fracture surfaces of PC composites increases dramatically with increasing D4-SiO_2 content as shown in Figure 4.1.6. At 8 Vol.-% of particles, more dimples can create much more voids (defects) on the fracture surface of PC composite, promoting macro-crack propagation and impairing the plasticity of PC matrix [118]. As a result, the fracture toughness K_{IC} of this composite is decreased.

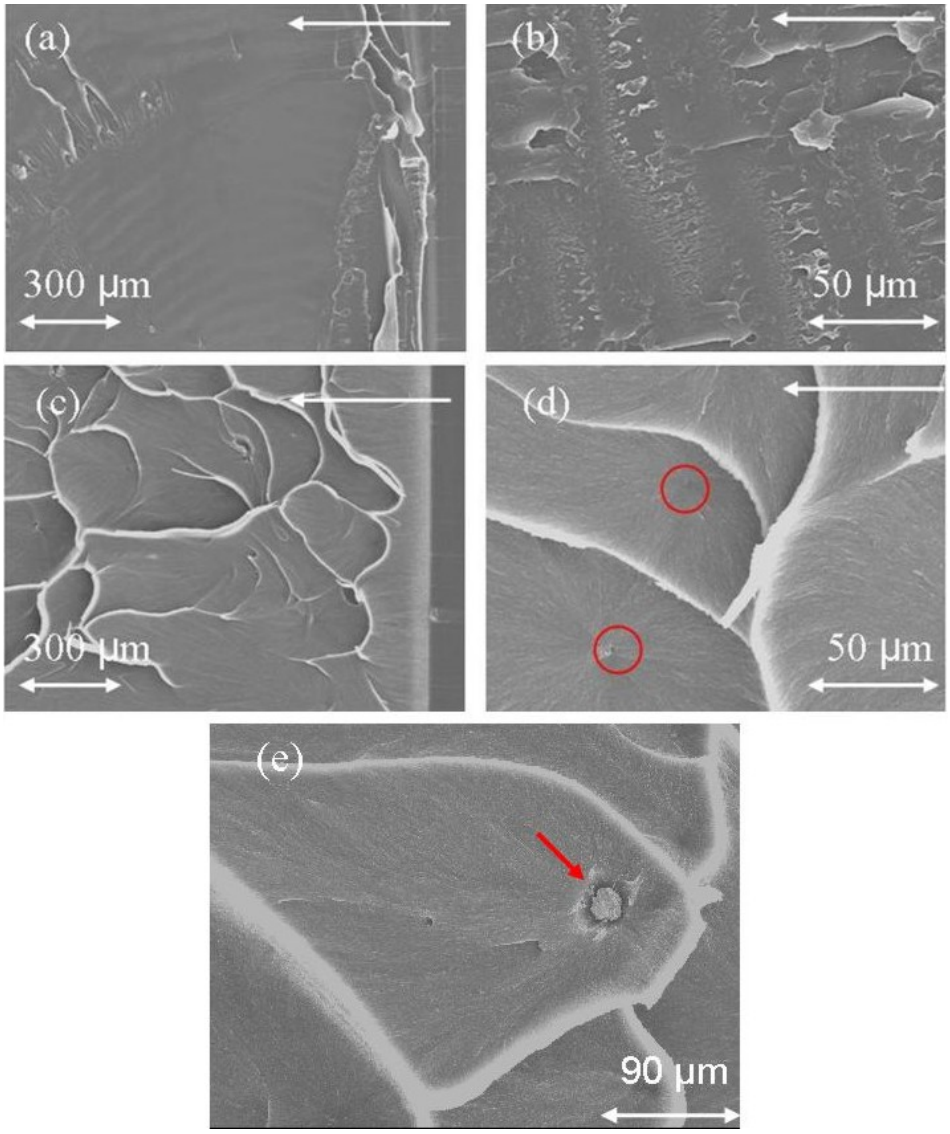

Figure 4.1.5: Morphology of fracture surfaces of CT-samples: (a) and (b) neat PC; (c), (d) and (e): PC/D4-SiO_2 composite filled with 4 Vol.-% of nanoparticles. The arrows in the pictures indicate the direction of crack propagation.

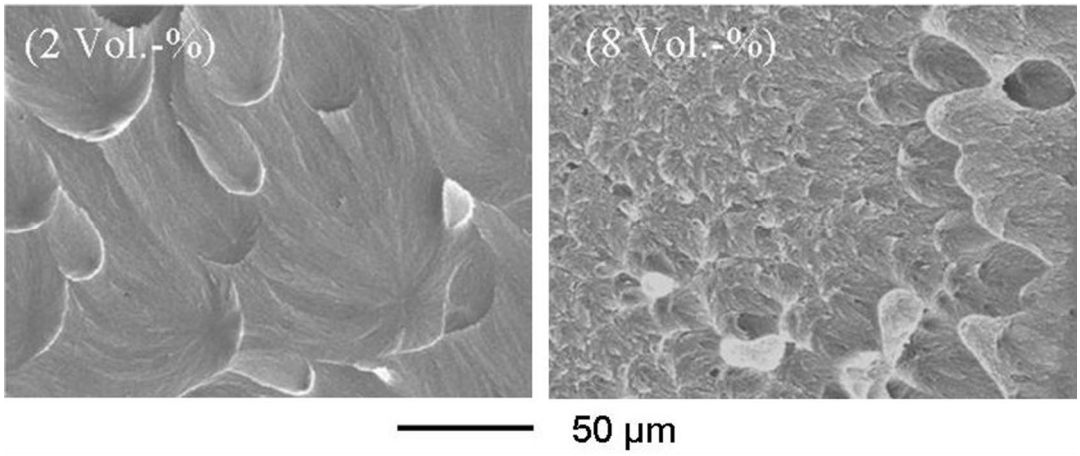

Figure 4.1.6: Increased number of dimples on the fracture surface with increased SiO_2 particle content.

Resistance against ESC

The resistance of PC samples against stress cracking in critical environments is indicated by the life-time of samples (time to sample failure) via COD testing (crack opening distance). The values of COD and constant force as a function of test time obtained in IPA and in toluene are shown in Figure 4.1.7. By testing in IPA, both neat PC and PC/D4-SiO_2 composites could stand for a long time without rupture (over 48 h). Figure 4.1.7a shows the curves of PC/D4-SiO_2 composite containing 2 Vol.-% of D4-SiO_2 particles as an example, other PC composites show a similar shape of COD curves because of slow crack-propagation. On the contrary, the pre-crack propagated quickly in toluene, indicated by a quick arising of COD value as shown in Figure 4.1.7b. In the case of sample failure, the curve of COD rises abruptly, and at the same time the curve of force falls steeply to zero. All PC samples tested in toluene were completely ruptured along the pre-crack after less than two hours. Comparing the Figures 4.1.7a and 4.1.7b, one can conclude that the environmental effect of toluene on stress-crack propagation in PC is much stronger than that one of IPA. The values

of life-time of neat PC and PC/D4-SiO_2 composites tested in toluene are shown in Figure 4.1.8 as a function of particle content. It can be seen that all PC/D4-SiO_2 composites show remarkably improved life-time values compared to neat PC. At 4 Vol.-% of particles, the life-time of PC/D4-SiO_2 composite runs through a maximum with an improvement by +118%.

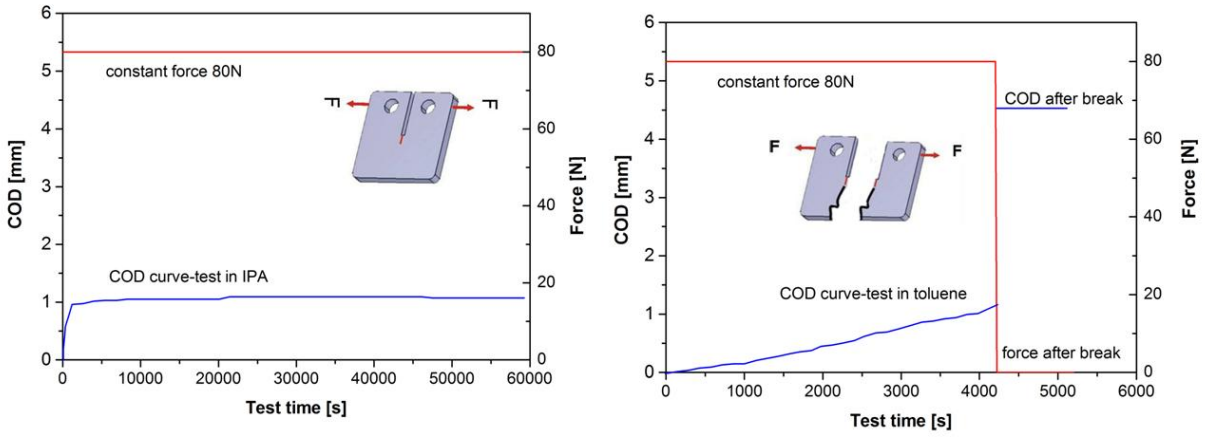

Figure 4.1.7: COD and constant force as a function of test time obtained in (a) IPA and in (b) toluene. PC/D4-SiO_2 nanocomposite containing 2 Vol.-% of nanoparticles is taken as an example.

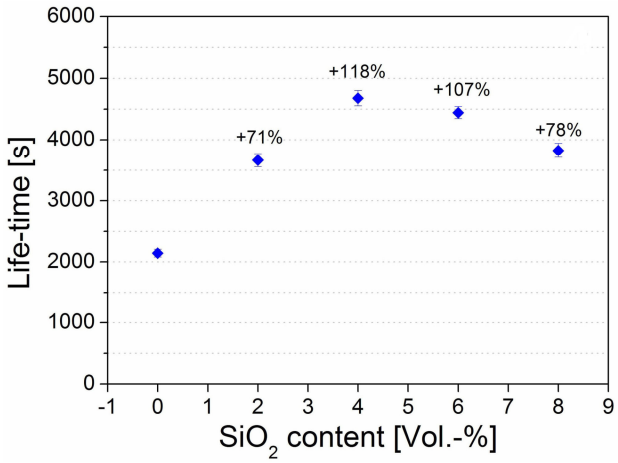

Figure 4.1.8: Life-time of PC and PC/D4-SiO_2 composites tested in toluene.

Figure 4.1.9 shows the fracture surfaces of failed neat PC and PC/D4-SiO_2 composite containing 6 Vol.-% of particles tested in toluene as examples. It can be seen that numerous large voids appear on the fracture surfaces of both samples, especially on the fracture surface of neat PC (Figure 4.1.9a). It was reported that the main mechanism for the formation of voids in environments is diffusion and swelling of chemical solvents into polymers [8]. Accordingly, diffusion and swelling of toluene within PC matrix created a large number of voids, promoting further localized diffusion along voided zones. These voids could rapidly propagate as cracks/failures under constant loading. As reported in [121], the particles and their agglomerates within polymer matrix could in some degree prevent solvent diffusion and swelling, preventing the formation of more voids as shown in Figure 4.1.9b. As a result, the incorporation of D4-SiO_2 nanoparticles in PC exhibits significant improvements in resistance to ESC of PC composites in toluene. On the other hand, stress-crazing by liquids usually results in rapid and catastrophic failure. According to [113], toluene has a much higher diffusion coefficient in PC than IPA, and IPA does not craze PC. Accordingly, the PC samples have much longer life-time in IPA than in toluene.

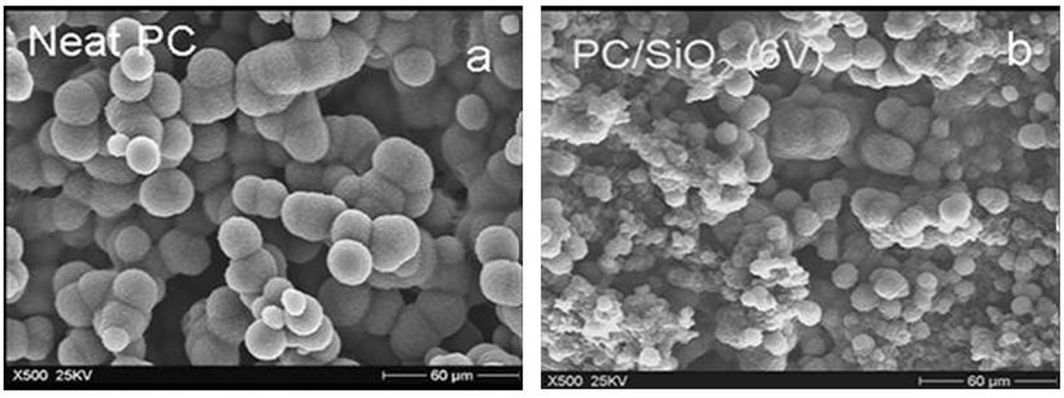

Figure 4.1.9: Fracture surfaces of neat PC (a) and PC/D4-SiO_2 composite containing 6 Vol.-% of particles (b) tested in toluene.

Craze initiation behaviour

Two series of bent strip tests running in air and in IPA were designed for PC samples. The reasons for use of IPA as an environment are as follows: firstly, IPA is one of the most used chemical agents in which PC can keep a long time without damage as shown in ESC test results; secondly, IPA does not craze PC [113].

Figure 4.1.10 shows optical micrographs of bent strip samples tested in air and in IPA. It is evident that all PC samples tested in air show no crazes on the outer surfaces (Figure 4.1.10a), whereas the PC/D4-SiO_2 composites filled with 2-, 6- and 8 Vol.-% of nanoparticles tested in IPA show obvious crazes or micro-cracks which direction is perpendicular to the sample length as shown in Figure 4.1.10b. In addition, the number of such crazes increases clearly with increasing particle content due to increasing number of nanoparticles/agglomerates in PC composites which lead to increasing stiffness of composites. Figure 4.1.10c shows the side view of crazes in some samples. Interestingly, the composite filled with 4 Vol.-% of D4-SiO_2 nanoparticles shows a different behaviour on the outer surface, namely intensive plastic deformation instead of crazes. This result is in good agreement with the results of other mechanical tests in which the composite containing 4 Vol.-% of nanoparticles shows the highest tensile strength and fracture toughness K_{IC} as well as resistance to ESC. A potential explanation is that at 4 Vol.-% of nanoparticles, a balance between stiffening and toughening effects of nanoparticles is achieved in comparison to lower or higher particle contents.

Unlike PC/D4-SiO_2 composites, neat PC shows no crazes or plastic deformation after test in IPA. This result indicates that the incorporation of D4-SiO_2 nanoparticles into PC promotes the craze initiation in IPA due to particle debonding from the matrix. The particle debonding occurs slowly with difficulty in air, but this process is accelerated in

IPA through solvent diffusion and swelling. Under constant strain, the micro voids formed by particle debonding could quickly coalesce and further propagate to large macro crazes as shown in pictures.

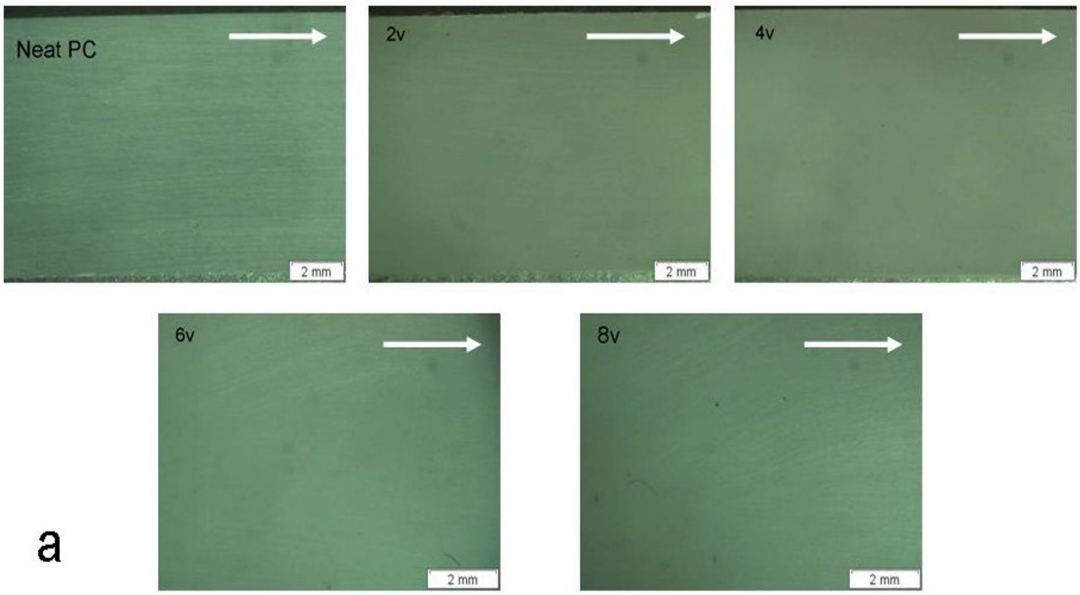

Figure 4.1.10(a): Optical micrographs of bent strip samples tested in air: no crazes and/or cracks on the surfaces of all samples. The white arrows show the bending direction of samples.

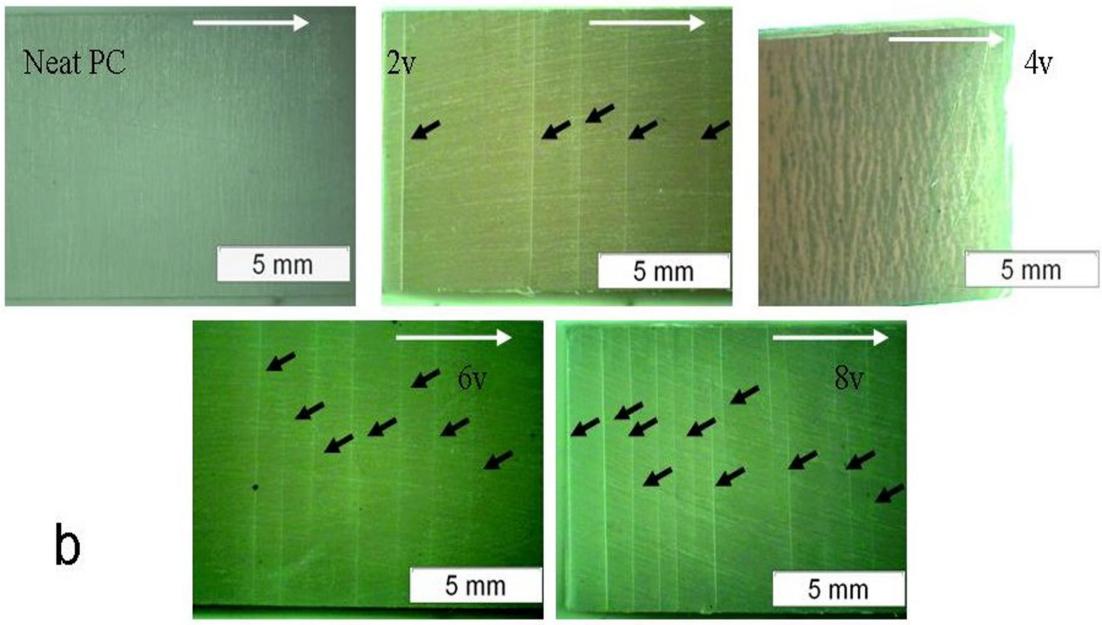

Figure 4.1.10(b): Optical micrographs of bent strip samples tested in IPA: crazes and/or plastic deformation on the surfaces of PC composites. The long arrows show the bending direction of samples. The short arrows indicate the crazes.

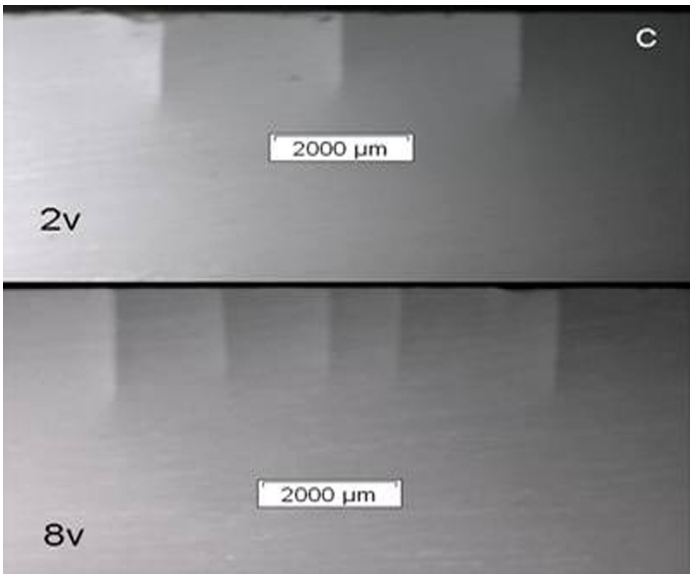

Figure 4.1.10(c): Optical micrographs of bent strip samples tested in IPA: a side view indicating the depth of crazes in samples.

4.1.5 Optical properties

Transparency is an important behaviour of PC. The optical properties, combined with the material toughness, strength and resistance to ultraviolet light, make PC an alternative material toward glass in many applications [6]. Figure 4.1.11a shows the results of optical characterization of PC composites. As expected, the light transmittance of PC/D4-SiO_2 composites decreases with increasing nanoparticle content due to increasing light reflection at the interfaces between PC matrix and D4-SiO_2 particles. Since the refractive indices of PC (1.58) and D4-SiO_2 particles (1.45) are not well-matching, loss in transparency due to reflection in PC/D4-SiO_2 composites can not be avoided. Unlike decreased light transmittance, the haze value clearly increases with increasing particle content. According to [122], the main reason for increasing haze in composites is the Rayleigh light scattering which is caused by dispersed nanoparticles and increased with increasing particle content. Another reason for decreased light transmittance and increased haze of composites is the decomposition of PC matrix during compounding process due to hydrolysis of carbonate groups [44, 45]. Figure 4.1.11b shows that the untreated PC exhibits clearly a higher thermal stability than extruded PC. Accordingly, the presence of degradation products in PC composites should be partly responsible for a decrease in transparency. According to the experience in this study and literatures [44, 45], the degradation of bisphenol-A PC during extrusion process can not be avoided, regardless of which parameters are used for extrusion and injection moulding (temperature, screw configuration, screw speed, etc.).

As shown in Figure 4.1.11a, the clarity of PC/D4-SiO_2 composites does not change much compared to neat PC as particle content increases. Figure 4.1.12 shows the

neat PC and PC composite samples for visual assessment. It is evident that the PC/SiO_2 composites show yellowish discoloration after particle compounding. Increasing particle content leads to decreased transparency of samples.

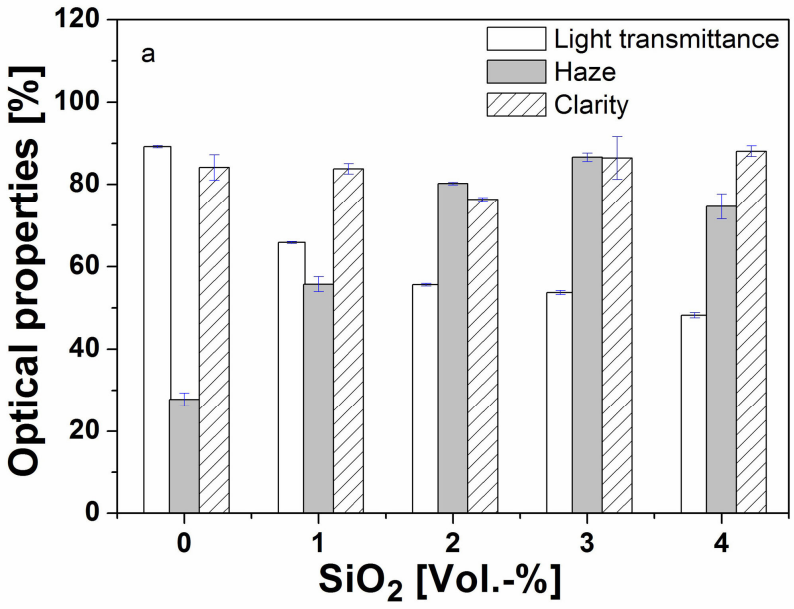

Figure 4.1.11(a): Results of optical tests of PC samples: light transmittance, haze and clarity as a function of particle content.

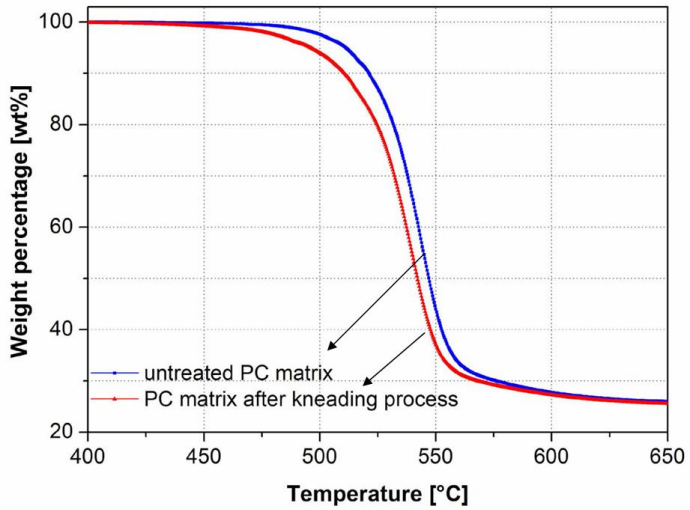

Figure 4.1.11(b): TGA results of neat PC as received and PC after extrusion process.

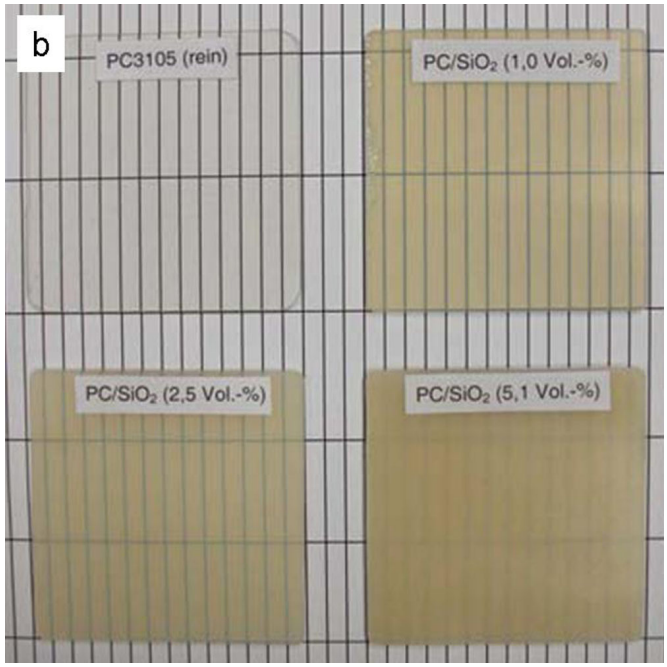

Figure 4.1.12: Neat PC and PC/D4-SiO_2 composites for visual assessment.

4.1.6 Conclusion

Surface-modified nanosilica-filled PC composites were produced using direct melt compounding method. The thermal, mechanical and optical properties of PC/D4-SiO_2 nanocomposites were characterized. According to the results obtained, the following conclusions can be drawn:

1. The thermal stability of PC/D4-SiO_2 nanocomposites will be -based on TGA analysis- clearly improved compared to neat PC and it increases with increasing particle content.
2. The stiffening effect of D4-SiO_2 nanoparticles in PC matrix is evident, indicated by an overall increased storage modulus and tensile modulus. The reinforcing and toughening effects are observed at particle content lower that 4 Vol.-%,

indicated by increased tensile strength and fracture toughness of respective PC composites.

3. The resistance against environmental stress cracking of PC/SiO_2 composites containing up to 8 Vol.-% of particles in toluene is significantly improved compared to neat PC. The maximum improvement is by 118% at 4 Vol.-% of particles.
4. The PC/D4-SiO_2 composite containing 4 Vol.-% of nanoparticles exhibits the best mechanical properties such as the highest tensile strength, the highest fracture toughness, and the highest ESC resistance in toluene among produced PC/D4-SiO_2 nanocomposites.
5. The PC composites show yellowish discoloration after extrusion and injection moulding process. The light transmittance and haze of PC/D4-SiO_2 composites are deteriorated with increasing particle content due to increased light reflection and scattering in composites (not optimal matched refractive indices), whereas the clarity of PC composites is comparable high to that one of neat PC.

4.2 iPP/SiO_2 Composites filled with different SiO_2 nanoparticles

In this chapter, the mechanical and thermal properties of different SiO_2-filled iPP composites are studied and discussed. In addition, the interface behaviour between iPP matrix and SiO_2 nanoparticles is also investigated and discussed.

4.2.1 Degrees of hydrophobicity and surface covering of SiO_2 nanoparticles

The unmodified polar C0-SiO_2, modified 3C1-, C8- und C16-SiO_2 nanoparticles which are used for iPP have comparable primary particle sizes, but they show different surface polarity in terms of hydrophobicity by using different surface pre-treatment. In order to obtain the influence of surface polarity of respective nanoparticles on thermal and mechanical properties of iPP/SiO_2 nanocomposites, the hydrophobicity of respective SiO_2 nanoparticles should be determined firstly.

The hydrophobicity measurements show that the 3C1-SiO_2 reveals the highest degree of hydrophobicity by 63.5%. The C8-nanoparticles show a lower degree of hydrophobicity than 3C1-nanoparticles by 56.2%. Both nanoparticles could not be wetted in water without methanol addition. Unexpected, the surface modified C16-SiO_2 nanoparticles were totally wetted in pure water forming a clear emulsion like unmodified polar C0-SiO_2 nanoparticles as shown in Figure 4.2.1. This result indicates a very low degree of organic modification of C16-SiO_2 nanoparticles. Note that the carbon content in the C16-SiO_2 nanoparticles is only 0.9~1.8 wt% according to supplier's information. The carbon contents in 3C1-SiO_2 and C8-SiO_2 nanoparticles are clearly higher than this value (Table 3.1).

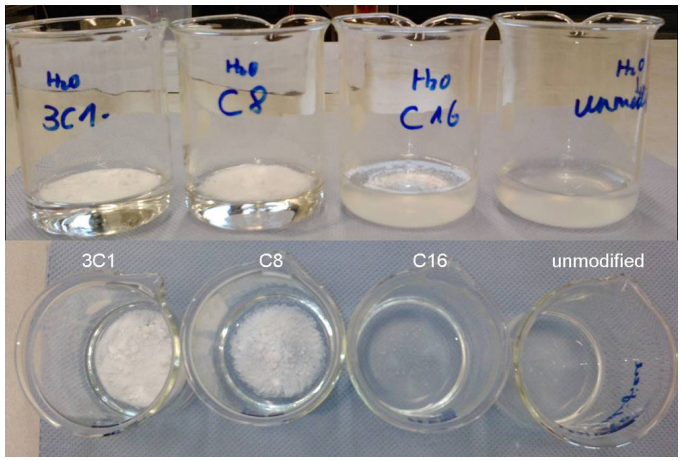

Figure 4.2.1: Different water-wettability of various unmodified and surface modified SiO_2 nanoparticles.

This result should be attributed to different degrees of surface covering of used silica nanoparticles by the alkyl chains on the particle surface. Based on carbon content in respective silica nanoparticles given in Table 3.1 and the alkyl chain length, it can be qualitatively obtained that the degree of surface covering of respective silica nanoparticles decreases with the following order: 3C1-SiO_2 > C8-SiO_2 > C16-SiO_2 > C0-SiO_2 (unmodified, hydrophilic surface: Si-OH). The higher the degree of surface covering of SiO_2 nanoparticles, the higher is the degree of hydrophobicity of these nanoparticles. Because iPP is an unpolar polymer, the SiO_2 nanoparticles with higher degree of hydrophobicity should be better dispersed in iPP due to better compatibility with hydrophobic matrix.

According to literature [123], a globular Aerosil SiO_2 particle with a diameter of 7 nm and densely packed oxygen atoms contains 10^5 oxygen atoms. This corresponds to a formula of $Si_{50000}O_{100000}$ in molecular language. It is accepted in this study that the number of SiO_2 molecules in a primary particle is proportional to the particle diameter. This means, the molecular formula of one 3C1-SiO_2 nanoparticle used in this study

with a diameter of 12 nm can be described as $Si_{\frac{12\cdot 50000}{7}} O_{\frac{12\cdot 100000}{7}}$. Accordingly, the molecular weight of such a SiO_2 nanoparticle can be calculated as:

*28*12*50000/7 g/mol + 16*12*10^5/7 g/mol = 5.1 *10^6 g/mol*

The surface area of this spherical nanoparticle can be calculated as:

$$A = \pi d^2 = \pi \cdot (12nm)^2$$

The molecular weight of a $(CH_3)_3$-Si-O-group:

36 (3C) + 28 (Si) + 16 (O) + 9 (9H) = 89 g/mol

The weight of C-atoms in a $(CH_3)_3$-Si-O-group:

*3*12 = 36 g/mol*

According to supplier's information (technical data from Evonik), the C-weight percentage in the 3C1-SiO_2 nanoparticle is by 2-4 wt%. The average value by 3 wt% is taken in this case. Then the number of $(CH_3)_3$-Si-O-groups (n) on a primary particle surface can be obtained as:

$$\frac{36 \cdot n}{5.1 \cdot 10^6 + 89 \cdot n} = 3wt\%$$

It leads to: *n* = 4590

As a simplified model, the cover surface of a single trimethylsilyl group on the nanoparticle surface can be treated as an equilateral triangle formed by three C-atoms as shown in Figure 4.2.2.

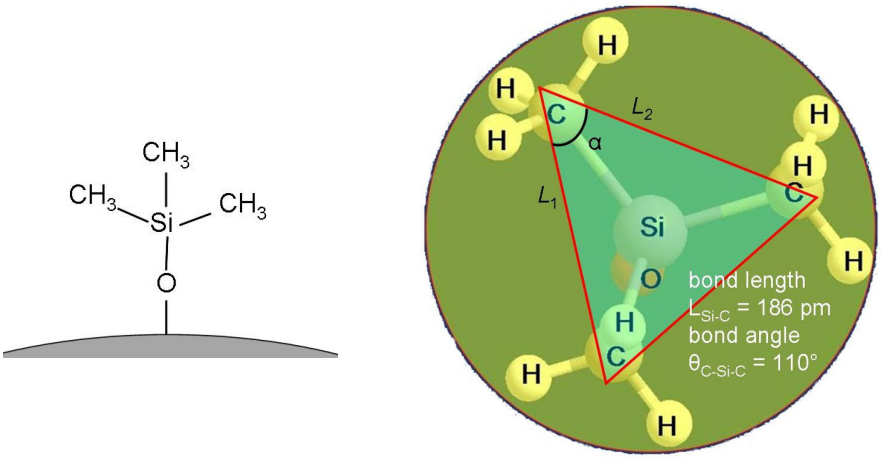

Figure 4.2.2: Schematic illustration of a $(CH_3)_3$-Si-O-group on the 3C1-SiO_2 nanoparticle surface.

As known in literatures [124, 125], the bond length between Si and C atoms (L_{Si-C}) in trimethylsilyl group is 186 pm. The bond angle θ_{C-Si-C} is about 110°. Accordingly, the length between two C-atoms L_{C-C} in the approximate equilateral triangle composed of three C-atoms can be calculated according to the following equation:

$$c^2 = a^2 + b^2 - 2a \cdot b \cos\theta$$

where c is the length of equilateral triangle L_{C-C}, a and b are bond lengths between Si and C atoms (a = b = 186 pm), θ is the C-Si-C bond angle with a value of 110°. It can be obtained: c = 305 pm.

The surface of this equilateral triangle can be obtained as follows:

$$F = \frac{1}{2} L_1 L_2 \sin\alpha$$

where L_1 and L_2 are the lengths of this equilateral triangle ($L_1 = L_2 = 305$ pm), α is the angle between L_1 and L_2 as shown in Figure 4.2.2 ($\alpha = 60°$ in equilateral triangle). Therefore, the surface *F* can be calculated as *F* = 40281 pm^2.

The theoretical maximum number (N) of these equilateral triangles covering on this 3C1-SiO_2-nanoparticle surface can be approximately obtained as:

$$N = \frac{nanoparticle - surface}{triangle - surface} = \frac{A}{F} = \frac{\pi \cdot (12nm)^2}{40281pm^2} = 11225$$

As calculated above, the real number of trimethylsilyl groups resulting in 3 wt% of C-element on the 3C1-SiO_2 nanoparticle surface is 4590. Therefore, the degree of covering (*S)* of the 3C1-SiO_2 nanoparticle surface is:

$$S = \frac{n}{N} \cdot 100\% = \frac{4590}{11225} \cdot 100\% = 41\%$$

It is ever reported that only less than 50% of OH-groups on such a silica surface are reactive and can be replaced via surface modification. The other OH-substrates have fewer opportunities for reaction [126]. Therefore, the calculation of degree of surface covering in this study is reliable.

The degree of surface covering by 41% means that nearly half of the particle surface is covered by organic groups which could build up an organic shell surrounding the 3C1-SiO_2 nanoparticle as shown in Figure 4.2.3a. As a result, these nanoparticles exhibit a high degree of hydrophobicity by 63.5%. Compared to short 3C1-groups, the long C8- and C16-chains behave very differently regarding spacial location and stretching direction. Therefore, the simplified model is not suitable to calculate the surface covering of C8- and C16-SiO_2 particles. In general, the higher the degree of covering on the nanoparticle surface covered by organic groups, the higher is the degree of hydrophobicity of such nanoparticles. Compared to 3C1-SiO_2 nanoparticles, the C8-SiO_2 nanoparticles show a lower degree of hydrophobicity by 56.2%. This corresponds to a lower degree of covering on particle surface. The C16-SiO_2

nanoparticles show toll hydrophilic surface nature like unmodified C0-SiO_2 particles, indicating a very poor covering of particle surface as shown in Figure 4.2.3b.

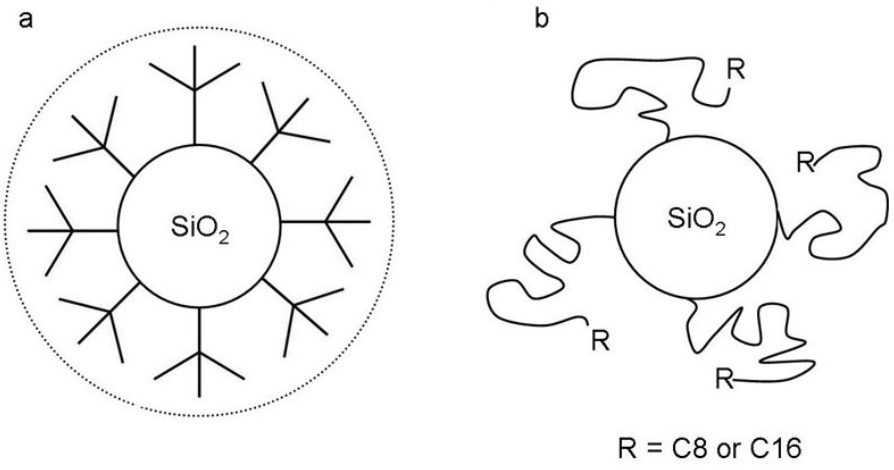

Figure 4.2.3: Schematic Illustration of surface behaviour of different SiO_2 nanoparticles regarding surface covering: (a) 3C1-SiO_2 nanoparticles, and (b) C8- and C16-SiO_2 nanoparticles.

4.2.2 Dispersion of SiO_2 nanoparticles in iPP matrix

Figure 4.2.4 shows SEM micrographs of respective iPP/SiO_2 nanocomposites. It can be seen that the 3C1- and C8-SiO_2 nanoparticles are more homogeneously distributed in iPP matrix than C0- and C16-SiO_2 nanoparticles. The latter two particles result in more and larger particle clusters/agglomerates than the former two types. This result correlates well with the degrees of hydrophobicity and surface covering of respective nanoparticles.

It is well known that the hydroxyl groups on particle surface can build up hydrogen bonds among particles themselves (interbonding), leading to a higher degree of agglomeration. This is the reason for stronger agglomeration of C0-SiO_2 particles.

After surface modification with silanes, the introduced alkyl chains on particle surface can in some degree prevent the forming of hydrogen bonds due to steric hindrance, increasing the dispersibility of nanoparticles. However, Bagwe et al. [127] concluded that the silica nanoparticles with long alkyl chains on the particle surface have a much smaller shear or slippage plane, and the long alkyl chains extending from the particle surface are beyond the shear plane. Therefore, such nanoparticles can easily agglomerate due to strong hydrophobic interactions among nanoparticles themselves. This suggestion explain the higher degree of agglomeration of C16-SiO_2 nanoparticles in this study. On the other hand, the very low degree of hydrophobicity of C16-SiO_2 nanoparticles should be the main reason for the stronger agglomeration.

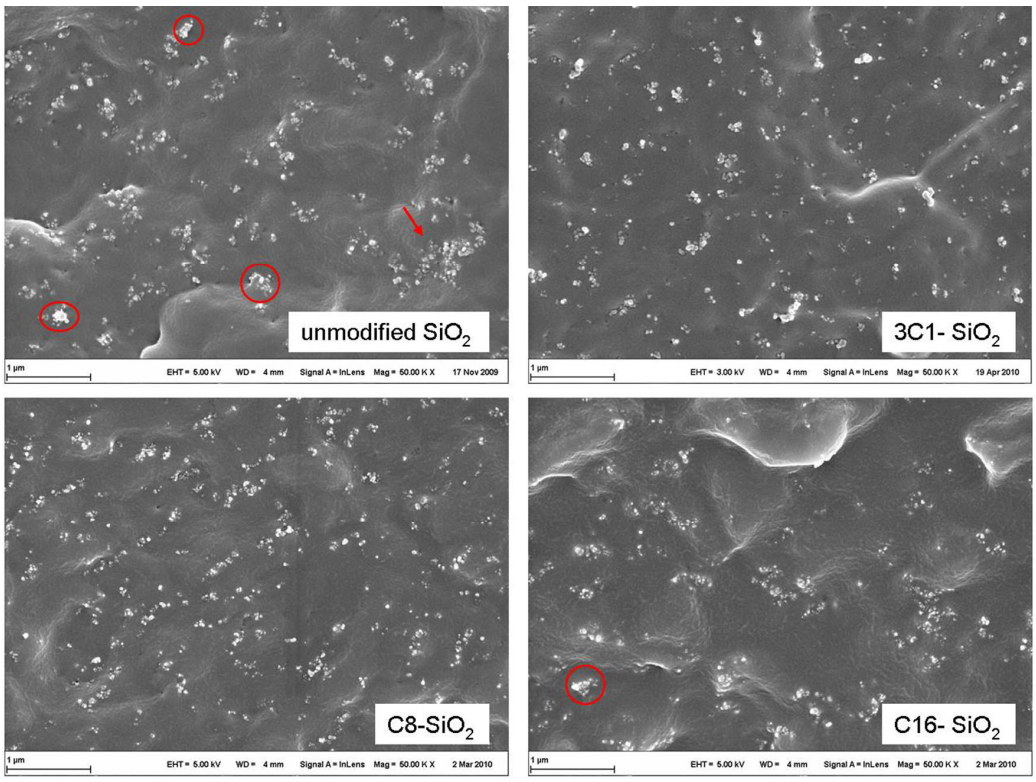

Figure 4.2.4: SEM micrographs of iPP/SiO_2 nanocomposites filled with 2.3 Vol.-% of different treated silica nanoparticles.

4.2.3 Mechanical properties

Tensile properties

The typical stress-strain curves (S-S curve) of tensile tests for all iPP/SiO_2 composites containing 2.3 Vol.% of nanoparticles are shown in Figure 4.2.5. From the S-S-curves, the incorporation of all SiO_2 nanoparticles clearly reinforces the iPP matrix but reduces the ductility of polymer matrix.

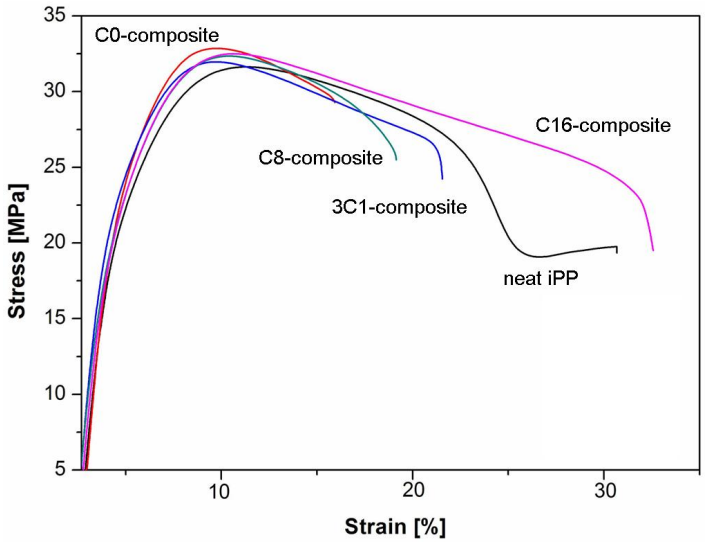

Figure 4.2.5: Stress-strain curves of neat iPP and iPP/SiO_2 composites containing 2.3 Vol.-% of nanoparticles obtained by tensile tests.

The relative improvements in tensile modulus, tensile strength and tensile strain of iPP/SiO_2 nanocomposites compared to neat iPP are presented together in Figure 4.2.6a as a function of alkyl chain length. One can see that the incorporation of all types of nanoparticles significantly increases the material stiffness indicated by overall increased tensile modulus. Since the crystallinity of iPP matrix in iPP/SiO_2 composites are slightly decreased compared to neat iPP, the increase in tensile modulus should be attributed to the rigid particles themselves. The maximum improvement in tensile

modulus is by 21% achieved by C0-iPP/SiO_2 composite. Increasing alkyl chain length leads to clearly decreased tensile modulus. It is reported that the interphase between iPP and silane-modified SiO_2 nanoparticles shows viscoelastic behaviour. The alkyl chains in particle-matrix interphase can act as plasticizers reducing the stiffness of boundary layer, and this effect increases with increasing chain length [27, 131].

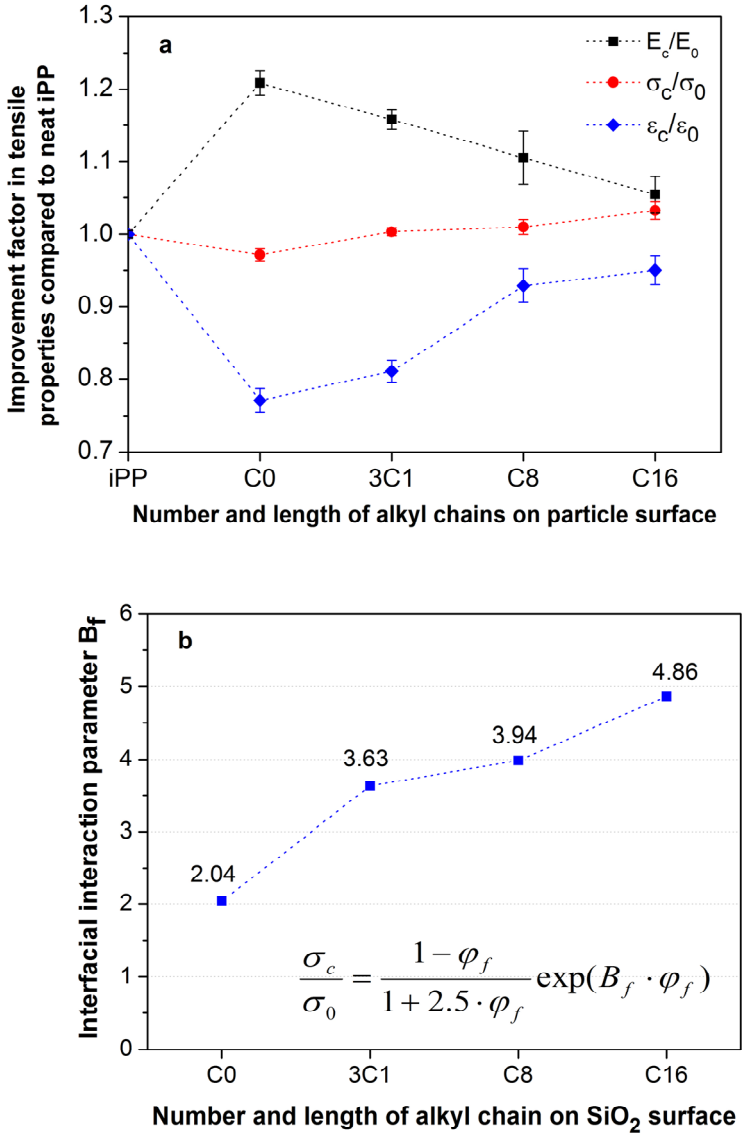

Figure 4.2.6: (a) Relative improvements in tensile modulus, tensile strength and strain of iPP/SiO_2 composites (2.3 Vol.-%) compared to neat iPP as a function of alkyl chain length, (b) interfacial interaction parameter B_f as a function of alkyl chain length.

Unlike tensile modulus, the tensile strength and strain increase slightly with increasing alkyl chain length. Generally, the tensile strength mainly depends on the interfacial interactions between polymer matrix and fillers. In C0-composite, the interfacial adhesion is very weak due to hydrophilic-hydrophobic repulsion force. Therefore, the tensile strength of this composite is decreased compared to neat iPP. The introduction of alkyl chains on particle surface increases the hydrophobicity of respective nanoparticles and leads to increased interfacial interactions between iPP matrix and SiO_2 particles due to chain entanglement at interface. As a result, the tensile strength also increases. The 3C1-composite exhibits comparable tensile strength as neat iPP because the degree of chain entanglement at matrix-particle interface is very low due to short methyl groups. Increasing alkyl chain length on particle surface leads to an increased degree of chain entanglement at interface. Therefore, the tensile strength of iPP/SiO_2 composites also increases with increasing chain length, which is in agreement with the calculated interfacial interaction parameter B_f based on Pukanszky's model as shown in Figure 4.2.6b. For tensile strain, the dominated influence factor is usually the interfacial slippage. At a certain degree of plastic deformation, the interfacial slippage between particle surface and polymer matrix leads to debonding of particles. With increasing alkyl chain length the interfacial slippage becomes more difficult due to increased interfacial interactions, and the plasticizing effect of nanoparticles also increases [27, 131], resulting in higher tensile strain.

It should be noted that the interfacial interaction in iPP/SiO_2 composites in this study is weak Van der Waals force and the alkyl chains (C1, C8 and C16) are not long enough to achieve a high degree of chain entanglement. Therefore, the improvements in tensile strength of iPP/SiO_2 nanocomposites are not significant. Compared with iPP/SiO_2 nanocomposites in this study, the iPP/SiO_2 nanocomposites filled with

polymer-grafted (PS, PMMA, etc.) SiO_2 nanoparticles show much higher tensile strength and B_f values [132]. This is also an evidence of increased interfacial interactions with increased chain length in boundary layer.

Fracture toughness, fracture mechanisms and morphology

The fracture toughness of iPP/SiO_2 composites were determined by using compact tension test. Figure 4.2.7a shows the force-displacement curves of all iPP samples. It is evident that the incorporation of C8-, C16- and C0-SiO_2 nanoparticles leads to decreased load maximum (F_{max}) at which the initial crack starts to propagate, whereas the 3C1-iPP/SiO_2 nanocomposite shows obviously increased F_{max} compared to neat iPP. Correspondingly, the fracture toughness K_{IC} calculated from F_{max} decreases with the following order: 3C1-iPP/SiO_2 > neat iPP > C0-iPP/SiO_2 > C8-iPP/SiO_2 > C16-iPP/SiO_2 as shown in Figure 4.2.7b. The improvement in fracture toughness of 3C1-iPP/SiO_2 composite is by 9%.

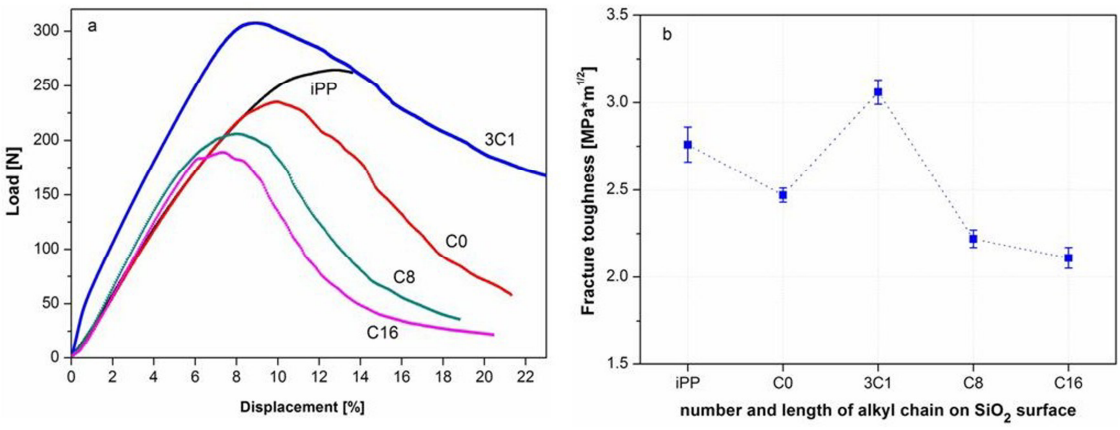

Figure 4.2.7: (a) Load-displacement curves of neat iPP and iPP/SiO_2 composites (2.3 Vol.-%), (b) fracture toughness K_{IC} of neat iPP and iPP/SiO_2 composites (2.3 Vol.-%) as a function of alkyl chain length.

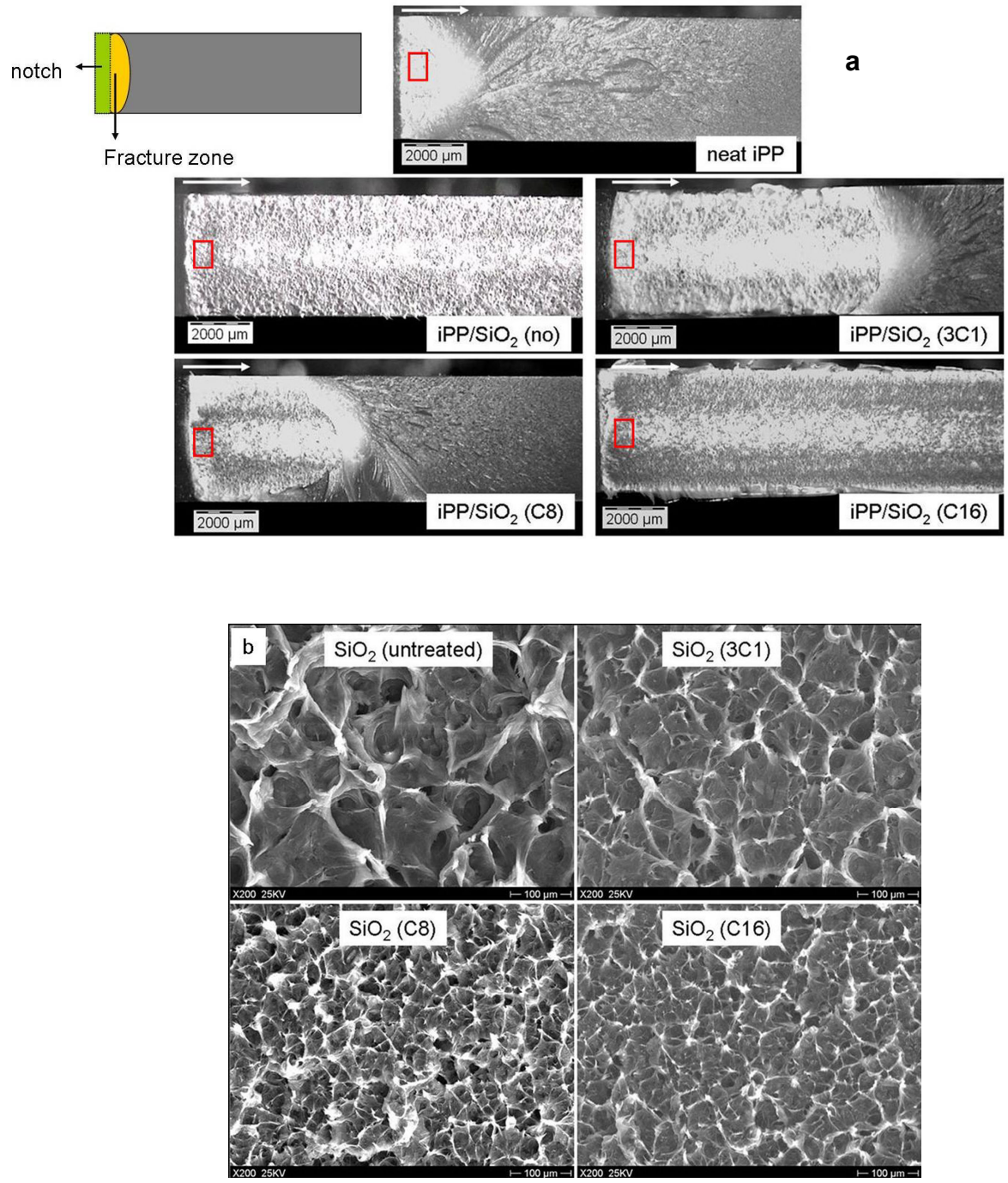

Figure 4.2.8: SEM micrographs of fractured iPP and iPP composites (2.3 Vol.-%): (a) overview of fracture surfaces, (b) close-view of the fracture zones. The arrows in 4.2.8a indicate the direction of crack propagation. The squares ahead of the pre-cracks indicate the positions where the fracture surfaces in 4.2.8b are taken.

As introduced in chapter 1.2.4, the micro mechanism regarding the respective deformation mechanisms and particle debonding is widely accepted to explain the fracture mechanism in nanoparticle-filled polymer composites. In iPP/nanoparticle composites, it is also reported that debonding is believed to be the initial damage mechanism because of the low polarity and consequently low surface free energy of iPP matrix [133, 134]. Figure 4.2.8a shows the fractured surface morphology near the crack tip of neat iPP and iPP/SiO_2 composites (2.3 Vol.-%) after CT-test.

Macroscopically, neat iPP, C8-composite and 3C1-composite show similar fracture surfaces with increased fracture zone in which matrix deformation is observed. Differently, C16-composite and C0-composite show longer fracture zones with less matrix deformation on the surfaces, particularly the fracture surface of C16-composite is very smooth. Macroscopically, one can get the impression that the fracture behaviour of iPP/SiO_2 composites correlates well with the degree of hydrophobicity of respective SiO_2 nanoparticles, i.e. the degree of surface covering. The 3C1- and C8-SiO_2 nanoparticles show higher hydrophobicity than C0-SiO_2 and C16-SiO_2 nanoparticles (chapter 4.2.1), correspondingly, 3C1-composite and C8-composite show stronger resistance against crack growth.

A close examination of the fracture zones near the initial crack tip is presented in Figure 4.2.8b. It can be seen that all composites exhibit micro deformation and numerous dimples (particle debonding) on the fracture surfaces. The C0-iPP/SiO_2 composite shows the most extensive micro deformation but the lowest number of dimples. With increasing alkyl chain length, the plastic deformation of matrix decreases clearly whereas the number of dimples increases. This increase of dimple number can be attributed to increased stress concentration effect of nanoparticles due to increased interfacial interactions. In C0-iPP/SiO_2 composite, the nanoparticles and agglomerates detach easily from iPP matrix because of poor matrix-particle adhesion,

forming less but larger voids. On one hand, it is believed that the formation of more dimples in fracture process is accompanied by more energy dissipation, leading to higher fracture toughness [119, 120]. On the other hand, more voids (dimples) result in smaller matrix zone on the fracture surface. Consequently, the degree of micro deformation of matrix is reduced by coalescence of voids during fracture process. This leads finally to easier crack propagation and ductile-brittle transition. Obviously, the obtained fracture toughness of iPP/SiO_2 nanocomposites is a result of combined effects. The 3C1-iPP/SiO_2 composite exhibits improved fracture toughness compared to neat iPP because the total energy dissipation during fracture process in this composite is larger than that one in neat iPP. Conversely, the other composites dissipate lower total energy during deformation process and formation of dimples than neat iPP, therefore, they show a decreased fracture toughness compared to neat iPP.

Notched Charpy impact strength

Besides tensile properties and fracture toughness, the notched Charpy impact strength was also measured. Figure 4.2.9 shows the results of Charpy impact test for all iPP samples. The C0-iPP/SiO_2 composite shows slightly increased impact strength with an improvement by 4.9% in comparison to neat iPP. In analogy to CT results, the 3C1-iPP/SiO_2 composite reveals the highest impact strength among iPP/SiO_2 composites containing surface modified nanoparticles with a significant improvement by 45.6%. The C8-composite exhibits increased impact strength with an improvement by 7.3%, whereas the C16-composite shows a decreased notched Charpy impact strength with a reduction by 5.8% compared to neat iPP. Similar to fracture toughness K_{IC}, this result correlates well with the degree of hydrophobicity/surface covering of respective modified nanoparticles.

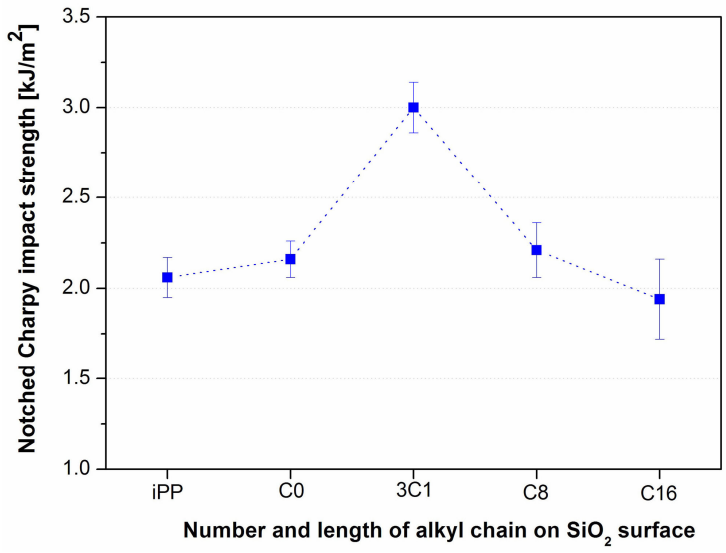

Figure 4.2.9: Result of notched Charpy impact tests of neat iPP and iPP/SiO_2 composites (2.3 Vol.-%).

4.2.4 Thermal and thermo-mechanical properties

TGA results

In order to study the thermal behaviour of respective iPP/SiO_2 composites, TGA measurements were performed. Figure 4.2.10 shows the decomposition curves of all iPP samples. It is noted that the weight loss of pure iPP and its composites below 350 °C is lower than 0.05% corresponding to loss of remaining humidity in materials. The main decomposition of iPP matrix corresponding to molecular back-bone (C-C bond) degradation starts at about 360 °C with an accelerated rate. The onset thermal degradation temperature (T_{onset}), characterizing the thermal stability of a material, is 443.7 °C for neat iPP. The incorporation of SiO_2 nanoparticles obviously increases the thermal stability of iPP, indicated by increased T_{onset} with a maximum improvement by 11.3 °C achieved by C16-iPP/SiO_2 composite. Compared to C0-iPP/SiO_2 composite, the iPP/SiO_2 composites filled with surface modified nanoparticles show higher T_{onset}

values. This result correlates well with the interfacial interaction parameter B_f calculated before as shown in Figure 4.2.6b and Table 4.3. Between 3C1- and C8-iPP/SiO_2 composites, the difference in thermal stability T_{onset} is small due to small difference in their B_f values (3.63 vs. 3.99).

The temperatures of 20% and 50% weight losses as well as the T_{onset} of all samples are summarized in Table 4.3. It can be seen that the values obtained by all composites are clearly higher than those of neat iPP except for $T_{20\%}$ of C0-iPP/SiO_2 composite. All composites containing 2.3 Vol.-% of nanoparticles exhibit similar residue weight fraction at 525 °C by about 5 wt%, corresponding to 2.3 Vol.-% of SiO_2 nanoparticles, as expected.

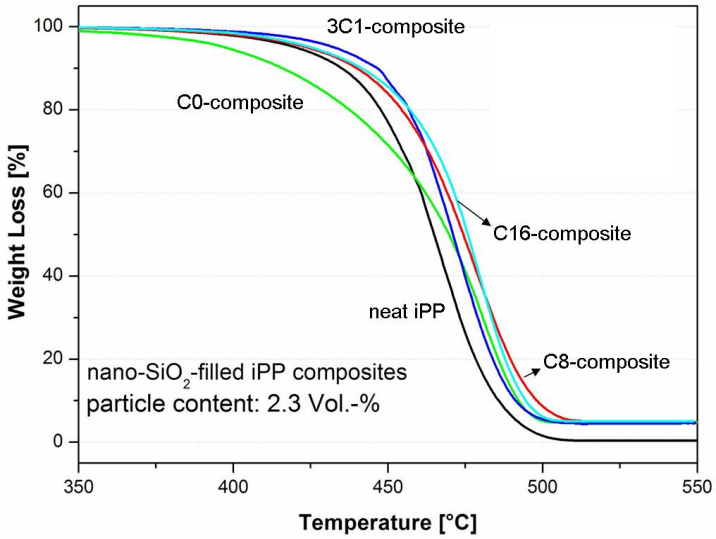

Figure 4.2.10: Weight loss as a function of temperature for neat iPP and iPP/SiO_2 composites containing 2.3 Vol.-% of particles obtained by TGA.

Table 4.3: TGA results of neat iPP and iPP/SiO_2 composites containing 2.3 Vol.-% of nanoparticles

Samples	Interfacial interaction parameter B_f	T_{onset} [°C]	$T_{20\%}$ [°C]	$T_{50\%}$ [°C]
neat iPP		443.7	447.6	464.9
C0-iPP/SiO_2	2.04	449.1	437.5	469.6
3C1-iPP/SiO_2	3.63	452.6	456.6	470.7
C8-iPP/SiO_2	3.99	452.2	454.4	474.3
C16-iPP/SiO_2	4.86	455.0	456.8	475.7

DSC results

The effect of surface-treated and untreated SiO_2 nanoparticles on crystallization behaviour of iPP was determined by DSC measurements. The important data obtained are listed in Table 4.4. From the results, the melting temperature T_m of all iPP samples is nearly identical. The addition of C0-SiO_2 nanoparticles shows almost no effect on the crystallinity of iPP although the crystallization process starts at a little higher temperature. The crystallinity of iPP in 3C1-, C8- and C16-SiO_2 filled composites is decreased up to 1.9%, which could be the effect of chain entanglements in interphase restricting the crystallization of iPP molecules. The crystalline temperature of iPP in 3C1-, C8- and C16-composites shifts slightly to a higher temperature with a maximum improvement by 1.1 °C. Based on these results, one can conclude that the crystalline behaviour of iPP will not be greatly influenced by addition of both treated and untreated SiO_2 nanoparticles. This DSC results are in good agreement with literature [128], where Rong and his co-workers reported that the crystallinity and thermal temperatures (T_m, T_c etc.) of PP are not significantly affected by addition of untreated and PS-grafted-SiO_2 nanoparticles.

Table 4.4: DSC results of iPP and iPP/SiO_2 composites containing 2.3 Vol.-% of nanoparticles

Samples	Melt temperature T_m [°C]	Crystalline enthalpy ΔH_m [J/g]	Crystallinity X_c [%]	Crystalline temperature T_c [°C]
neat iPP	168.4	101.2	48.4	116.0
C0-iPP/SiO_2	167.0	101.0	48.3	116.9
3C1-iPP/SiO_2	168.2	98.0	46.9	116.2
C8-iPP/SiO_2	167.7	97.2	46.5	116.6
C16-iPP/SiO_2	167.3	97.6	46.7	117.1

From the SEM micrographs in Figure 4.2.11, it can be seen that neat iPP shows typical three-dimensional spherulite structure with clear boundaries. The iPP spherulites are 10-20 µm in diameter. Conversely, no spherulitic structure is observed in all iPP/SiO_2 composites. The reason for disappeared spherulites in iPP/SiO_2 composites could be the presence of nanoparticles which prevented the growth of matrix crystals due to small interparticle distances [128].

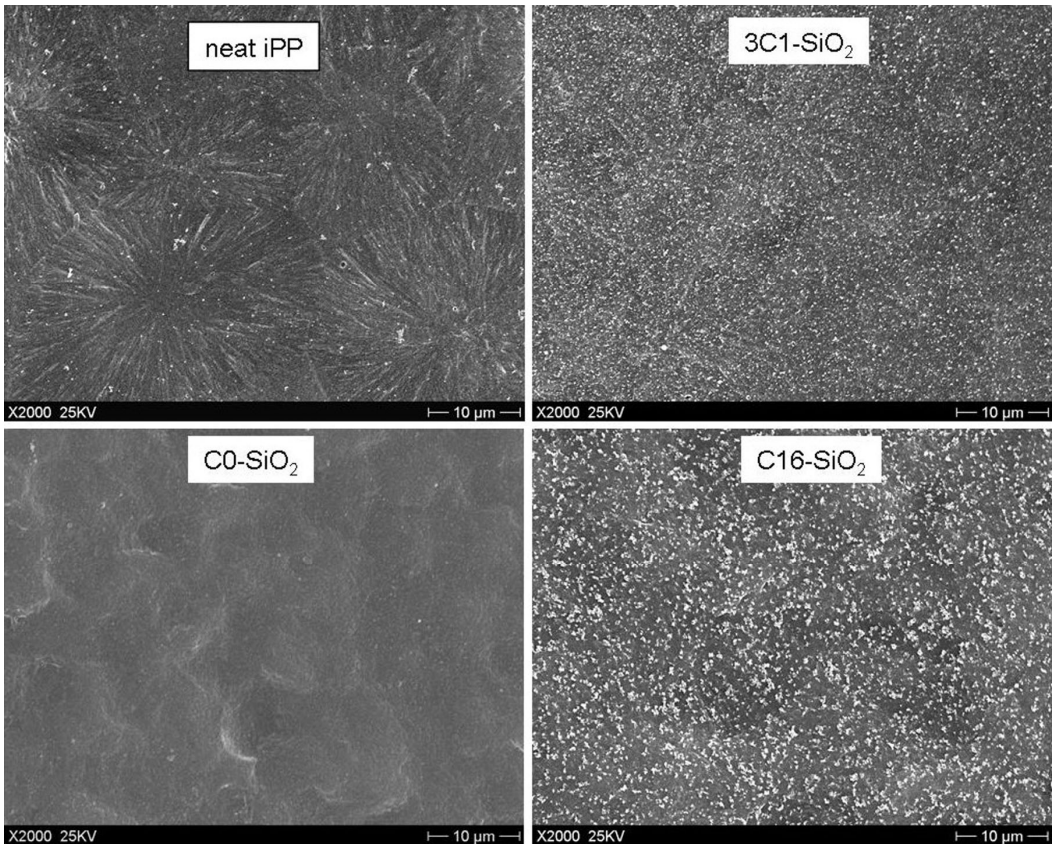

Figure 4.2.11: Spherulite structure and size of neat iPP and iPP in iPP/SiO_2 composites containing 2.3 Vol.-% of nanoparticles examined by SEM.

DMTA results and interphase behaviour

The dynamic-mechanical thermal properties of iPP/SiO_2 composites were determined by using DMTA. Due to the fact that the mechanical loss factor tanδ is a sensitive indicator of molecular motions and phase transition, the curves of tanδ against temperature are shown in Figure 4.2.12. It is observed that the tanδ curves of all samples exhibit two relaxation peaks within selected temperature range. The first peak around 12°C corresponds to the glass transition of amorphous iPP (β-relaxation). Evidently, the 3C1-iPP/SiO_2 composite shows the highest intensity of β-transition peak among all samples, shifting clearly to higher temperature compared to neat iPP.

The C8-iPP/SiO_2 and C16-iPP/SiO_2 composites show comparable β-peak intensity as neat iPP, whereas the C0-composite shows clearly decreased β-peak intensity compared to iPP matrix. This result can be firstly related to different dispersion quality of respective SiO_2 nanoparticles in matrix; secondly, this should be related to increased interfacial interactions between iPP matrix and silane-treated SiO_2 nanoparticles.

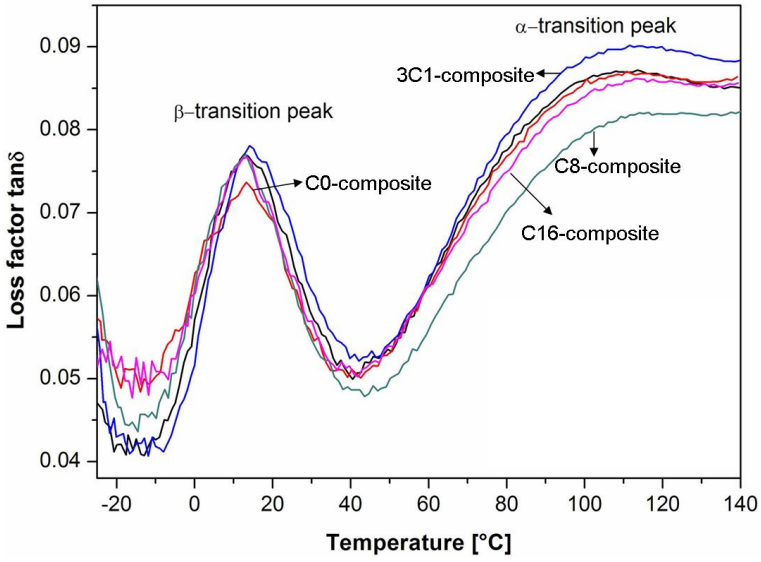

Figure 4.2.12: DMTA results of neat iPP and its composites filled with 2.3 Vol.-% of different SiO_2 nanoparticles.

The second transition peak around 110 °C in tanδ curve is attributed to α-transition of crystalline iPP due to crystal-crystal slippage motion [129]. The broadness of this peak may indicate a distribution of lamellar thickness of iPP crystals. The storage- and loss modulus at 23 °C, and the β-transition temperature T_β of all samples are summarized in Table 4.5. It can be seen that the incorporation of all silica nanoparticles significantly improves the storage- and loss modulus of iPP. The β-transition temperatures of iPP/SiO_2 composites are slightly increased up to 2.5 °C compared to neat iPP. The 3C1-iPP/SiO_2 composite shows the highest modulus and T_β values among the

samples. The reason should be the higher hydrophobicity and subsequent better dispersion quality of 3C1-particles.

Table 4.5: DMTA results and interphase parameters obtained based on Sumita's model [106] for neat iPP and iPP/SiO_2 composites containing 2.3 Vol.-% of nanoparticles

Composites	φ_f [Vol.-%]	$E'_{23°C}$ [MPa]	$E''_{23°C}$ [MPa]	T_β [°C]	φ_e [Vol.-%]	Δr [nm]
neat iPP	--	1762 ± 131	128.4 ± 1.5	12.4	--	--
C0-iPP/SiO_2	2.27	2150 ± 122	139.3 ± 1.7	12.8	7.96	3.93
3C1-iPP/SiO_2	2.24	2214 ± 71	147.2 ± 1.9	14.9	12.53	5.25
C8-iPP/SiO_2	2.26	1955 ± 78	137.5 ± 3.9	13.3	7.07	2.46
C16-iPP/SiO_2	2.26	2051 ± 61	136.7 ± 2.0	13.3	5.51	2.03

Based on Sumita's model introduced in chapter 1.2.4, the effective volume fraction of nanoparticles and the interphase thickness in respective nanocomposites can be quantitatively characterized as shown in Table 4.5. According to the results, the 3C1-composite exhibits the largest effective volume fraction (φ_e) and interphase thickness (Δr) among the composites (φ_e = 12.53 Vol.-%). This largest effective volume fraction can be partly attributed to the perfect dispersion of 3C1-SiO_2 nanoparticles and subsequently the largest contact interphase with matrix, because φ_e is the sum of real volume fraction plus the interphase regions. The obtained interphase thickness in respective composites decreases with the following order: 3C1-composite > C0-composite > C8-composite > C16-composite. In comparison to C0-SiO_2, C8-SiO_2 shows a lower effective volume fraction despite the higher degree of hydrophobicity. It should be noted that the calculated values using Sumita's model

are not accurate enough and they suffer from the fact that simplifying assumptions are made in the calculation. Actually, the chemical modification of nanoparticles creates an organic coating layer on particle surface which increases the interphase thickness as shown in Figure 4.2.13. According to this schematic representation, there is no positive interaction existing between iPP and untreated C0-SiO_2 nanoparticles due to hydrophilic-hydrophobic repulsion, resulting in a weak interphase layer. After surface modification with silanes, the introduced unpolar alkyl chains stretch far away from the particle surface, interacting with iPP molecules at interface and increasing the thickness of the interphase. Accordingly, the interphase thickness in modified SiO_2-filled composites should be larger than in unmodified SiO_2-filled composite. However, the interphase thickness for a particle-polymer system is not a constant size because the interphase has no well-defined border with the bulk polymer. Therefore, the effective value of interphase thickness depends on many parameters such as surface covering of particle, chain flexibility, energy of molecular adsorption, the extent of chain entanglements at interface, etc. [130].

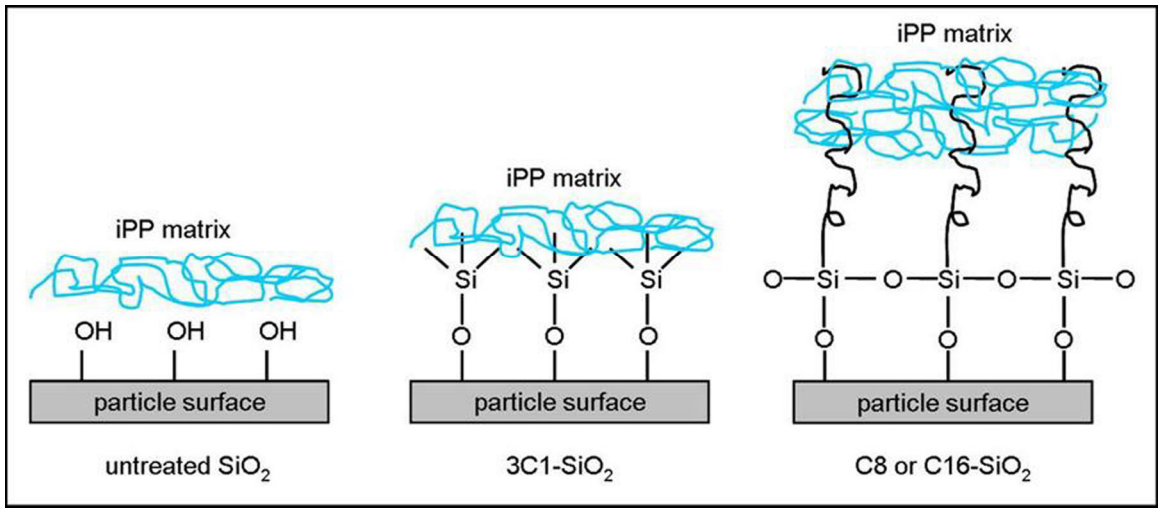

Figure 4.2.13: Schematic representation of the interphase in iPP/SiO_2 composites in this study.

4.2.5 Conclusion

The unmodified and silane-modified SiO_2 nanoparticles were compounded in iPP by direct melt blending in a twin-screw extruder. The SiO_2 nanoparticles show different degrees of hydrophobicity in which the 3C1-SiO_2 shows the highest degree of hydrophobicity by 63.5%, the C8-SiO_2 particles show hydrophobicity by 56%, whereas the C16-SiO_2 shows hydrophilic surface property like hydrophilic C0-SiO_2, although the C16-SiO_2 nanoparticles are pre-modified with organic silane by supplier. The hydrophilic surface property indicates a very low degree of organic modification for the C16-SiO_2 nanoparticles. According to visual assessment based on SEM pictures, the 3C1- and C8-SiO_2 nanoparticles show very good dispersion in iPP matrix whereas the C0- and C16-SiO_2 nanoparticles agglomerate in some degree. The incorporation of all SiO_2 particles into iPP increases the thermal stability of matrix but shows only little influence on the crystallization behaviour of iPP. The crystallinity of iPP matrix slightly increases in all iPP/SiO_2 composites. However, the spherulite size of iPP in all

composites is dramatically decreased compared to neat iPP. From DMTA results, both storage modulus and loss modulus of all iPP/SiO_2 nanocomposites are significantly increased compared to neat iPP. The glass transition temperature of polymer matrix in all composites is slightly increased up to 2.5 °C.

The tensile properties of iPP/SiO_2 composites show a direct correlation with alkyl chain length on particle surface. The tensile modulus of all composites is higher than that one of neat iPP and it decreases with increasing alkyl chain length. The maximum improvement in tensile modulus is by 21% achieved by C0-iPP/SiO_2 composite. The tensile strength and strain of composites increase with increasing alkyl chain length. The interfacial interaction parameter B_f calculated based on tensile strength of iPP/SiO_2 composites shows an increased tendency with increasing alkyl chain length on particle surface.

The values of fracture toughness of most iPP/SiO_2 composites are decreased compared to neat iPP except for 3C1-composite which exhibits an improvement in fracture toughness by 9%. In addition, the 3C1-composite shows the highest notched Charpy impact strength with an improvement by 45.6% among all iPP/SiO_2 composites. The C16-iPP/SiO_2 composite shows the lowest fracture toughness and Charpy impact strength among all iPP/SiO_2 composites. In both fracture toughness test and notched Charpy impact test, the results of surface-modified particle-filled iPP/SiO_2 composites increase with increasing degree of hydrophobicity/surface covering of respective nanoparticles.

According to the results obtained in this chapter, the following conclusions can be drawn: there are two important effects influencing the mechanical properties of iPP/SiO_2 composites. The one is the alkyl chain length on the particle surface which affects the tensile properties of the composites. The other one is the degree of surface covering of particles which affects the fracture toughness and the notched Charpy

impact strength. In order to achieve higher mechanical properties of unpolar polymers such as iPP, one should select a nanoparticle type with a higher degree of surface covering and long alkyl chain on the particle surface.

4.3 iPP/TiO_2 composites filled with different TiO_2 nanoparticles

Titanium dioxide (TiO_2) is the most popular pigment used today (70% of total pigments production). Chemically titanium dioxide occurs in three polymorphous varieties in nature: tetragonal rutile, anatase and rhombic brukite, in which the most common form is rutile and it is also the equilibrium phase at all temperatures [139]. The physical properties of rutile titania, including its transparency at visible wavelengths and its large index of refraction (2.73), have made it the most widely used white pigment for coatings, plastics and paper [140]. Upon UV light absorption, rutile TiO_2 becomes a photocatalyst via electronic reaction [141]:

$$H_2O + O_2 = OH^{\bullet} + HO_2^{\bullet}$$

The released free radicals can react with polymer matrix/organic additives, leading to weathering and chemical breakdown of the polymer matrix. In most exterior applications, the photo catalytic function of TiO_2 particles must be minimized via surface treatment. In addition to photolytic effect, untreated TiO_2 particles can result in flocculation (strong agglomeration) in liquid colorants or polymer matrix, leading to the following items [142, 143]:

- Loss of opacity: TiO_2 flocculates do not scatter light as primary particles.
- Color shift: flocculated TiO_2 particles have reduced tinting strength and undertone blueness.
- Poor flow: the rheology of a flocculated system is usually very thick. In most cases, stirring will thin the suspension, but flocculation will recur.

In order to reduce the photo catalytic effect and flocculation of TiO_2 particles, many commercial TiO_2 particles are pre-treated before supplying. In general, surface treatments of TiO_2 particles usually consist of aluminium oxide, silicon oxide, zinc oxide, and/or organic substrates such as silanes [144].

In this study, two types of Aeroxide® TiO_2 nanoparticles were used as fillers for iPP, i.e. unmodified hydrophilic C0-TiO_2 and silane-modified C8-TiO_2 nanoparticles. Both particle types have the same primary particle size by 21 nm. The iPP/TiO_2 composites were also prepared by direct melt blending in a twin-screw extruder and then injection moulded under the same processing conditions as iPP/SiO_2 composites. The particle content in iPP/TiO_2 composites was set as 0.4-, 0.8-, 1.3- and 2.3 Vol.-%. The properties of iPP/TiO_2 composites were characterized and discussed in this chapter.

4.3.1 Hydrophobicity and dispersion quality of TiO_2 nanoparticles

Based on the hydrophobicity measurements, the C8-TiO_2 nanoparticles show a relative high degree of hydrophobicity with a methanol-wettability by 75.6%, indicating a relative high degree of surface covering. The untreated TiO_2 nanoparticles were totally wetted by pure water, as expected. According to the contact angels of C0-TiO_2 (23.31) and C8-TiO_2 (143) (Table 1.2 , chapter 1.2.3), the surface tension is as follow: $\gamma_{C0-TiO_2} >> \gamma_{C8-TiO_2}$, resulting in: $\gamma_{iPP-C0-TiO_2} >> \gamma_{iPP-C8-TiO_2}$, indicating that the compatibility and dispersibility of C8-TiO_2 nanoparticles in iPP are much higher than those of C0-TiO_2 nanoparticles.

Figure 4.3.1 shows the SEM micrographs of iPP/TiO_2 composites containing 0.4-, 1.3- and 2.3 Vol.-% of C0- and C8-TiO_2 particles. It is evident that the surface modified C8-TiO_2 nanoparticles are very homogenously dispersed in iPP matrix at all particle contents. The well dispersed C8-TiO_2 particles clearly remain in the nanosized range (less than 100 nm). No large particle flocculates/agglomerates in microsized range

are observed even at higher particle contents. By contrast, the unmodified C0-TiO_2 nanoparticles result in a higher degree of agglomeration/flocculation which increases with increasing particle content. At 2.3 Vol.-% of C0-TiO_2 particles, large flocculates/agglomerates with a size of about 20 µm are observed as shown in SEM micrographs. The high degree of agglomeration of C0-TiO_2 nanoparticles can firstly be attributed to relative strong interactions among nanoparticles themselves due to formation of hydrogen bonds with bond energy by about 20 kJ/mol [63]. Secondly it can be attributed to the large interfacial tension between C0-TiO_2 particles and iPP matrix. The presence of large C0-TiO_2 agglomerates indicates that the shear forces during compounding process were not effective enough to break them down.

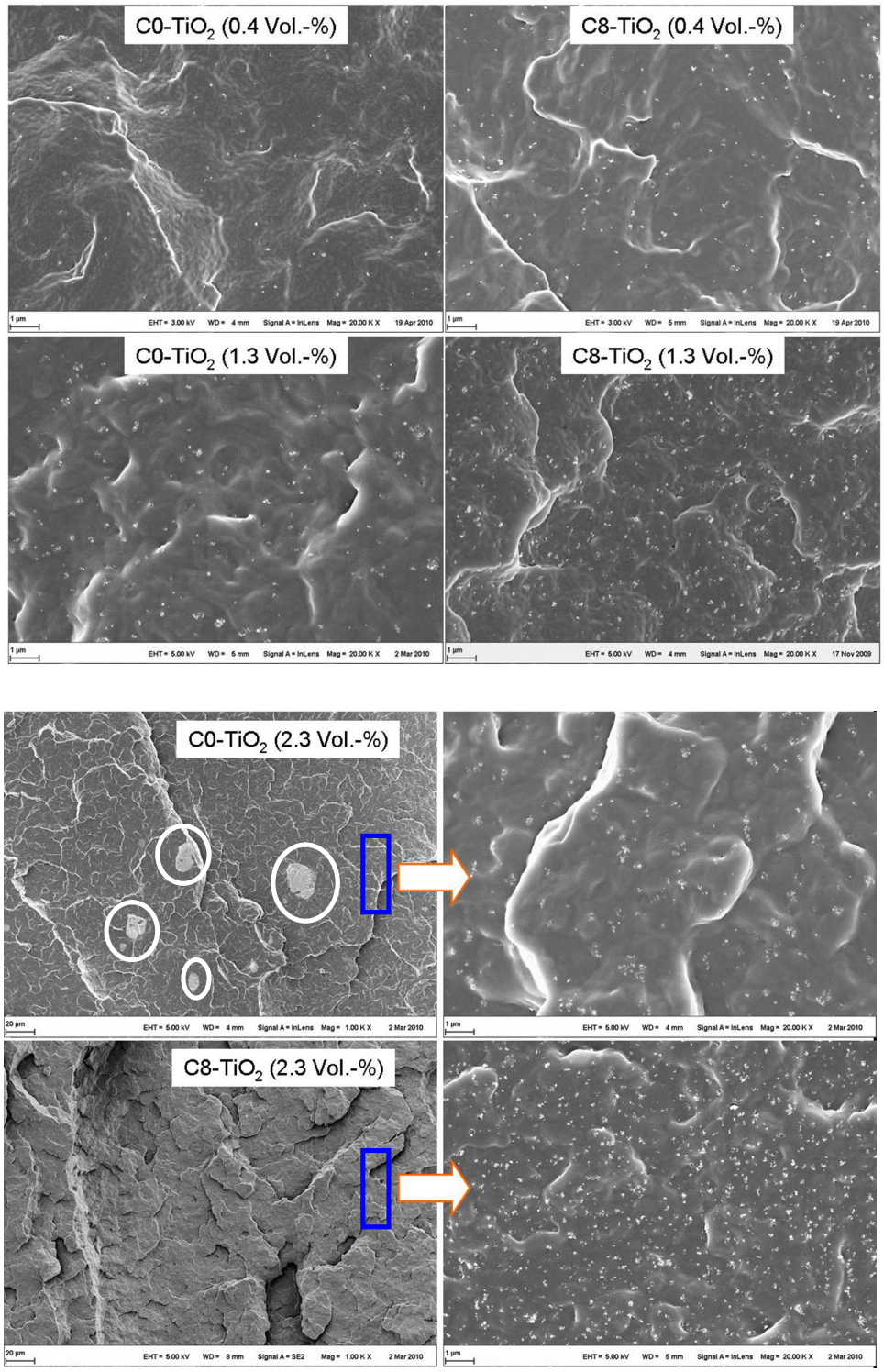

Figure 4.3.1: SEM micrographs of C0- and C8-iPP/TiO_2 composites with different TiO_2 contents as shown in the pictures. The circles in pictures show the large agglomerates of C0-TiO_2 particles. The quadrangles show the positions which are magnified.

4.3.2 Mechanical properties

Tensile properties

The tensile properties of iPP/TiO_2 composites were measured and analyzed. Figure 4.3.2 and 4.3.3 show the tensile properties of C0-and C8-iPP/TiO_2 composites as a function of particle content, respectively.

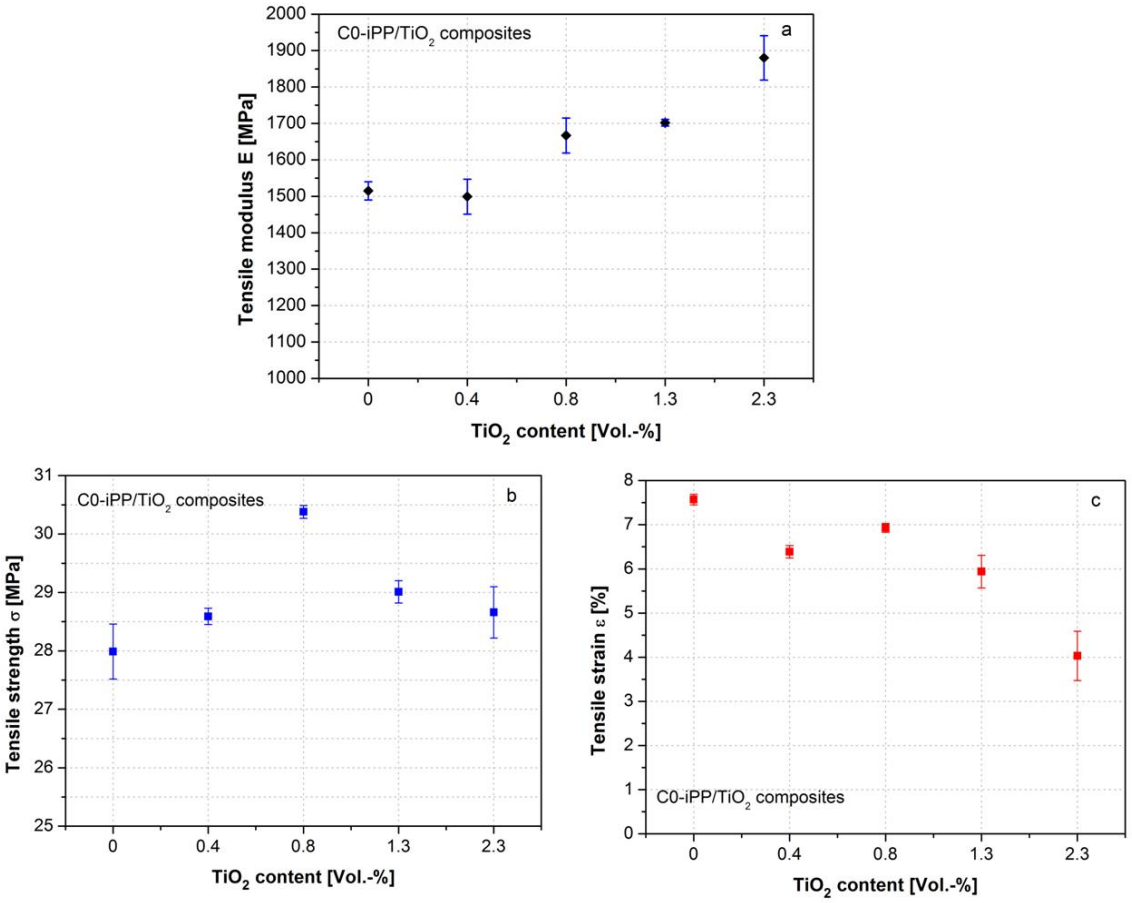

Figure 4.3.2: Tensile properties of C0-iPP/TiO_2 composites as a function of particle content.

As shown in Figure 4.3.2, it is evident that the tensile modulus of C0-iPP/TiO_2 composites increases with increasing particle loading. This increase should be attributed to the addition of rigid particles into polymer matrix. The maximum improvement in tensile modulus is by 24.1% achieved by C0-iPP/TiO_2 composite with

2.3 Vol.-% of particles. The tensile strength of C0-iPP/TiO_2 composites increases with increasing particle content up to 0.8 Vol.-%, at which a maximum improvement is obtained by 8.5%, and then decreases with further particle loading. All C0-iPP/TiO_2 composites show improved tensile strength compared to neat iPP. The tensile strain of C0-iPP/TiO_2 composites clearly decreases in comparison with neat iPP and the value decreases with increasing particle content due to increased stiffness, as expected.

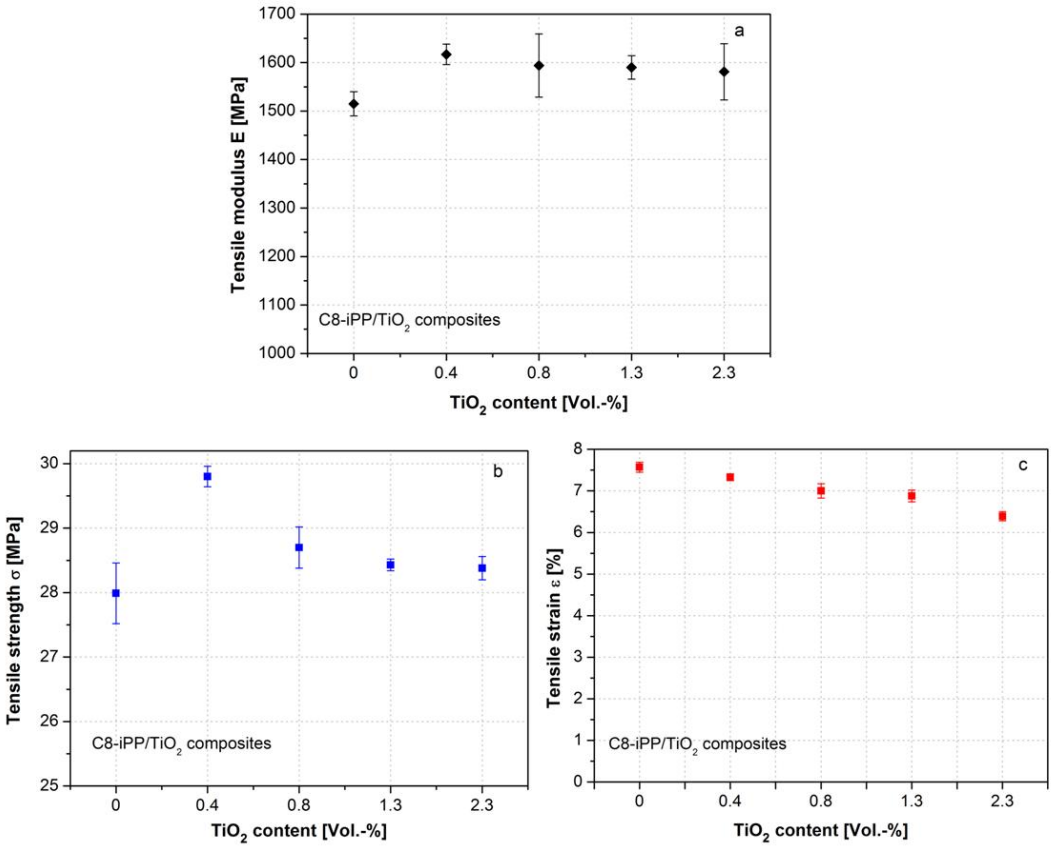

Figure 4.3.3: Tensile properties of C8-iPP/TiO_2 composites as a function of particle content.

As shown in Figure 4.3.3, all C8-iPP/TiO_2 composites exhibit slightly increased tensile modulus compared to neat iPP. Unlike C0-iPP/TiO_2 composites which show evident increasing tendency of tensile modulus with increasing particle content, the

C8-iPP/TiO_2 composites show comparable tensile modulus as particle content increases. A possible explanation is the plasticizing effect of surface modified C8-TiO_2 particles. At 0.4 Vol.-% of C8-TiO_2 particles, the tensile strength attains a maximum with an improvement by 6.5%. The tensile strength of C8-iPP/TiO_2 composites decreases slightly with increasing particle content. Similar to C0-iPP/TiO_2 composites, the C8-iPP/TiO_2 composites exhibit slightly decreased tensile strain with increasing particle content. All results of iPP/TiO_2 composites obtained by tensile test are summarized in Table 4.6.

Table 4.6: Tensile results of all C0- and C8-iPP/TiO_2 composites

Samples/Particle content [Vol.-%]		Tensile modulus E [MPa]	Tensile strength σ [MPa]	Tensile strain ε [%]
neat iPP	0	1515 ± 25	27.99 ± 0.47	7.57 ± 0.12
C0-iPP/TiO_2	0.4	1499 ± 47	28.59 ± 0.14	6.39 ± 0.14
	0.8	1667 ± 48	30.38 ± 0.11	6.93 ± 0.10
	1.3	1702 ± 9	29.01 ± 0.19	5.94 ± 0.37
	2.3	1880 ± 61	28.66 ± 0.44	4.03 ± 0.56
C8-iPP/TiO_2	0.4	1617 ± 21	29.80 ± 0.16	7.33 ± 0.08
	0.8	1594 ± 65	28.70 ± 0.32	7.00 ± 0.17
	1.3	1590 ± 24	28.43 ± 0.09	6.88 ± 0.14
	2.3	1581 ± 58	28.38 ± 0.18	6.39 ± 0.11

Based on tensile results, the C0-iPP/TiO_2 composites show higher tensile modulus but lower tensile strain than respective C8-iPP/TiO_2 composites. This can be explained that the alkyl chains on C8-TiO_2 particles can act as plasticizers reducing

stiffness. In addition, the maximum tensile strength occurs at 0.8 Vol.-% of C0-TiO_2 particles whereas it is obtained at 0.4 Vol.-% in case of C8-TiO_2 particles. This indicates that the interfacial interactions between iPP and C8-TiO_2 particles are stronger than those between iPP and C0-TiO_2 particles. Therefore, the C8-iPP/TiO_2 composite results in a high tensile strength/strain balance at a lower particle content compared to C0-iPP/TiO_2 composite.

Fracture toughness and morphology

The fracture toughness of iPP/TiO_2 composites was performed by using CT test. The load-displacement curves of all iPP/TiO_2 composites are shown in Figure 4.3.4. The maximum load values F_{max} of respective samples are taken to calculate the fracture toughness K_{IC}, because the initial crack on CT-samples began to propagate at this point.

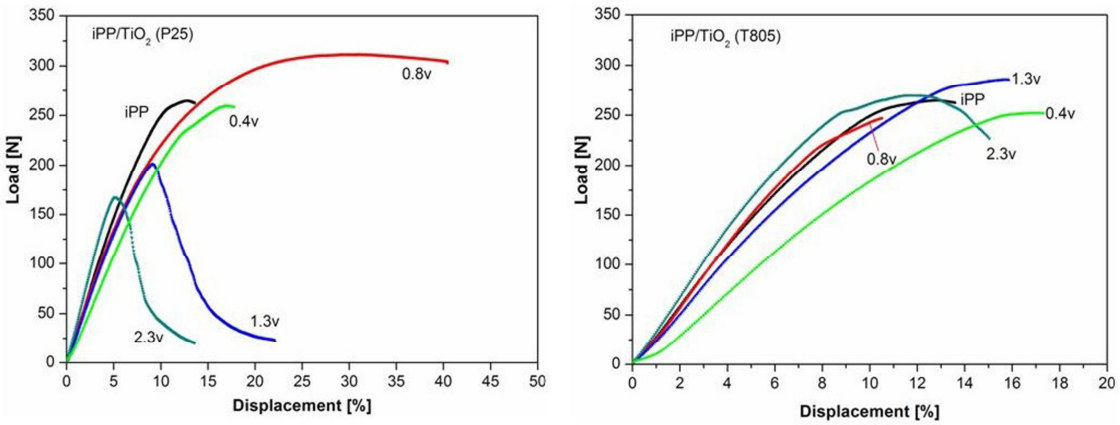

Figure 4.3.4: Load-displacement curves of C0- (left) and C8-iPP/TiO_2 (right) composites obtained by CT test.

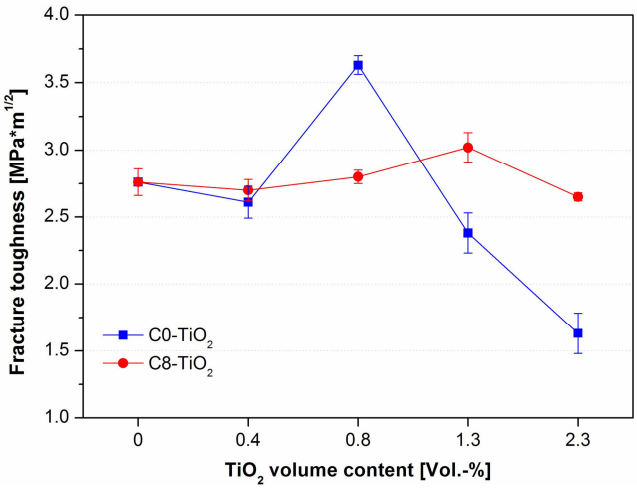

Figure 4.3.5: Fracture toughness of neat iPP and all iPP/TiO_2 composites as a function of particle loading.

The fracture toughness K_{IC} calculated from the maximum load F_{max} are shown in Figure 4.3.5. It can be seen that the fracture toughness of C0-iPP/TiO_2 composites increases up to 0.8 Vol.-% of particles, at which a maximum improvement by 32.0% is achieved. Above 0.8 Vol.-%, the fracture toughness decreases dramatically with increasing particle content. At 1.3- and 2.3 Vol.-% of C0-TiO_2 particles, the reduction in fracture toughness is by 14% and 41%, respectively. This large reduction in fracture toughness should be attributed to increasing agglomeration of C0-TiO_2 particles in iPP matrix as already shown in Figure 4.3.1 (chapter 4.3.1). The large agglomerates could create micro-cracks during easy particle debonding from matrix due to poor interfacial adhesion, promoting macro-crack propagation and leading to brittle fracture of samples. In C8-iPP/TiO_2 composites, the fracture toughness slightly increases with increasing particle content up to 1.3 Vol.-%, at which the fracture toughness reaches its maximum with an improvement by about 10.0% compared to neat iPP. At 2.3 Vol.-% of C8-particles, the fracture toughness is decreased by 4%. The reason should be that the particles/agglomerates at high concentration in iPP matrix will build up a

three dimensional network structure that leads to a brittle behaviour of composites. The fracture surface and morphology of iPP/TiO_2 composites are shown in Figure 4.3.6. From the figures, the C0-iPP/TiO_2 composite with 0.8 Vol.-% of particles shows macro polymer deformation on the fracture surface, whereas the C0-iPP/TiO_2 composites containing 1.3- and 2.3 Vol.-% of particles show much smoother fracture surfaces, especially at 2.3 Vol.-% of particles. The C0-iPP/TiO_2 composites show decreased resistance against fracture growth with increasing particle content. The C8-iPP/TiO_2 composites containing 0.8-, 1.3- and 2.3 Vol.-% of particles show similar fracture surfaces with fracture zones. Among three composites, the composite with 2.3 Vol.-% of particles shows the smoothest fracture surface indicating the lowest resistance against fracture propagation. More details in fracture zones are shown in Figure 4.3.7.

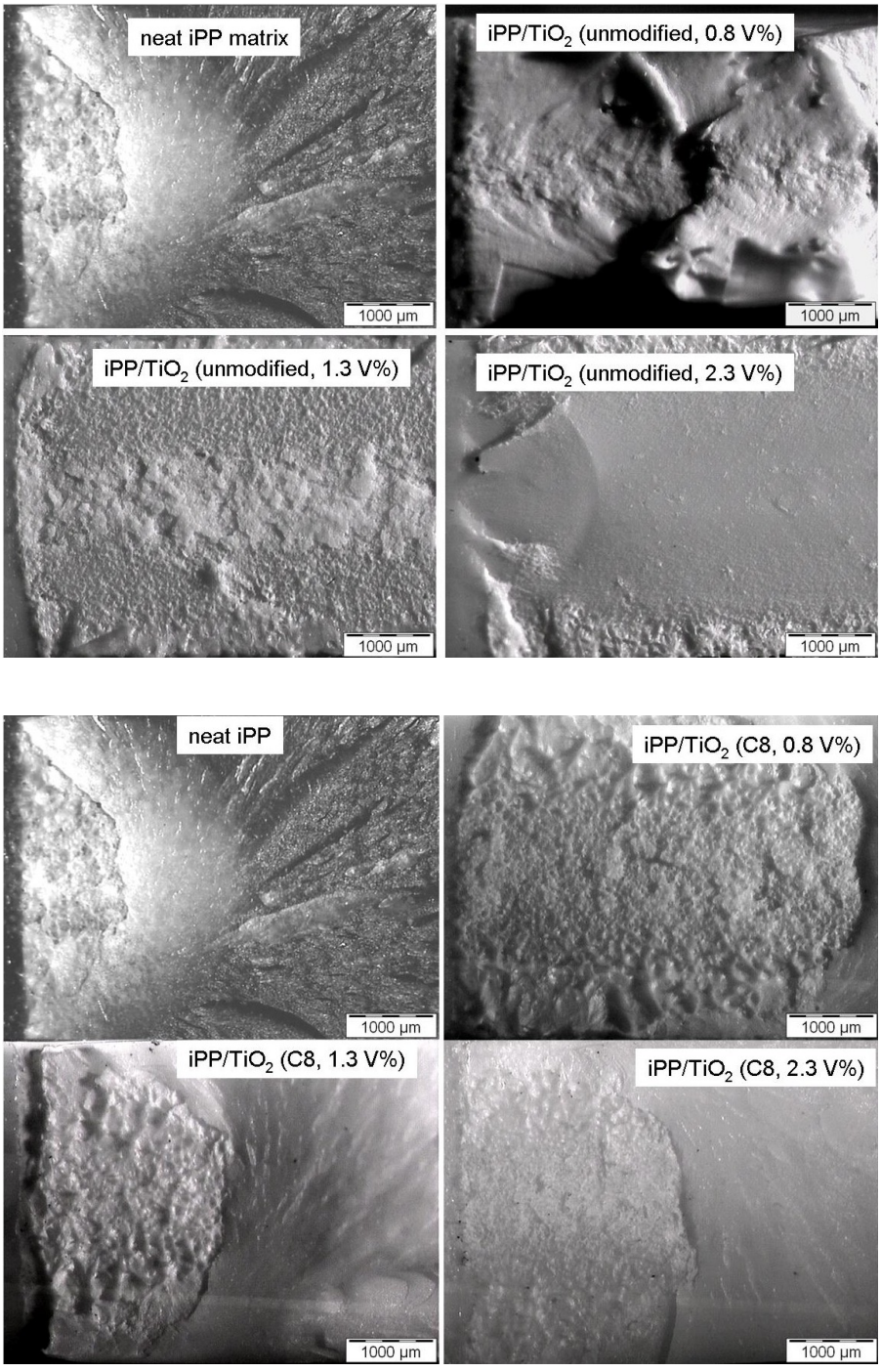

Figure 4.3.6: Overview of fracture surfaces of C0- and C8-iPP/TiO_2 composites after CT test obtained by SEM examination.

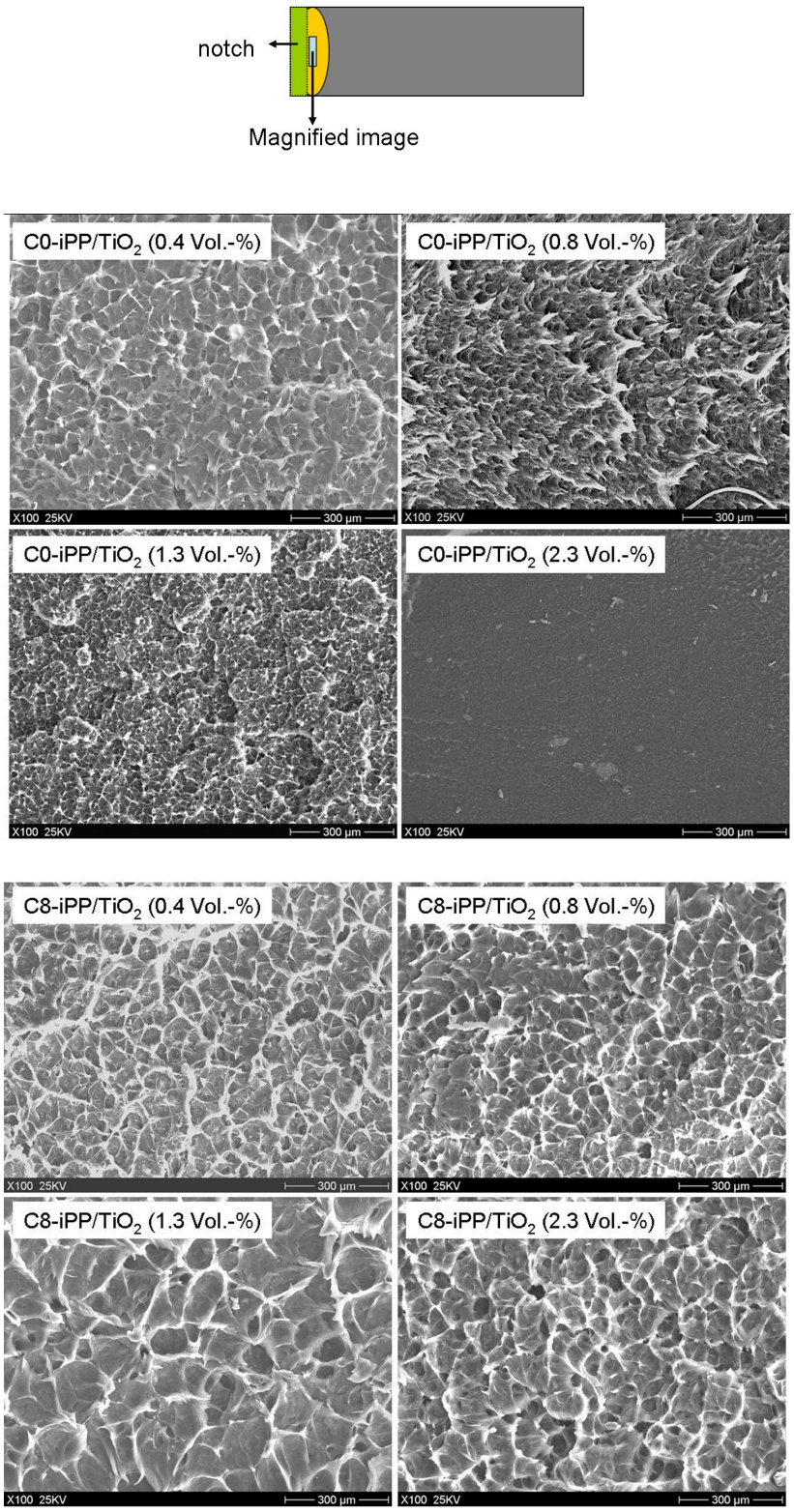

Figure 4.3.7: Close-view into the fracture zones on the surfaces of fractured C0- and C8-iPP/TiO_2 composites after CT test. The pictures are taken from the position at the top of initial crack on CT-samples.

As mentioned in chapter 4.2.4, the fracture toughness of a polymer composite is a result of combined effects related to the formation of dimples and polymer deformation by coalescence of voids as shown in Figure 1.2.20 (chapter 1.2.4). As shown in Figure 4.3.7, the C0-iPP/TiO_2 composite with 0.8 Vol.-% of particles reveals the maximum viscoelastic deformation on the fracture surface. The fractured surfaces of other C0-composites show decreased deformation behaviour; especially the C0-composite with 2.3 Vol.-% of TiO_2 particles shows a very smooth fracture surface on which large agglomerates of particles are observed, indicating a brittle fracture. This fracture morphology correlates well with the fracture toughness of C0-iPP/TiO_2 composites.

In C8-iPP/TiO_2 composites, the C8-TiO_2 particles will not easily detach from the iPP matrix due to increased interfacial adhesion. Additionally, the increased matrix-particle adhesion leads to formation of more dimples during fracture process due to a stronger stress transfer effect than easily debonded C0-TiO_2 particles. This stress transfer effect depends on particle loading and is more pronounced at higher particle contents. On the other hand, higher particle content leads to smoother fracture surface. As a result, the C8-iPP/TiO_2 composite containing 1.3 Vol.-% of particles results in the highest fracture toughness among C8-composites. The fracture toughness (total energy dissipation) in C8-iPP/TiO_2 composites does not differ much during fracture process. This correlates well with their comparable fracture toughness as shown in Figure 4.3.7.

Notched Charpy impact strength

The notched Charpy impact strength of all iPP/TiO_2 composites was measured and analyzed. The results are shown in Figure 4.3.8.

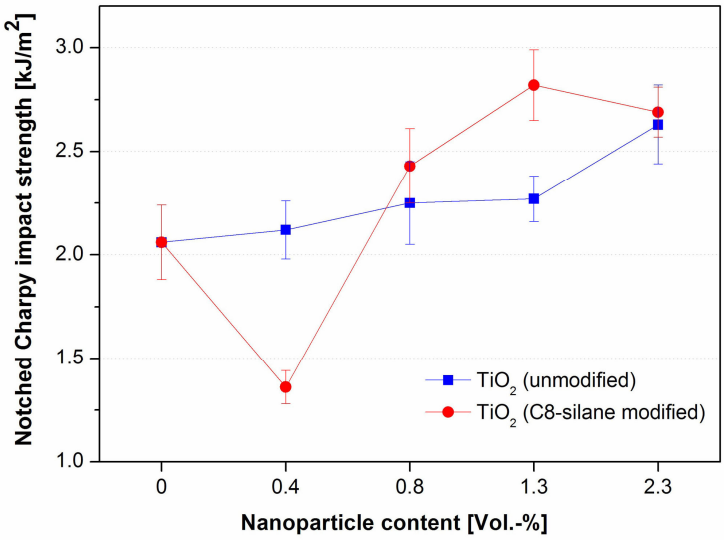

Figure 4.3.8: notched Charpy impact strength of neat iPP and all iPP/TiO_2 composites as a function of particle loading.

As observed, the notched Charpy impact strength of C0-iPP/TiO_2 composites increases with increasing particle content and all values are higher than that one of neat iPP. The maximum improvement at 2.3 Vol.-% is by 28.0%. In C8-iPP/TiO_2 composites, the impact strength increases with increasing particle loading up to 1.3 Vol.-% of particles, at which the maximum improvement is by 37.2%. Higher particle loading does not lead to higher improvement. At 2.3 Vol.-% of C8-TiO_2 particles, the improvement in notched Charpy impact strength is by 31.1%. The C8-composite containing 0.4 Vol.-% of TiO_2 particles shows dramatically decreased impact strength compared to neat iPP, which is unexplainable and will be neglected.

From 0.8 Vol.-% of TiO_2 particles, the C8-composites exhibit higher impact strength than respective C0-composites. This should be attributed to a better matrix-particle adhesion and better dispersion quality of C8-TiO_2 particles in iPP.

4.3.3 Thermal and thermo-mechanical properties

TGA results

The thermal stability of iPP/TiO_2 composites was investigated by TGA. Figure 4.3.9 shows the curves of weight loss of C8-iPP/TiO_2 composites as a function of temperature. The C0-iPP/TiO_2 composites show a similar thermal behaviour as C8-iPP/TiO_2 composites. The onset degradation temperature (T_{onset}), the temperatures at 20% ($T_{20\%}$) and 50% weight loss ($T_{50\%}$) of C0- and C8-iPP/TiO_2 composites are listed in Table 4.7.

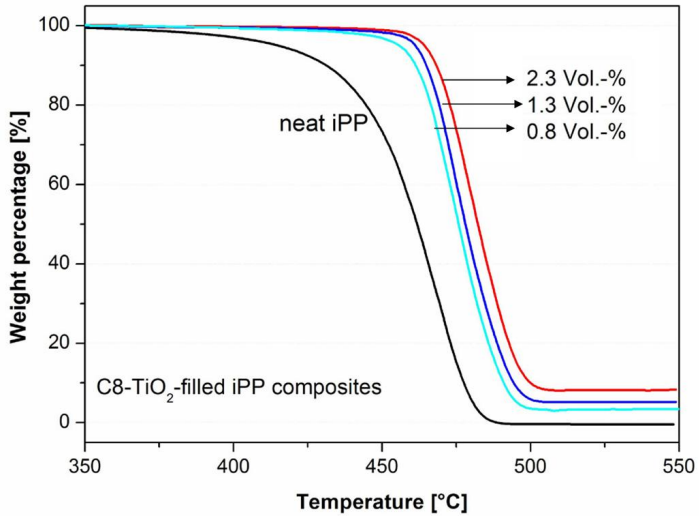

Figure 4.3.7: Weight loss as a function of temperature for C8-iPP/TiO_2 composites obtained by TGA.

It is evident that the thermal stability T_{onset} of iPP/TiO_2 composites increases slightly with increasing particle content, this increasing tendency is especially significant in C8-iPP/TiO_2 composites. At 2.3 Vol.-% of TiO_2 particles, the respective improvements in T_{onset} are by 23.7 °C for C8-iPP/TiO_2 composite and by 21.4 °C for C0-iPP/TiO_2 composite. Additionally, the C8-composites show a slightly higher thermal stability than the respective C0-composites. This correlates with the higher interfacial

interactions between iPP matrix and C8-TiO_2 nanoparticles due to surface modification with silane. Nevertheless, the difference is not significant.

Table 4.7: TGA results of C0- and C8-iPP/TiO_2 composites

Particle content [Vol.-%]	C8-iPP/TiO_2			C0-iPP/TiO_2		
	$T_{20\%}$ [°C]	$T_{50\%}$ [°C]	T_{onset} [°C]	$T_{20\%}$ [°C]	$T_{50\%}$ [°C]	T_{onset} [°C]
neat iPP	447.6	464.9	443.7	447.6	464.9	443.7
0.4	464.6	478.2	460.3	464.4	475.1	462.2
0.8	466.5	479.7	462.3	469.7	476.0	462.6
1.3	469.4	480.2	466.0	470.8	478.3	464.2
2.3	472.7	482.9	467.4	471.2	480.9	465.1

DSC results

The thermal and crystalline behaviour of iPP/TiO_2 composites were examined by using DSC. Figure 4.3.8 shows the melting and the crystalline peaks of neat iPP and C0-iPP/TiO_2 composites. The C8-iPP/TiO_2 composites show similar DSC curve shapes as C0-iPP/TiO_2 composites.

It can be seen that the position of melting peaks of iPP composites doesn't change significantly compared to neat iPP. On the contrary, the crystalline peaks of composites shift significantly to higher temperatures in comparison to neat iPP. The obtained melting temperature (T_m), the crystalline temperature (T_c) and the crystallinity of iPP matrix (X_c) for all samples are listed in Table 4.8.

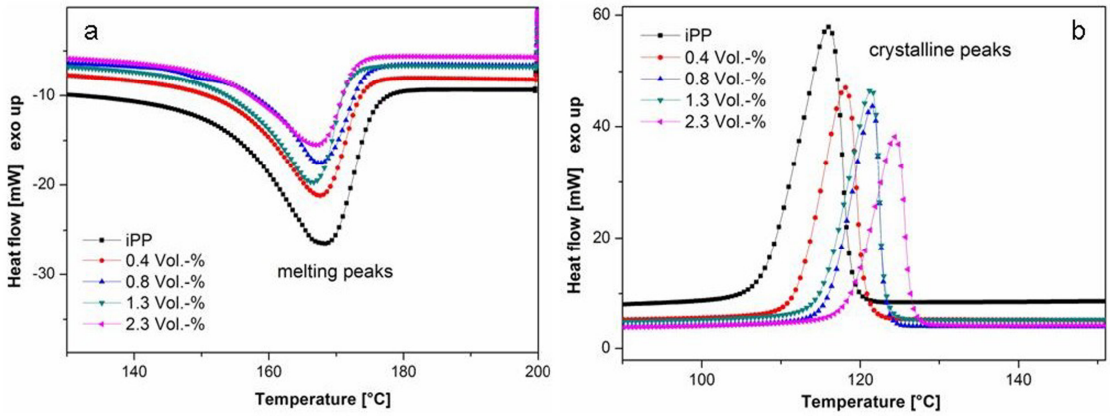

Figure 4.3.8: DSC results of C0-iPP/TiO_2 composites: (a) melting curves and (b) crystalline curves.

Table 4.8: DSC results of C0- and C8-iPP/TiO_2 composites

Particle content [Vol.-%]	C8-iPP/TiO_2 composite			C0-iPP/TiO_2 composite		
	T_m [°C]	T_c [°C]	X_c [%]	T_m [°C]	T_c [°C]	X_c [%]
neat iPP	168.4	116.0	48.4	168.4	116.0	48.4
0.4	166.7	116.4	46.9	167.1	117.5	47.1
0.8	167.5	116.9	44.7	167.4	121.3	46.6
1.3	168.0	116.9	43.1	166.6	121.5	44.5
2.3	167.2	116.7	40.5	167.2	123.7	42.0

It is evident that the melting temperature T_m of iPP in all iPP/TiO_2 composites is not significantly affected by addition of TiO_2 nanoparticles, and there is no clear relationship between the melting temperature of iPP in iPP/TiO_2 composites and the particle content as reported in [128]. In addition, no evident improvements in crystalline temperatures of C8-iPP/TiO_2 composites are observed. By contrast, the crystalline temperatures of C0-iPP/TiO_2 composites are obviously increased compared to neat iPP, and the improvement in T_c clearly increases with increasing

particle content. At 2.3 Vol.-% of C0-TiO_2 particles, the crystalline temperature is 7.7 °C higher than that of neat iPP. This result indicates that the unmodified C0-TiO_2 particles reveal much stronger nucleation effect than modified C8-TiO_2 particles. Similar result are obtained in case of SiO_2 nanoparticles where that unmodified C0-SiO_2 nanoparticles show a stronger nucleation effect than surface modified SiO_2 nanoparticles (chapter 4.2.3). Supaphol and co-workers have also reported that untreated TiO_2 particles show a higher nucleating effect than chemically treated TiO_2 particles [60]. As a result of higher nucleation effect of C0-TiO_2 particles, the crystallinity of iPP matrix in C0-iPP/TiO_2 composites is slightly higher than that one of respective C8-composites. Additionally, the crystallinity of iPP matrix in both C0- and C8-composites decreases with increasing particle content and the X_c values in all iPP/TiO_2 composites are clearly decreased compared to neat iPP, especially at high particle content. Figure 4.3.9 shows the morphology of spherulite features of iPP in C0- and C8-iPP/TiO_2 composites with 2.3 Vol.-% of particles. Similar to iPP/SiO_2 composites, no crystal structure is observed in both iPP/TiO_2 composites at such a high TiO_2 concentration..

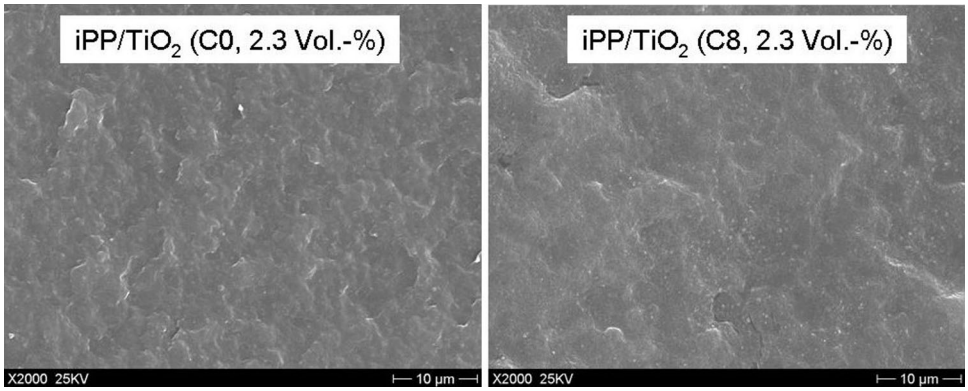

Figure 4.3.9: SEM images for “spherulite structure” and size in iPP/TiO_2 composites.

DMTA results

The dynamic-mechanical thermal properties of iPP/TiO_2 composites were investigated by using DMTA. The storage modulus E' at 23 °C and the β-transition temperature of neat iPP and all iPP/TiO_2 composites are summarised in Table 4.9.

Table 4.9: DMTA results of C0- and C8-iPP/TiO_2 composites

Particle content [Vol.-%]	C8-iPP/TiO_2 composite		C0-iPP/TiO_2 composite	
	E' at 23 °C [MPa]	T_β [°C]	E' at 23 °C [MPa]	T_β [°C]
neat iPP	1762 ± 131	12.4	1762 ± 131	12.4
0.4	1985 ± 77	12.5	1900 ± 71	12.4
0.8	2080 ± 99	13.5	2027 ± 59	13.5
1.3	2175 ± 123	14.0	2200 ± 83	12.5
2.3	2340 ± 47	13.9	2401 ± 41	12.5

It is observed that the storage moduli of iPP/TiO_2 composites are overall improved compared to neat iPP. In both composite series, increasing particle content leads to increased storage modulus despite the reduction in crystallinity of iPP matrix. The maximum improvements at 2.3 Vol.-% of particles are by 33% for C8-iPP/TiO_2 composite and by 36% for C0-iPP/TiO_2 composite, respectively. The differences in storage modulus between C0-iPP/TiO_2 composites and C8-iPP/TiO_2 composites are not significant. The β-relaxation temperature of iPP in iPP/TiO_2 composites is slightly increased with maximum improvements by 1.6 °C and 1.1 °C for C8-iPP/TiO_2 (1.3 Vol.-%) and C0-iPP/TiO_2 (0.8 Vol.-%), respectively. This slight increase in glass transition temperature of iPP can be attributed to reduction in the mobility of iPP molecules due to particle hindrance and decrease in crystallinity of iPP in iPP/TiO_2 composites.

4.3.4 Weathering/Chalking effect of TiO_2 particles on iPP/TiO_2 composites

Some pigments, of which TiO_2 is the most known, are photochemically active and can catalyse the photodegradation of the polymer matrix in which they reside. The untreated TiO_2 particles with OH-groups on particle surface especially that ones with anatas-structure will absorb UV light causing cyclic reduction and oxidation of titanium ions via electronic reactions as follows [135]:

$$Ti^{4+}OH^- + h\nu \rightarrow Ti^{3+} + OH^{\bullet}$$
$$Ti^{3+} + O_2 \rightarrow Ti^{4+}O_2^-$$
$$Ti^{4+}O_2^- + H_2O \rightarrow Ti^{4+}OH^- + HO_2^-$$

In polymer/TiO_2 composites, the released free radicals at the particle-matrix interface will accelerate the photodegradation of the polymer, resulting in weathering/chalking of polymers as shown in Figure 4.3.10.

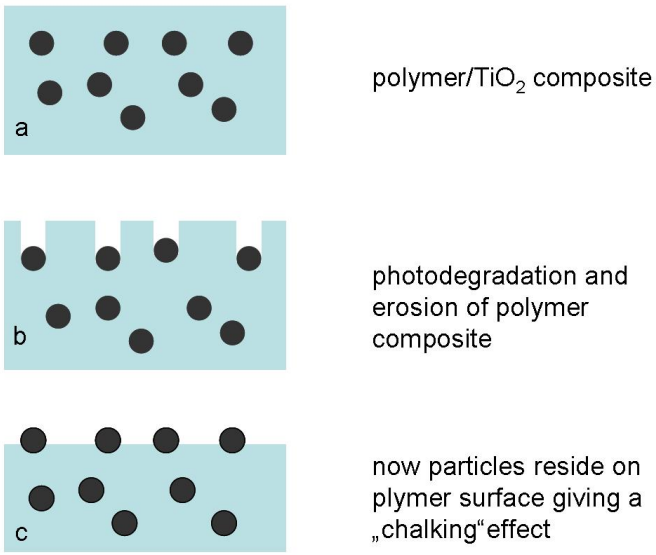

Figure 4.3.10: Mechanism of weathering/chalking of polymers due to photoactive TiO_2 particles [135].

This weathering/chalking effect of untreated TiO_2 particles is usually suppressed by the surface treatment with inorganic (e.g. Al_2O_3, SiO_2, ZrO_2) and/or organic substrates

(e.g. silanes). The surface treatment traps the photochemically induced radicals on the TiO_2 surface and prevents them to go into a secondary photochemical reactions with polymers [135].

Figure 4.3.11 shows the tensile bars of C0- and C8-iPP/TiO_2 composites with 2.3 Vol.-% of respective particles. The samples were exposed in air for 30 days before the pictures were taken. It can be seen that the weathering/chalking is not significant in both iPP composites although one of which is filled with untreated TiO_2 nanoparticles. This indicates that iPP has a high resistance against photodegradation caused by untreated TiO_2 particles. It should be noted that weathering depends on the duration and the environments of exposure.

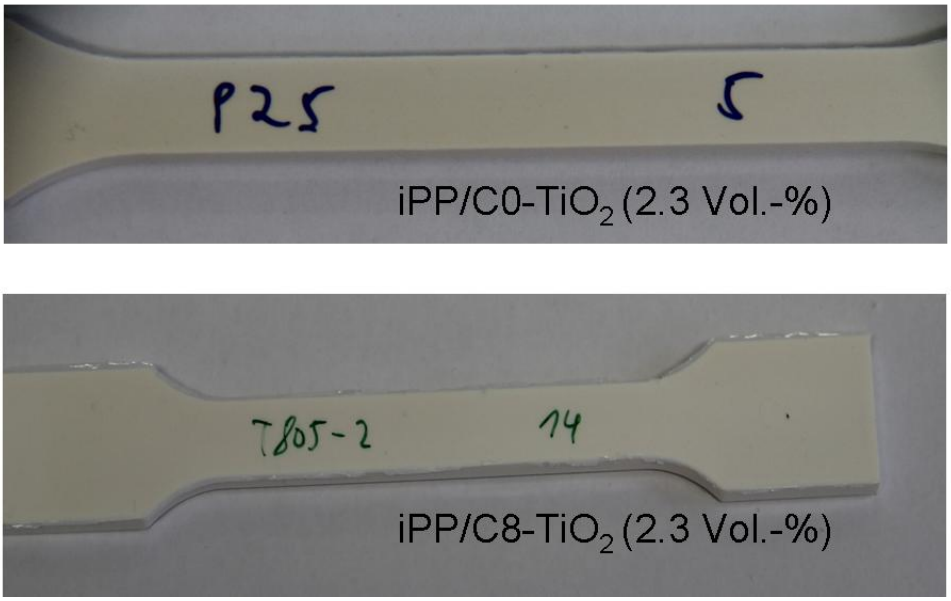

Figure 4.3.11: Tensile samples of C0- and C8-iPP/TiO_2 composites (2.3 Vol.-%) after exposure in air for 30 days, no weathering is observed.

4.3.5 Conclusion

Two types of TiO_2 particles were incorporated into iPP. The iPP/TiO_2 composites were prepared by direct melt blending in a twin-screw extruder. The properties of produced composites were characterized and discussed. The silane-modified C8-TiO_2 nanoparticles show a degree of hydrophobicity by 75.6%. According to SEM examination, the C8-TiO_2 particles are homogeneously dispersed in iPP matrix, whereas untreated C0-TiO_2 particles result in a high degree of agglomeration/flocculation. The TGA results show that the C8-iPP/TiO_2 composites exhibit higher thermal stability than C0-iPP/TiO_2 composites due to increased interfacial interactions. According to DSC results, the C0-TiO_2 particles show a stronger nucleation effect than surface modified C8-TiO_2 particles, indicated by much higher crystalline temperatures of iPP matrix in C0-iPP/TiO_2 composites. Similar to iPP/SiO_2 composites, the crystallinity of iPP matrix in iPP/TiO_2 composites is decreased and doesn't benefit to the mechanical properties of composites. Both C0- and C8-composites show increased storage moduli with increasing particle content. Furthermore, the C8-composites show higher fracture toughness and notched Charpy impact strength than respective C0-composites at higher particle contents. This result should be attributed to increased matrix-particle interchanges in C8-composites. No difference in weathering behaviour was observed between C0- and C8-iPP/TiO_2 composites. According to the results obtained in this chapter, the surface pre-treatment of TiO_2 particles strongly affects the dispersion quality and the nucleation effect of particles in iPP. Conversely, the effect of surface pre-treatment is not significant on the mechanical, thermal and weathering properties of iPP/TiO_2 composites.

4.4 Influence of nanoparticle nature on properties of iPP composites

An important parameter which strongly affects the thermal and mechanical properties of particulate-filled polymer composites is the chemical nature of nanoparticles. Different particles with similar size and shape can differ in chemical composition and related chemical activity as well as their surface nature. It is known that unmodified TiO_2 nanoparticles (metal oxide) are chemically more active as electronic donator than unmodified SiO_2 nanoparticles (non-metal oxide) [72]. The surface polarity of unmodified TiO_2 particles is higher than that one of unmodified SiO_2 particles as shown in Table 1.2 in chapter 1.2.3, i.e. the surface tension $\gamma_{(C0-TiO_2)} >> \gamma_{(C0-SiO_2)}$ [72]. As a result of higher surface polarity, the compatibility and adhesion between C0-TiO_2 and iPP matrix are lower than those between C0-SiO_2 and iPP matrix. Thus, the C0-TiO_2 particles result in a higher degree of agglomeration in iPP matrix than C0-SiO_2 particles as shown in SEM micrographs in Figures 4.2.4 and 4.3.1. After surface modification with octylsilane, C8-TiO_2 nanoparticles show a higher degree of hydrophobicity than C8-SiO_2 particles (75.6% vs. 56.2%) according to hydrophobicity test in this study, indicating a higher degree of covering on particle surface with alkyl groups. In addition, C8-TiO_2 particles have a larger contact angle (143) than C8-SiO_2 particles (136) as given in Table 1.2 in chapter 1.2.3, indicating a lower surface tension of C8-TiO_2 particles, i.e. $\gamma_{(C8-TiO_2)} < \gamma_{(C8-SiO_2)}$, but the difference should be not large.

The thermal properties of C0- and C8-iPP/SiO_2 and iPP/TiO_2 composites containing 2.3 Vol.-% of respective particles are summarized in Table 4.10.

Table 4.10: Thermal properties of C0- and C8-iPP/SiO_2 and iPP/TiO_2 composites containing 2.3 Vol.-% of respective nanoparticles

Samples	Thermal stability T_{onset} [°C]	Crystalline temperature T_c [°C]	Crystallinity X_c [%]
Neat iPP	443.7	116.0	48.4
C0-iPP/SiO_2	449.1	116.9	48.3
C0-iPP/TiO_2	465.1	123.7	42.0
C8-iPP/SiO_2	452.2	116.6	46.5
C8-iPP/TiO_2	467.4	116.7	40.5

Based on the results in Table 4.10, it can be seen that the thermal stability of C0- and C8-iPP/TiO_2 composites is 15°C higher than the respective C0- and C8-iPP/SiO_2 composites. Because of this significant reinforcing effect in thermal stability, TiO_2 nanoparticles are usually used as flame retardant in many polymers to improve the thermal stability of final products [60]. In terms of crystalline behaviour, C0-iPP/TiO_2 composite (2.3 Vol.-%) shows a higher crystalline temperature by 7.1°C than C0-iPP/SiO_2 composite (2.3 Vol.-%), indicating a stronger heterogeneous nucleation effect of C0-TiO_2 particles. This should be attributed to the different chemical structures of TiO_2 and SiO_2 particles as well as to the different surface polarity as mentioned above. The C8-iPP/SiO_2 and C8-iPP/TiO_2 composites show similar crystalline temperatures of iPP matrix, indicating a similar nucleation effect of these two particle types. In the case of crystallinity of iPP matrix, both iPP/SiO_2 composites show much higher X_c degrees than both iPP/TiO_2 composites.

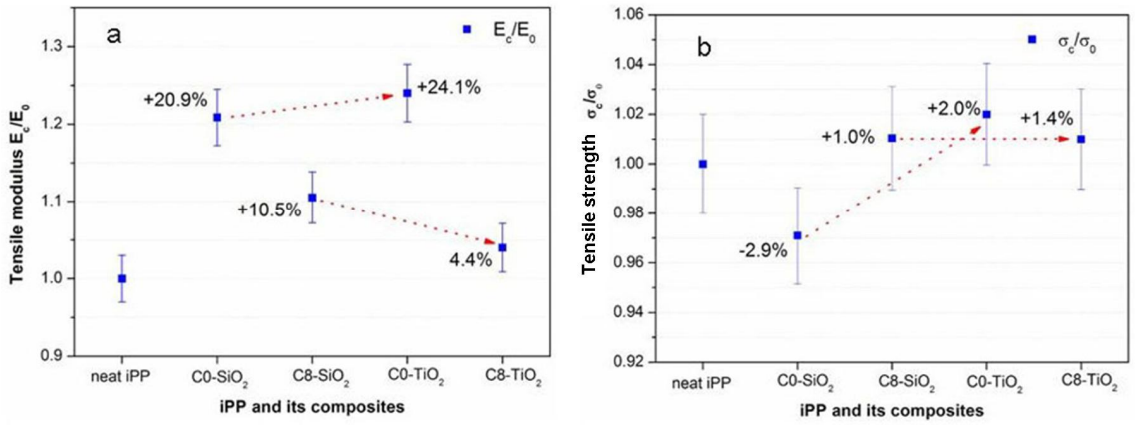

Figure 4.4.1: Influence of particle type on tensile properties of iPP composites containing 2.3 Vol.-% of particles (TiO_2 vs. SiO_2): (a) tensile modulus and (b) tensile strength.

The tensile modulus and tensile strength of discussed composites based on the values of neat iPP are shown in Figure 4.4.1. From Figure 4.4.1a, the C0-iPP/TiO_2 composite (2.3 Vol.-%) shows a higher tensile modulus than C0-iPP/SiO_2 composite (2.3 Vol.-%) despite lower crystallinity of iPP matrix, the respective improvements are by 24.1% vs. 20.9%. The reasons could be as follows: firstly, the metal oxide C0-TiO_2 particles are harder than non-metal oxide C0-SiO_2 particles; secondly, C0-TiO_2 particles result in larger agglomerates/flocculates in iPP matrix as shown in Figure 4.3.1, which lead to a stiffer behaviour of iPP composite. Unlike C0-composites, the C8-iPP/SiO_2 composite (2.3 Vol.-%) shows a higher tensile modulus with an improvement by 10.5% towards 4.4% in case of C8-iPP/TiO_2 composite (2.3 Vol.-%). It can be explained as follows: firstly, the crystallinity of iPP in C8-iPP/SiO_2 composite (2.3 Vol.-%) is by 6% higher than that one in C8-iPP/TiO_2 composite (2.3 Vol.-%); secondly, the degree of hydrophobicity of C8-TiO_2 particles is higher than that one of C8-SiO_2 particles (75.6% vs. 56.2%), indicating a higher degree of covering on C8-TiO_2 particle surface. The higher the surface covering, the stronger the plasticizing

effect of particles.

As shown in Figure 4.4.1b, the C8-iPP/TiO_2 composite (2.3 Vol.-%) exhibits slightly increased tensile strength compared to C8-iPP/SiO_2 composite (2.3 Vol.-%), whereas the C0-iPP/TiO_2 composite (2.3 Vol.-%) shows a much higher tensile strength than the C0-iPP/SiO_2 composite (2.3 Vol.-%). In general, dispersed particles in polymer composites should act in two ways: (1) serving as binding agent in order to modify the morphological structure of polymer matrix; (2) acting as stress concentrators under imposed force [136]. Since the interfacial adhesion between iPP and C0-TiO_2 particles is weaker than that between iPP and C0-SiO_2 particles, the higher tensile strength of C0-iPP/TiO_2 composite (2.3 Vol.-%) can be attributed to a stronger stress concentration effect of C0-TiO_2 particles. The C8-iPP/TiO_2 composite (2.3 Vol.-%) reveals a higher tensile strength than the C8-iPP/SiO_2 composite (2.3 Vol.-%) due to stronger interfacial interactions (higher degree of covering).

It was reported that lower crystallinity and smaller spherulites of matrix would lead to higher fracture toughness of a polymer composite [137, 138]. Figure 4.4.2 shows the fracture toughness of neat iPP and discussed composites. It can be seen that the C0-iPP/TiO_2 composite (2.3 Vol.-%) exhibits much lower fracture toughness than the C0-iPP/SiO_2 composite (2.3 Vol.-%) despite lower crystallinity of iPP matrix in composite. This result can be mainly attributed to poor dispersion quality of C0-TiO_2 particles in iPP matrix leading to easier propagation of cracks. On the other hand, the C8-iPP/TiO_2 composite (2.3 Vol.-%) shows a higher K_{IC} value than the C8-iPP/SiO_2 composite (2.3 Vol.-%), correlating well with the lower crystallinity of iPP matrix and the higher interfacial interactions in C8-iPP/TiO_2 composite (2.3 Vol.-%).

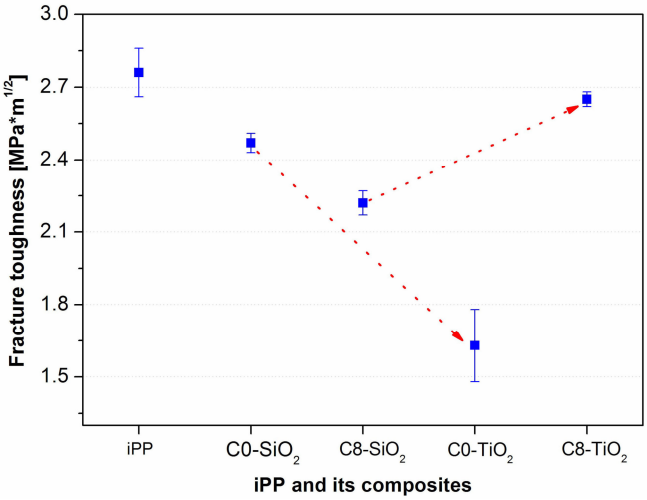

Figure 4.4.2: Influence of particle type on fracture toughness of iPP composites containing 2.3 Vol.-% of particles (TiO_2 vs. SiO_2).

4.5 TPE(PBT-PTMG)/TiO_2 composites filled with different TiO_2 particles

In this chapter, a thermoplastic elastomer (TPE) based on PBT-PTMG was used as polymer matrix. Three types of TiO_2 particles were used as fillers for TPE(PBT-PTMG) as shown in Table 3.2 in chapter 3.1.2, i.e. unmodified TiO_2 (21 nm, Aeroxide P25) particles with OH-groups on particle surface, surface modified TiO_2 (300 nm, Kronos 2310) and TiO_2 (15 nm, Hombitec RM 300) particles with Al_2O_3, SiO_2 and polyalcohol. All three particles show a hydrophilic surface nature. The TPE(PBT-PTMG)/TiO_2 composites were prepared by direct melt blending in a twin-screw extruder via masterbatch technique as introduced in chapter 3. The properties of produced TPE(PBT-PTMG)/TiO_2 composites were characterized and discussed.

4.5.1 TPE(PBT-PTMG)/TiO_2 (21 nm) composites

4.5.1.1 Dispersion of TiO_2 (21 nm) particles in TPE(PBT-PTMG)

After compounding process, the dispersion quality of TiO_2 (21 nm) particles in TPE(PBT-PTMG) was examined by using SEM and µCT methods. Figure 4.5.1a shows the SEM micrographs of unmodified TiO_2-filled TPE(PBT-PTMG) composites with different particle contents. Figure 4.5.1b represents a close-up view of particle-matrix interphase.

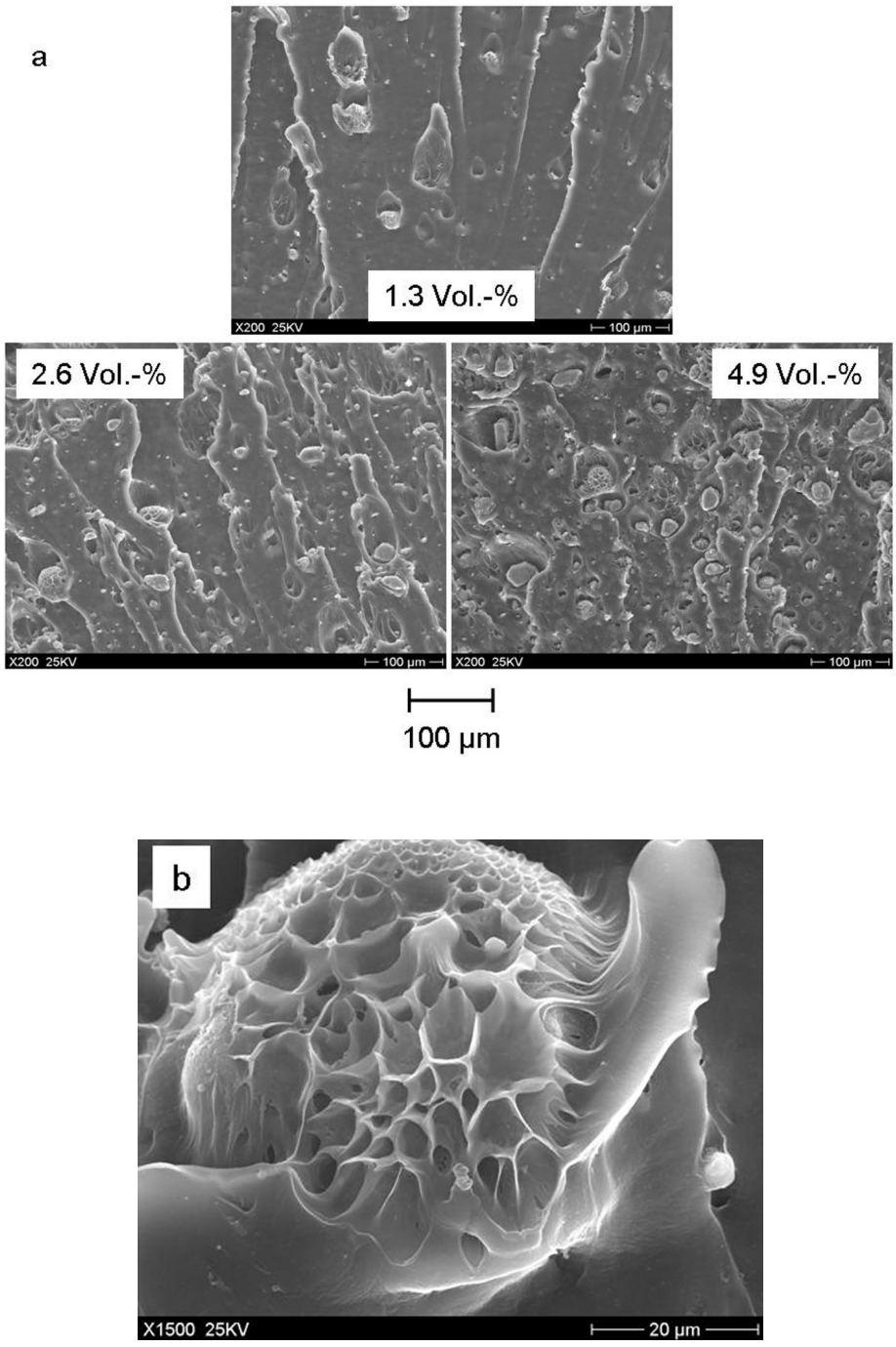

Figure 4.5.1: SEM micrographs of TPE(PBT-PTMG)/TiO_2 (21 nm) composites with different particle contents: (a) dispersion of TiO_2 (21 nm) particles in TPE(PBT-PTMG), (b) a close view of particle-matrix interface.

Like in iPP/C0-TiO_2 composites, the TiO_2 (21 nm) nanoparticles result in strong agglomeration/flocculation in the TPE(PBT-PTMG) matrix and the degree of agglomeration increases with increasing particle content. As already discussed in chapter 4.4 and 4.5, the reason for such a strong agglomeration is the strong interfacial interactions among the nanoparticles itself due to formation of hydrogen bonds, especially related to the high surface tension of this unmodified TiO_2 nanoparticles. The existence of such large agglomerates in the TPE(PBT-PTMG)/TiO_2 (21 nm) composites indicates again that the shear force during extrusion process was not effective enough to break them down. From Figure 4.5.1b, it is interesting to see that a “fibrillar” structure of TPE(PBT-PTMG) is formed at the matrix-TiO_2 interface, indicating an excellent interfacial adhesion. It is mentioned in chapter 1 that TiO_2 molecules can form chemical bonding with carboxylate groups in PBT-PTMG copolymer. The good interfacial adhesion at interface is a proof for such chemical bonds.

The µCT images characterize the spacial dispersion of TiO_2 (21 nm) particles in the TPE(PBT-PTMG) matrix as shown in Figure 4.5.2. It should be noted that the maximum resolution of used µ-CT apparatus in this work is 500 nm. The particles, which are much smaller than 500 nm, can not be detected by µ-CT examination. From µCT images, the TiO_2 (21 nm) agglomerates are well distributed in TPE(PBT-PTMG) matrix although they result in a high degree of agglomeration.

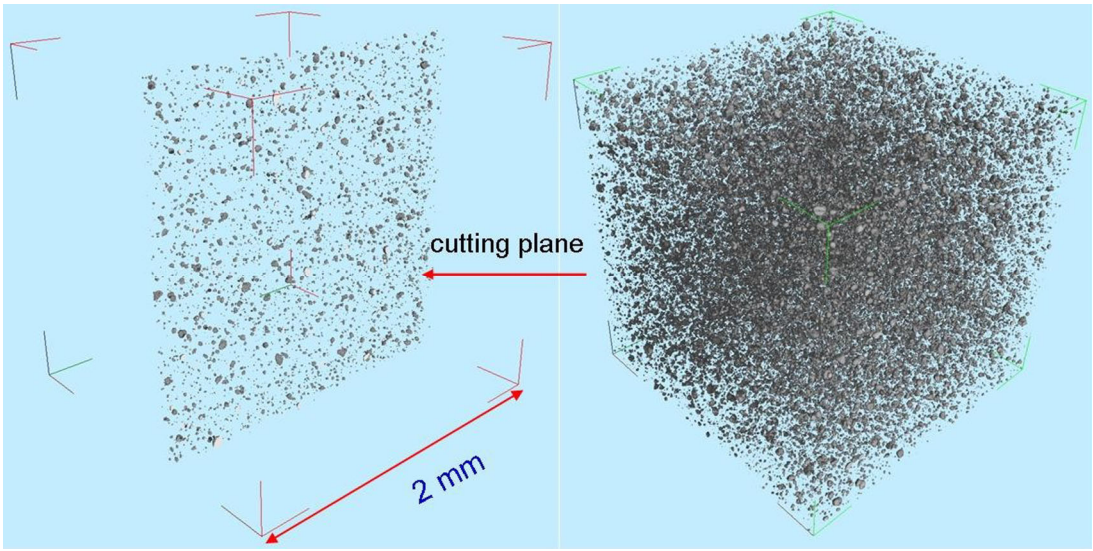

Figure 4.5.2: µCT image of TPE(PBT-PTMG)/TiO_2 (21 nm) composite containing 1.3 Vol.-% of particles.

4.5.1.2 Thermal properties of TPE(PBT-PTMG)/TiO_2 (21 nm) composites

DMTA results

Dynamic mechanical measurements can provide a good impression of the phase behaviour of copolymers. Figure 4.5.3 shows the DMTA results of pure PBT-PTMG copolymer and its composites filled with TiO_2 (21 nm) particles.

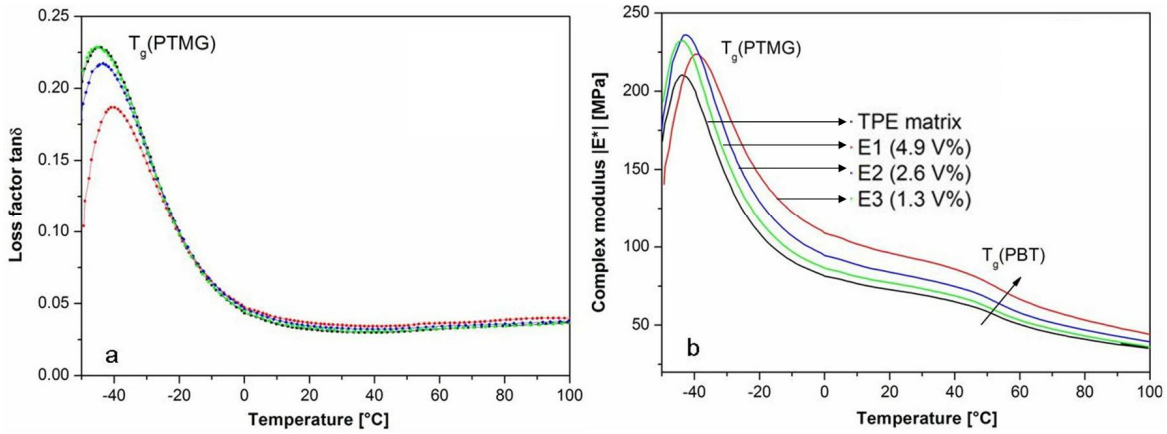

Figure 4.5.3: Dynamical mechanical properties of TPE(PBT-PTMG) and its composites: (a) loss factor tanδ as a function of temperature and (b) complex modulus as a function of temperature.

From the Figure 4.5.3a, the tanδ curves of all materials exhibit only one significant glass transition peak at about -45 °C (T_g^1) which is mainly attributed to the soft PTMG block. Compared to PTMG homopolymer which has a T_g at about -50 °C [35], the single intensive glass transition peak in the PBT-PTMG block copolymer shifts clearly to higher temperature at -45.5°C. This increase of T_g (PTMG) in the copolymer is caused by chemical linkage to the rigid PBT block and partial block mixing with amorphous PBT segment. The glass transition peak of amorphous PBT in tanδ-temperature curve is not clearly observed. This indicates that either a non-crystalline PBT phase does not exist or the weight fraction of amorphous PBT is very low in this PBT-PTMG copolymer. The reason is that in polymeric materials containing semicrystalline components, during glass transition only the amorphous part undergoes the segmental motion, whereas the crystalline region remains as solid until its melting temperature is reached [130]. Generally, it is accepted that the amorphous PBT phase is mixed with PTMG phase building a homogenous amorphous phase [37]. As shown in Figure 4.5.3b, two fast drop steps in complex

modulus |E*| are observed as indicated in diagram. The first sharp drop in $|E^*|$ occurs after the glass transition of PTMG segment. The second fast drop in $|E^*|$ occurs at about 50 °C at which the glass transition of amorphous PBT segment should take place [139].

By incorporation of TiO_2 (21 nm) particles, the glass transition peaks of PTMG segments in composites shift to higher temperatures compared to neat TPE(PBT-PTMG) matrix. This implies that the TiO_2 (21 nm) particles in TPE(PBT-PTMG) restrict the mobility of macromolecular chains of matrix due to chemical and physical interactions. In addition, increasing particle content leads to increased glass transition temperature of PTMG segment and the complex modulus of TPE(PBT-PTMG)/TiO_2 (21 nm) composites. At 4.9 Vol.-% of TiO_2 (21 nm) particles, the improvements in glass transition temperature (PTMG) and storage modulus are 3.0 °C and 32.7%, respectively. The storage modulus E' and the glass transition temperature of PTMG segments in TPE(PBT-PTMG)/TiO_2 (21 nm) composites are listed in Table 4.11.

TGA results

The thermal stability of TPE(PBT-PTMG) and TPE(PBT-PTMG)/TiO_2 (21 nm) composites was examined by using TGA. The results are shown in Figure 4.5.4.

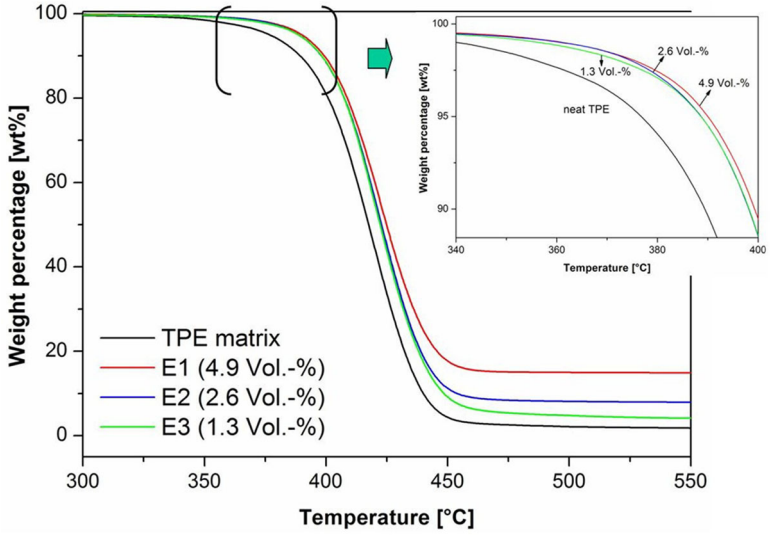

Figure 4.5.4: TGA curves of TPE(PBT-PTMG) and TPE(PBT-PTMG)/TiO_2 (21 nm) composites.

It is evident that neat TPE(PBT-PTMG) exhibits a one-step-degradation process in the temperature range of 330-460 °C. The weight loss of pure TPE(PBT-PTMG) below 330 °C is lower than 0.05% corresponding to loss of remaining humidity in matrix. The main decomposition corresponding to matrix back-bone degradation starts at about 330 °C with an accelerated rate. The average thermal degradation temperature (T_{onset}) of neat TPE(PBT-PTMG) which characterizes the thermal stability of the polymer is 395.8 °C. The incorporation of TiO_2 (21 nm) particles obviously reinforces the thermal stability of TPE(PBT-PTMG) with a maximum improvement by 5.3 °C at 4.9 Vol.-% of particles. This improvement can be attributed to the chemical interactions between TPE(PBT-PTMG) and TiO_2 (21 nm) particles. The T_{onset} of TPE(PBT-PTMG) composites increases with increasing particle content. All T_{onset} values of neat TPE(PBT-PTMG) and its composites are given in Table 4.11.

Table 4.11: Results of DMTA and TGA tests of neat TPE(PBT-PTMG) and TPE(PBT-PTMG)/TiO_2 (21 nm) composites

Samples	Particle content [Vol.-%]	T_g (PTMG) [°C]	E' (23°C) [MPa]	T_{onset} [°C]
neat TPE(PBT-PTMG)	0	-45.5	72.7	395.8
E3	1.3	-44.7	75.9	397.9
E2	2.6	-44.5	83.5	398.7
E1	4.9	-42.5	96.5	401.1

DSC results

The thermal and crystalline properties of neat TPE(PBT-PTMG) and its composites were examined by using DSC method. The results are shown in Figure 4.5.5.

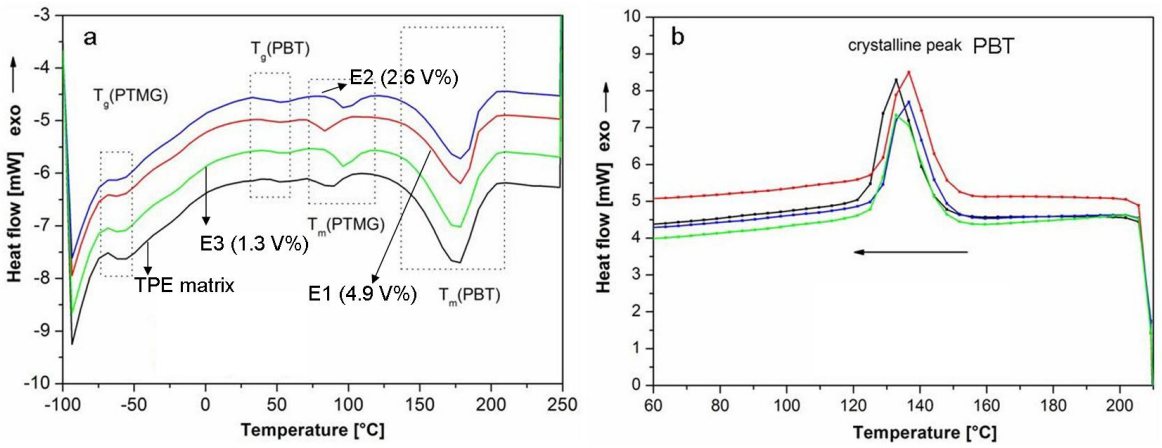

Figure 4.5.5: DSC curves of TPE(PBT-PTMG) matrix and TPE(PBT-PTMG)/TiO_2 (21 nm) composites: (a) melting curves and (b) crystalline curves.

As shown in Figure 4.5.5a, two glass transition peaks and two melting peaks in the DSC curves of all materials are observed, in which the glass transition peak at about -55 °C (T_g^1) and the melting peak close to 90 °C (T_m^1) are related to PTMG segment,

while the small glass transition peak around 50 °C (T_g^2) and the melting peak at about 175 °C (T_m^2) are attributed to PBT segment. The observation of two glass transition peaks reflects the amorphous PBT and PTMG phases which differ in chemical composition. Compared to pure TPE(PBT-PTMG) matrix, the TPE(PBT-PTMG)/TiO_2 (21 nm) composites reveal slightly increased glass transition temperatures of PTMG and PBT segments as given in Table 4.12.

Table 4.12: DSC results of TPE(PBT-PTMG) and its TPE(PBT-PTMG)/TiO_2 (21 nm) composites

Samples	T_g^1 (DSC) [°C]	T_g^2 (DSC) [°C]	T_m^1 (DSC) [°C]	T_m^2 (DSC) [°C]	ΔH(PBT) [J/g]
neat TPE(PBT-PTMG)	-57.2	52.0	86.5	174.6	23.2
E3 (1.3 V%)	-56.4	52.9	97.2	178.0	20.5
E2 (2.6 V%)	-55.5	52.6	95.6	177.2	19.7
E1 (4.9 V%)	-56.9	52.4	83.4	175.9	20.2

Note: [1] for PTMG block, [2] for PBT block.

From Table 4.12, the incorporation of TiO_2 (21 nm) particles in TPE(PBT-PTMG) shows a strong effect on the melting temperature of PTMG segment. At 1.3 Vol.-% of particles, the melting temperature T_m (PTMG) increases from 86.5 °C of matrix to 97.2 °C of composite. The improvement is about 11 °C. Higher particle loading leads to a decrease of T_m (PTMG). At 4.9 Vol.-% of TiO_2 (21 nm) particles, the melting temperature of PTMG segment in composite is 3.1 °C lower than that of pure matrix. Unlike strongly affected T_m (PTMG) in composites, the melting temperature of PBT segment in TPE(PBT-PTMG)/TiO_2 (21 nm) composites only slightly increases compared to pure TPE(PBT-PTMG) matrix, but it shows similar decreasing tendency

with increasing particle content. The maximum improvement in T_m (PBT) is 3.4 °C at 1.3 Vol.-% of TiO_2 (21 nm) particles. The increase of melting temperatures of PTMG and PBT segments in composites should be attributed to the chemical linkage between matrix and TiO_2 (21 nm) particles as introduced in chapter 1, which actually increases the chain length and the molecular weight of PBT-PTMG block as well as the degree of crosslinkage between polymer chains. On the other hand, the addition of TiO_2 particles in composites leads to decreased weight fractions of PTMG and PBT segments in composition. This should be the reason for decreasing T_m (PTMG) and T_m (PBT) in composites with increasing particle content [139]. Furthermore, it is thought that the TiO_2 (21 nm) particles are mainly located in the mixed PTMG/PBT amorphous phase which is rich in PTMG segment, i.e. the chemical interactions between TPE(PBT-PTMG) matrix and TiO_2 (21 nm) particles mostly exist in the mixed PBT/PTMG amorphous phase as shown in Figure 4.5.6. Therefore, the increasing effect of particles on melting temperature is more pronounced for PTMG segment than for PBT segment.

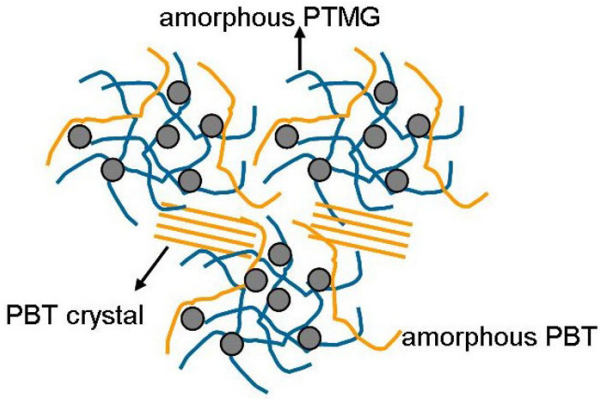

Figure 4.5.6: The location of TiO_2 (21 nm) particles in the PBT-PTMG matrix.

As another result of these chemical cross-links between matrix and TiO_2 particles, the

crystallinity of hard PBT segment is clearly decreased in TPE(PBT-PTMG)/TiO_2 composites due to decreased chemical regularity of PBT macromolecular chains, indicated by decreased crystalline enthalpy (ΔH-PBT) as shown in Table 4.12. The crystalline peaks of PBT segment in composites shift to higher temperature compared to neat TPE(PBT-PTMG) matrix, indicating a heterogeneous nucleation effect of TiO_2 particles.

4.5.1.3 Mechanical properties of TPE(PBT-PTMG)/TiO_2 (21 nm) composites

Tensile properties

The tensile properties of TPE(PBT-PTMG)/TiO_2 (21 nm) composites were examined by using tensile test. Figure 4.5.7 shows the typical stress-strain curves of neat TPE(PBT-PTMG) and TPE(PBT-PTMG)/C0-TiO_2 composites.

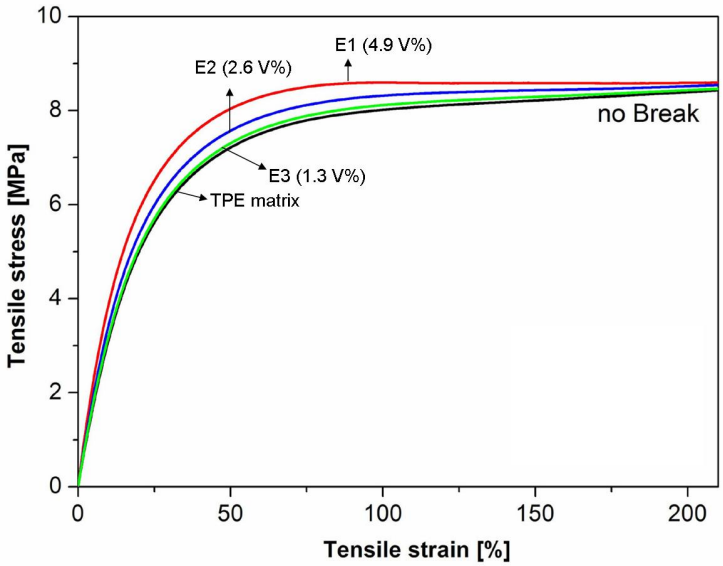

Figure 4.5.7: Stress-strain curves of TPE(PBT-PTMG) and TPE(PBT-PTMG)/TiO_2 (21 nm) composites.

It can be seen that the tensile stress increases continuously with increasing tensile

strain in S-S curves. No yield point is observed. From the S-S curves, the incorporation of TiO_2 (21 nm) particles reinforces the TPE(PBT-PTMG) matrix and the composites remain ductile. Figure 4.5.8 shows the tensile results in detail.

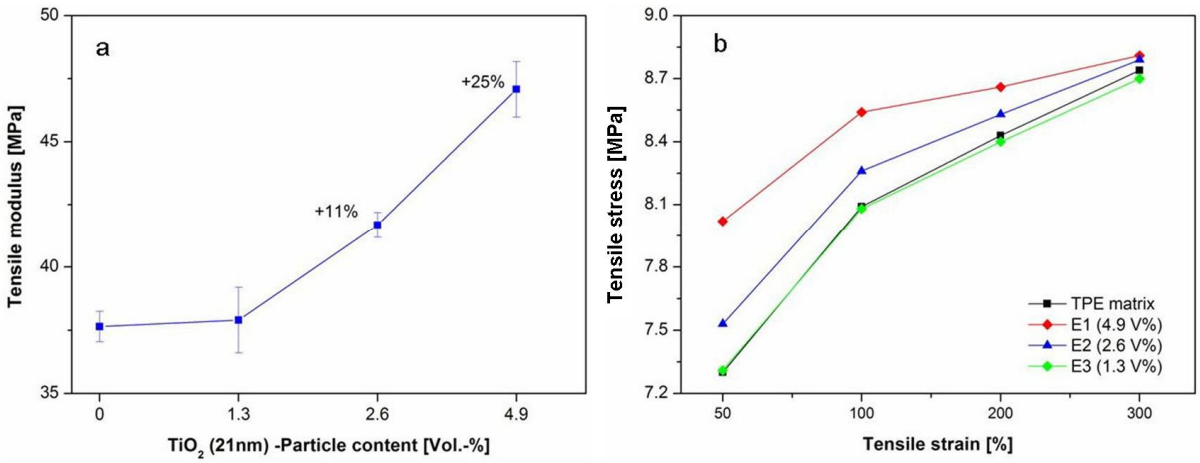

Figure 4.5.8: Tensile properties of neat TPE(PBT-PTMG) and TPE(PBT-PTMG)/TiO_2 (21 nm) composites: (a) tensile modulus as a function of particle content, and (b) tensile stress as a function of tensile strain.

As shown in Figure 4.5.8a, the tensile modulus significantly increases with increasing particle content. At 1.3 Vol.-% of TiO_2 particles, the tensile modulus is comparable high with neat TPE(PBT-PTMG) matrix due to low particle loading. At 2.6- and 4.9 Vol.-% of particles, the improvements in tensile modulus attain 11% and 25%, respectively. The diagram in Figure 4.5.8b shows the tensile stress of all samples as a function of tensile strain. Evidently, the tensile stress of all samples increases with increasing tensile strain in the studied strain range. The incorporation of TiO_2 particles into TPE(PBT-PTMG) improves the tensile stress of composites at higher particle contents due to strong stress transfer from matrix to particles. At 1.3 Vol.-% of TiO_2 (21 nm) particles, an improvement in tensile stress does not occur efficiently due to reduced stress transfer from TPE(PBT-PTMG) matrix to particles. Furthermore,

increasing tensile strain leads to decreased improvements in tensile stress of composites. At 50% tensile strain, the composites E1 and E2 exhibit 10% and 3% improvements, respectively. At 100% tensile strain, the improvements are by 6% for E1 and 2% for E2. At 300% tensile strain, the values of tensile stress of composites and neat TPE(PBT-PTMG) matrix are comparable to each other. In addition, all composites show high flexibility in the applied strain range whereas their tensile modulus and stress are obviously improved. All samples kept undamaged up to 300% tensile strain.

Creep behaviour

The tensile creep behaviour of TPE(PBT-PTMG) and TPE(PBT-PTMG)/TiO_2 (21 nm) composites as a function of time at different testing temperatures is shown in Figure 4.5.9. It can be clearly seen that the creep compliance of all samples increases with increasing temperature due to increasing polymer chain mobility and the creep compliance also increases with increasing testing time.

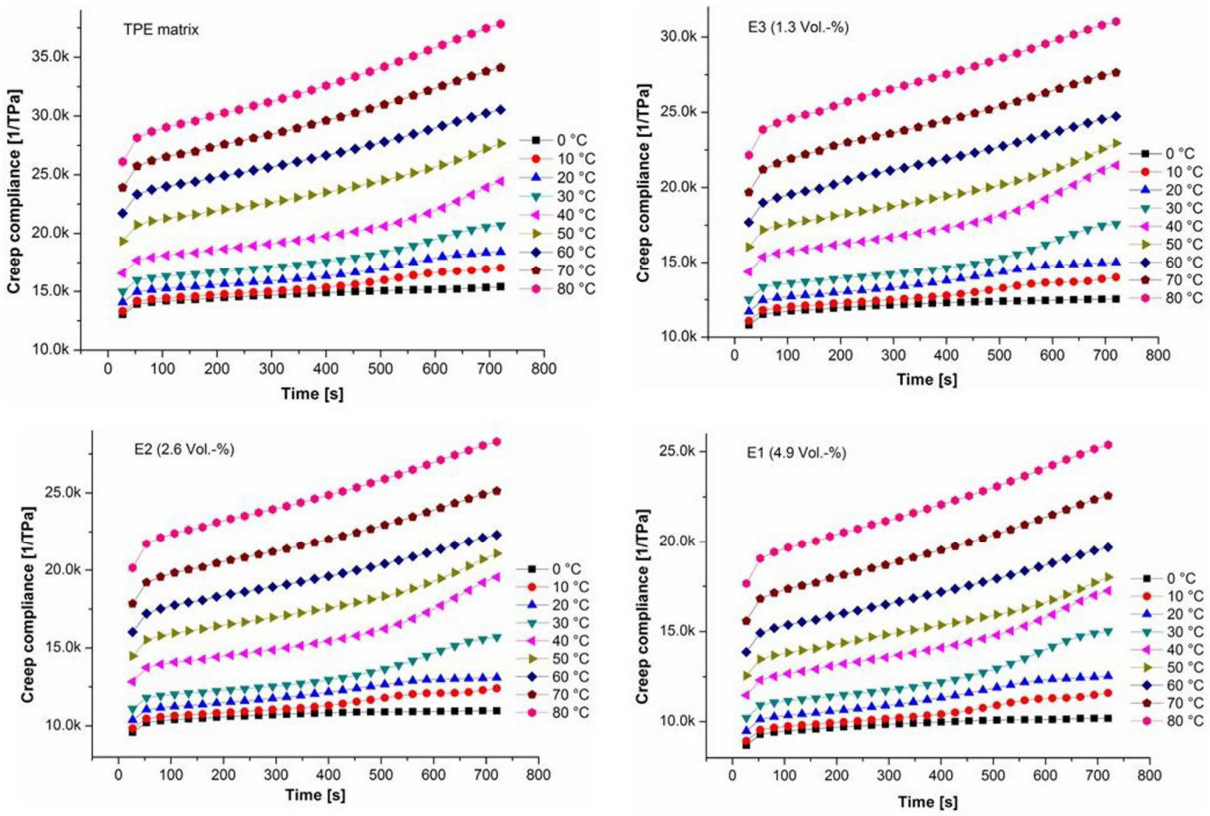

Figure 4.5.9: Effect of temperature on the tensile creep behaviour of neat TPE(PBT-PTMG) and TPE(PBT-PTMG)/TiO_2 (21 nm) composites.

Figure 4.5.10a and 4.5.10b show the creep compliance of TPE(PBT-PTMG) samples as a function of testing temperature (T = 30 °C) and time (t = 500 s), respectively. Evidently, at the same testing time or testing temperature, the creep compliance of TPE(PBT-PTMG) decreases significantly by incorporation of TiO_2 (21 nm) particles. The reason is that the mobility of TPE(PBT-PTMG) chains in composites is strongly reduced due to chemical and physical interactions between matrix and TiO_2 (21 nm) particles. In addition, increasing particle content leads to decreased creep compliance as expected, indicating an increased creep resistance of composites. This increased creep resistance of composites with increasing particle content can be attributed to increased interfacial interactions between TPE(PBT-PTMG) matrix and TiO_2 (21 nm) particles which restrict the mobility of polymer chains.

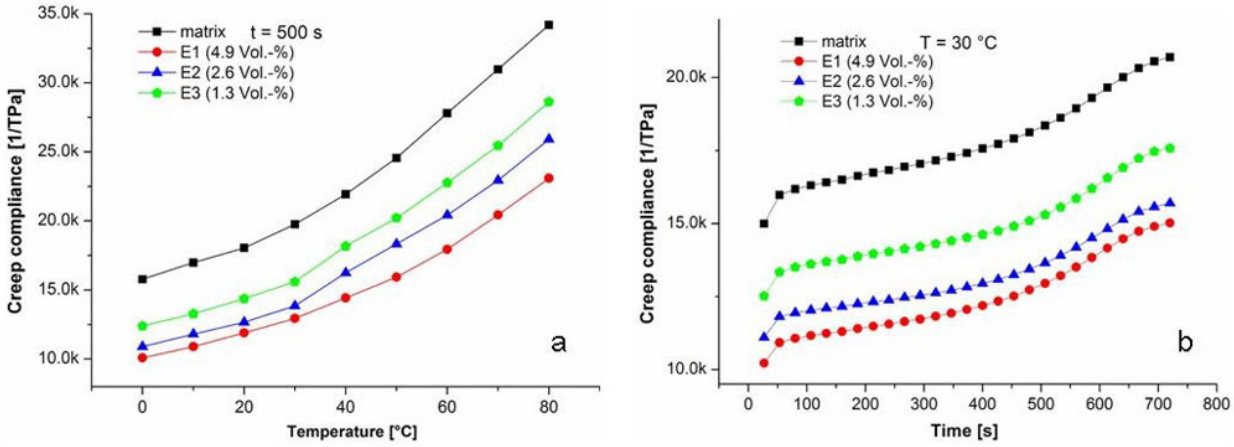

Figure 4.5.10: Creep compliance of TPE(PBT-PTMG) samples as a function of: (a) temperature and (b) time.

In order to obtain the long-term creep behaviour of TPE(PBT-PTMG) samples, the time-temperature superposition (TTS) principle has been applied. The generated master curves, i.e. the logarithm creep compliance as a function of logarithm time, are

displayed in Figure 4.5.11 at a reference temperature by 30 °C. It is evident that the TPE(PBT-PTMG)/TiO_2 (21 nm) composites reveal significant decreased creep compliance, i.e. increased resistance to tensile creep compared to neat TPE(PBT-PTMG) within the whole time range (10^{-2} to 10^{8} s). Additionally, the creep resistance of composites increases with increasing particle content.

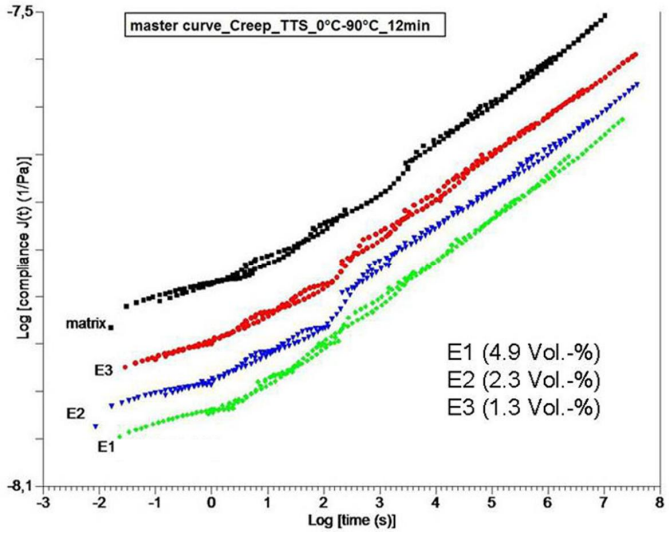

Figure 4.5.11: Master curves of creep compliance for TPE(PBT-PTMG) and TPE(PBT-PTMG)/TiO_2 (21 nm) composites.

According to [102], the Arrhenius equation can better describe the relationship between temperature and shift factor of TPE(PBT-PTMG) samples, because TPE(PBT-PTMG) is a block copolymer containing a semi-crystalline PBT segment. Figure 4.5.12 shows the shift factors $\log\alpha_T$, obtained by shifting the creep curves to the reference curve by 30 °C, as a function of 1/T for all TPE(PBT-PTMG) samples. It appears that the shift data can be well described by the Arrhenius equation. The activation energy values of all samples calculated from the slope of the regression curves in Figure 4.5.12 are listed in Table 4.13. It can be seen that the activation energy of TPE(PBT-PTMG) is increased by incorporation of TiO_2 (21 nm) particles,

and the value also increases with increasing particle content. The larger the activation energy, the greater is the influence of temperature on shift factor [140].

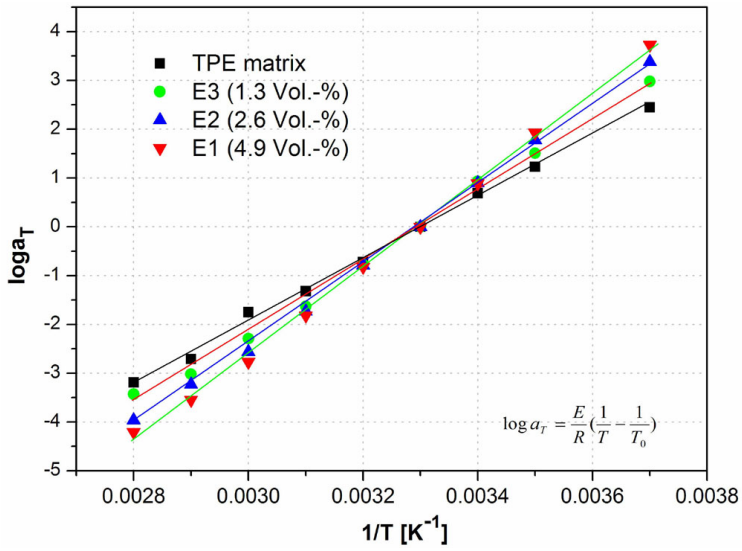

Figure 4.5.12: Dependency of shift factor on temperature for TPE(PBT-PTMG) and TPE(PBT-PTMG)/TiO_2 (21 nm) composites.

Table 4.13: Activation energy of TPE(PBT-PTMG) and TPE(PBT-PTMG)/TiO_2 (21 nm) composites

Samples	Activation energy E [kJ/mol]
neat TPE(PBT-PTMG)	157.5
E3 (1.3 Vol.-%)	166.2
E2 (2.6 Vol.-%)	170.2
E1 (4.9 Vol.-%)	174.0

4.5.1.4 Weathering behaviour of TPE(PBT-PTMG)/TiO_2 (21 nm) composites

As mentioned in chapter 4.3.4, untreated TiO_2 particles in polymer composites can absorb UV light causing photochemical degradation of polymer matrix. Figure 4.5.13 shows the tensile bars of neat TPE(PBT-PTMG) and TPE(PBT-PTMG)/TiO_2 (21 nm) composites with 2.6- and 4.9 Vol.-% of particles. The samples were exposured in air for 30 days before the pictures were taken. Compared to neat TPE(PBT-PTMG), it is evident that both composite samples show clear weathering cracks in tensile samples, indicating a significant photodegradation effect of untreated TiO_2 (21 nm) particles. Compared to iPP in chapter 4.3.4, TPE(PBT-PTMG) has a lower resistance against photodegradation induced by TiO_2 (21 nm).

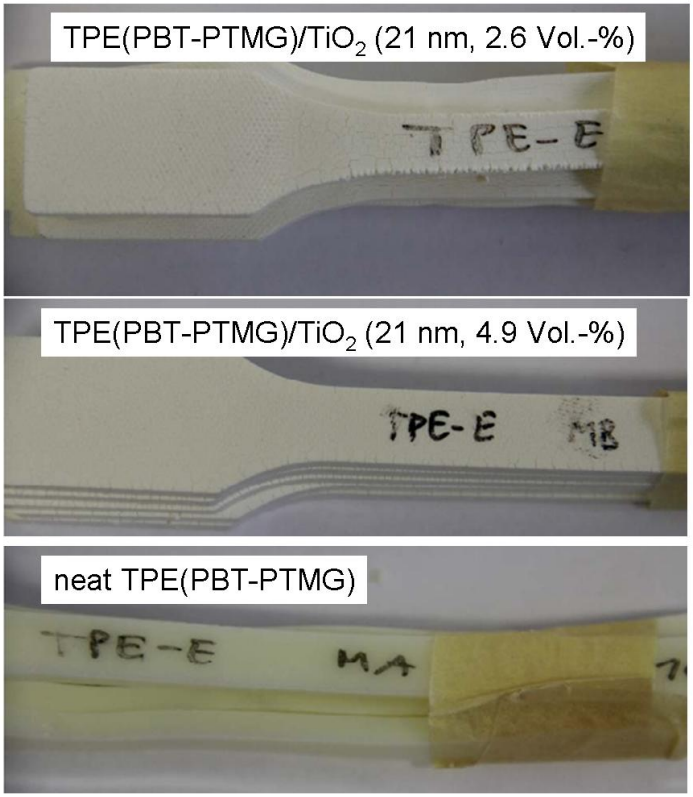

Figure 4.5.13: Tensile samples of TPE(PBT-PTMG) and TPE(PBT-PTMG)/TiO2 (21 nm) composites containing 2.6- and 4.9 Vol.-% of TiO2 (21 nm) particles for weathering assessment.

4.5.1.5 Conclusion

The untreated TiO_2 (21 nm) nanoparticles are compounded into PBT-PTMG-based TPE by using direct melt blending. The thermal and mechanical properties of TPE(PBT-PTMG)/TiO_2 (21 nm) composites were characterized and discussed. According to SEM and µCT examination, the TiO_2 (21 nm) particles result in a high degree of agglomeration. The agglomerates are well distributed in the TPE(PBT-PTMG) matrix despite high degree of agglomeration. It is also showed that the matrix-particle adhesion is very good due to strong chemical interactions. The results of thermal characterization show that the incorporation of TiO_2 (21 nm) particles into TPE(PBT-PTMG) overall increases the thermal properties such as thermal stability of matrix, glass transition temperatures and melting temperatures of both PBT and PTMG segments. The storage modulus of TPE(PBT-PTMG)/TiO_2 (21 nm) composites is also increased compared to neat TPE(PBT-PTMG). As a result of chelating effects between TPE(PBT-PTMG) matrix and TiO_2 (21 nm) particles, the crystallinity of PBT segment is decreased in composites. In addition, the incorporation of TiO_2 (21 nm) particles shows an evident reinforcing effect on the tensile properties of TPE(PBT-PTMG). The tensile modulus and strength of TPE(PBT-PTMG) are significantly improved, especially at higher particle contents. Furthermore, the TPE(PBT-PTMG)/TiO_2 (21 nm) composites show significantly higher creep resistance compared to neat TPE(PBT-PTMG), and it increases evidently with increasing particle content. Unlike iPP/TiO_2 (21 nm) composites, the TPE(PBT-PTMG)/TiO_2 (21 nm) composites show significant weathering/chalking behaviour caused by untreated TiO_2 (21 nm) nanoparticles.

4.5.2 TPE(PBT-PTMG)/TiO_2 (300 nm) composites

As introduced in chapter 4.3.4, untreated TiO_2 particles can act as photocatalyst in polymers and lead to photochemical degradation of polymer matrix as shown in chapter 4.5.1.4. Surface treatment can prevent the photodegradation induced by free radicals at polymer/TiO_2 interface. In general, surface treatments of TiO_2 particles usually consist of Al_2O_3, SiO_2, ZrO_2 and/or other substrates deposited in monomolecular layers by vapor-phase calcination. For example, an Al_2O_3 coating can enhance the dispersibility and flocculation resistance of TiO_2 particles. A SiO_2 treatment can suppress the photocatalytical reaction on TiO_2 surface, enhancing the durability of outdoor applications of polymer/TiO_2 composites [144, 145].

According to supplier's information, the TiO_2 (300 nm, Kronos 2310) particles were pre-treated with Al_2O_3 and SiO_2 before supplying. The particles also show hydrophilic surface nature. In this chapter, two TPE(PBT-PTMG)/TiO_2 (300 nm) composites containing 2.6- and 3.8 Vol.-% of particles were prepared. The thermal and tensile properties of produced composites were characterized and discussed.

4.5.2.1 Dispersion of TiO_2 (300 nm) particles in TPE(PBT-PTMG)

The dispersion of TiO_2 (300 nm) particles in TPE(PBT-PTMG) was examined by using SEM and µCT methods. Figure 4.5.14 shows the SEM micrograph of TPE(PBT-PTMG)/TiO_2 (300 nm) composite filled with 2.6 Vol.-% of particles. Unlike TiO_2 (21 nm) nanoparticles which exhibit a very high degree of agglomeration in TPE(PBT-PTMG), the TiO_2 (300 nm) particles are well dispersed in the TPE(PBT-PTMG) matrix. No large agglomerates are observed. The composite with 3.8 Vol.-% of TiO_2 (300 nm) particles shows similar SEM micrographs as the composite with lower particle loading. In addition, the TiO_2 (300 nm) particles are well

embedded in the TPE(PBT-PTMG) matrix indicating a very good phase adhesion between TPE(PBT-PTMG) matrix and particles. The very good dispersion quality of TiO_2 (300 nm) particles can be attributed to surface treatment and low interfacial interactions between particles themselves.

Figure 4.5.15 shows the spacial dispersion of TiO_2 (300 nm) particles in TPE(PBT-PTMG) matrix obtained by µCT analysis. It is observed again that the TiO_2 (300 nm) particles are very homogenously distributed in the TPE(PBT-PTMG) matrix and most particles are dispersed to be primary ones in the TPE(PBT-PTMG).

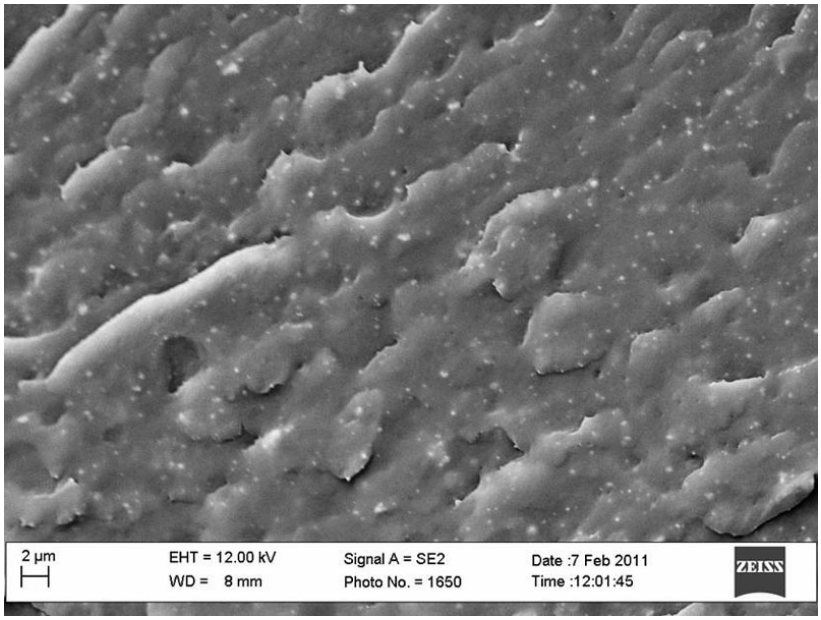

Figure 4.5.14: SEM micrograph of TiO_2 (300 nm)-filled TPE(PBT-PTMG) composite (2.6 Vol.-%).

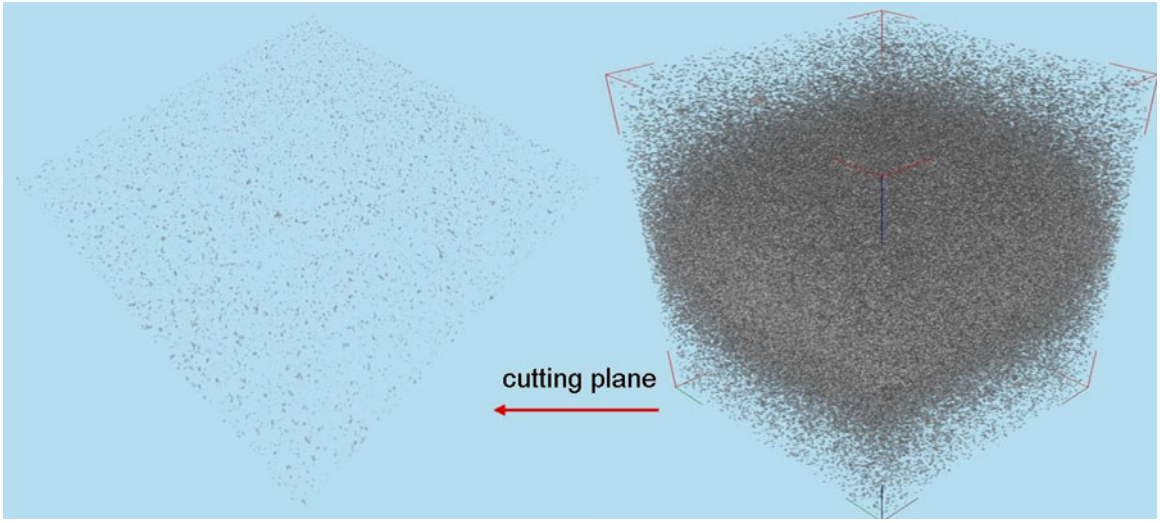

Figure 4.5.15: Three dimensional dispersion of TiO_2 (300 nm) particles in TPE(PBT-PTMG) matrix (2.6 Vol.-%) obtained by µCT analysis.

4.5.2.2 Thermal properties of TPE(PBT-PTMG)/TiO_2 (300 nm) composites

TGA results

The thermal properties of TPE(PBT-PTMG)/TiO_2 (300 nm) composites were characterized by TGA. Figure 4.5.16 shows the weight loss curves of neat TPE(PBT-PTMG) and composites filled with 2.6- and 3.8 Vol.-% of TiO_2 (300 nm) particles.

It can be seen that the incorporation of TiO_2 (300 nm) particles into TPE(PBT-PTMG) only slightly increases the thermal stability of matrix. The onset decomposition temperature of composite containing 2.6 Vol.-% of TiO_2 (300 nm) particles is only 0.7 °C higher than that one of neat TPE(PBT-PTMG). At 3.8 Vol.-% of particles, the improvement in T_{onset} is by 1.1 °C. The T_{onset} and the temperatures at 20- and 50 wt% weight loss for TPE(PBT-PTMG) and TPE(PBT-PTMG)/TiO_2 (300 nm) composites are listed in Table 4.14. From the TGA results, TiO_2 (300 nm) particles show no great

reinforcing effect on thermal stability of TPE(PBT-PTMG).

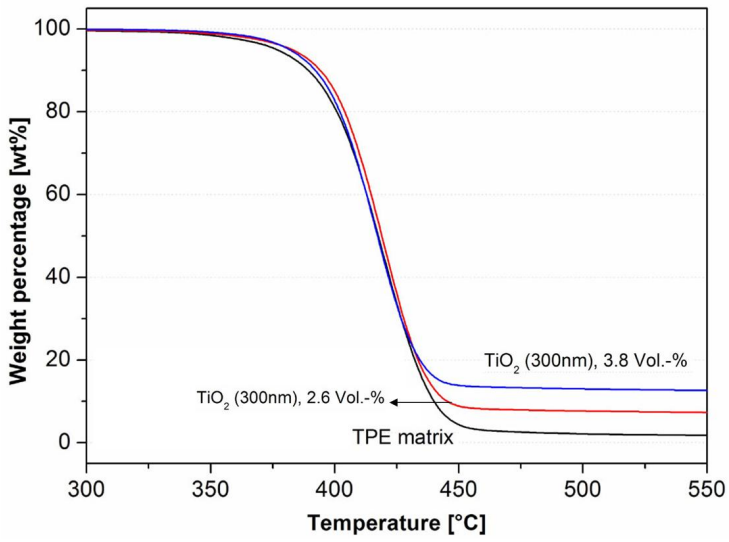

Figure 4.5.16: TGA curves of TPE(PBT-PTMG) and TPE(PBT-PTMG)/TiO_2 (300 nm) composites.

Table 4.14: TGA results of TPE(PBT-PTMG) matrix and TPE(PBT-PTMG)/TiO_2 (300 nm) composites

Samples	Particle content [Vol.-%]	T_{onset} [°C]	$T_{20\%}$ [°C]	$T_{50\%}$ [°C]
neat TPE(PBT-PTMG)	0	395.8	400.9	417.6
K2	2.6	396.5	404.1	419.0
K1	3.8	396.9	402.0	417.1

DMTA results

The dynamic-mechanical thermal behaviour of TPE(PBT-PTMG)/TiO_2 (300 nm) composites was performed by using DMTA. Figure 4.5.17 shows the curves of loss factor tanδ and complex modulus |E*| as a function of temperature for all samples.

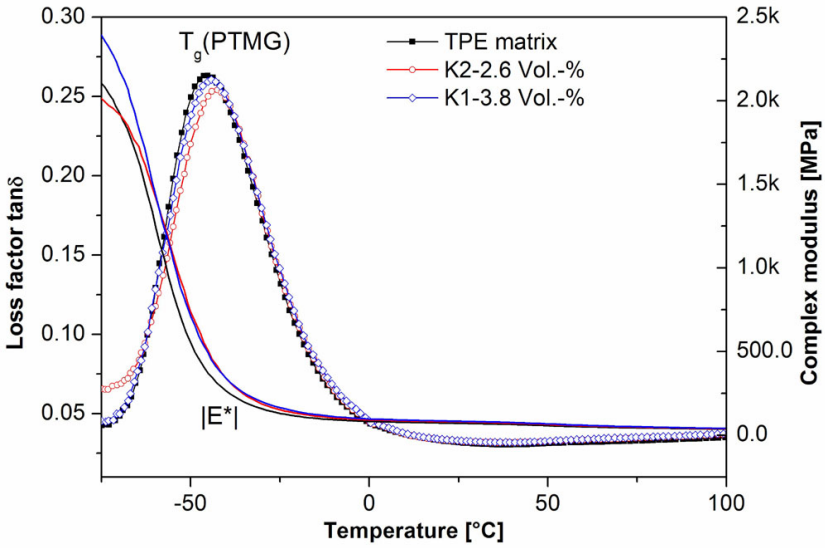

Figure 4.5.17: DMTA result of TPE(PBT-PTMG)/TiO_2 (300 nm) composites.

Similar to DMTA curves of TPE(PBT-PTMG)/TiO_2 (21 nm) composites, the curves of TPE(PBT-PTMG)/TiO_2 (300 nm) composites also show one significant glass transition peak related to PTMG segment in the tanδ-temperature diagram. Compared to neat TPE(PBT-PTMG) which exhibits a glass transition temperature of PTMG segment at -45.5 °C, the K2 composite containing 2.6 Vol.-% of TiO_2 (300 nm) particles shows an increase in T_g (PTMG) by 3.1 °C (-42.4 °C). However, higher loading content does not lead to further improvement in T_g (PTMG) in DMTA characterization. The K1 composite containing 3.8 Vol.-% of particles shows a T_g (PTMG) at -44.2 °C. Higher particle loading results in higher complex modulus of composite. In addition, both TPE(PBT-PTMG)/TiO_2 (300 nm) composites reveal significant improvements in storage modulus E' compared to neat TPE(PBT-PTMG), and the storage modulus increases with increasing particle content. At 23 °C, the storage modulus is 80.3 MPa for K2 composite and 84.1 MPa for K1 composite as listed in Table 4.15, i.e. the improvements in storage modulus are by 10.5% and 15.7%, respectively.

Table 4.15: DMTA results of TPE(PBT-PTMG)/TiO_2 (300 nm) composites

Samples	T_g (PTMG) [°C]	Storage modulus [MPa]
neat TPE(PBT-PTMG)	-45.5	72.7
K2 (2.6 Vol.-%)	-42.4	80.3
K1 (3.8 Vol.-%)	-44.2	84.1

DSC results

The thermal and crystalline behaviour of TPE(PBT-PTMG)/TiO_2 (300 nm) composites were investigated by using DSC analysis. The melting and crystalline curves of samples are shown in Figure 4.5.18. The obtained data are listed in Table 4.16.

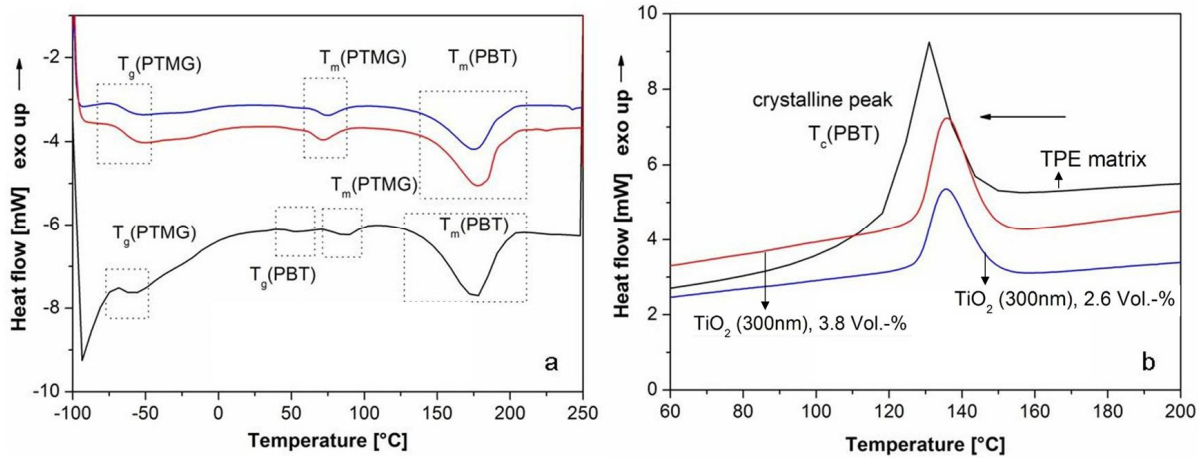

Figure 4.5.18: DSC diagrams of TPE(PBT-PTMG)/TiO_2 (300 nm) composites: (a) melting curves and (b) crystalline curves.

Table 4.16: DSC results of TPE(PBT-PTMG) matrix and TPE(PBT-PTMG)/TiO_2 (300 nm) composites

Samples	T_g (PTMG) [°C]	T_g (PBT) [°C]	T_m (PTMG) [°C]	T_m (PBT) [°C]	T_c (PBT) [°C]	ΔH (PBT) [J/g]
neat TPE(PBT-PTMG)	-57.2	52.0	86.5	174.6	132.0	23.2
K2 (2.6 V%)	-55.2	-	77.1	176.5	135.7	17.1
K1 (3.8 V%)	-54.1	-	72.5	179.6	135.8	16.4

From the DSC diagrams and the results in Table 4.16, it is evident that incorporation of TiO_2 (300 nm) particles into TPE(PBT-PTMG) increases the glass transition temperature of PTMG segments in composites due to reduced mobility of polymer chains. The respective improvements in T_g (PTMG) are by 2.0 °C for K2 composite and 3.1 °C for K1 composite. The glass transition peaks for PBT segment in both composites are not observed in this DSC analysis. In addition, the melting temperatures of PTMG segments in composites are decreased compared to neat TPE(PBT-PTMG) and the T_m (PTMG) decreases also at higher particle loading. By contrast, the melting temperature of PBT segments in composites increases after particle loading. Higher particle content leads to a higher T_m (PBT). The improvement is by 5.0 °C at 3.8 Vol.-% of TiO_2 (300 nm) particles. This improvement in T_m (PBT) in composites can be attributed to chemical interfacial interactions between TPE(PBT-PTMG) and TiO_2 (300 nm) particles. Furthermore, both TPE(PBT-PTMG)/TiO_2 (300 nm) composites show increased crystalline temperatures T_c (PBT) up to 3.8 °C at 3.8 Vol.-%, indicating a heterogeneous nucleation effect of TiO_2 (300 nm) particles. Additionally, the crystallinity of PBT segments decreases in both composites indicated by decreased crystalline enthalpy.

4.5.2.3 Mechanical properties of TPE(PBT-PTMG)/TiO_2 (300 nm) composites

Tensile properties

The tensile properties of TPE(PBT-PTMG)/TiO_2 (300 nm) composites were characterized. Figure 4.5.19 shows the stress-strain curves of neat TPE(PBT-PTMG) and TPE(PBT-PTMG)/TiO_2 (300 nm) composites filled with 3.8- and 2.6 Vol.-% of TiO_2 (300 nm) particles. It is evident that the K1 and K2 composites exhibit similar ductile behaviour as neat TPE(PBT-PTMG) and the tensile stress of TPE(PBT-PTMG) is clearly improved after loading of TiO_2 (300 nm) particles.

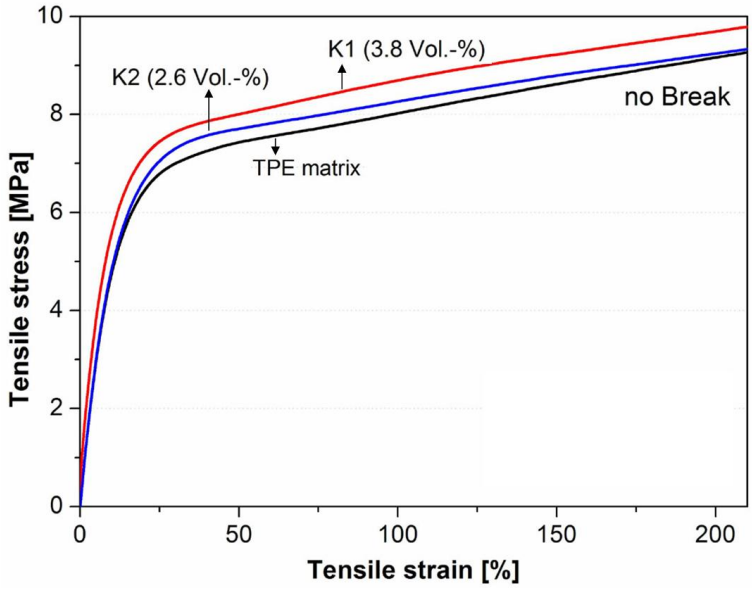

Figure 4.5.19: Tensile stress-strain curves of neat TPE(PBT-PTMG) and TPE(PBT-PTMG)/TiO_2 (300 nm) composites.

The detailed tensile modulus and tensile stress of all samples are shown in Figure 4.5.20. From Figure 4.5.20a, the TPE(PBT-PTMG)/TiO_2 (300 nm) composites show a remarkable improvement in tensile modulus. The improvements are by 89% for K2 composite and 103% for K1 composite. The increased tensile modulus of composites should be attributed to addition of rigid TiO_2 (300 nm) particles themselves.

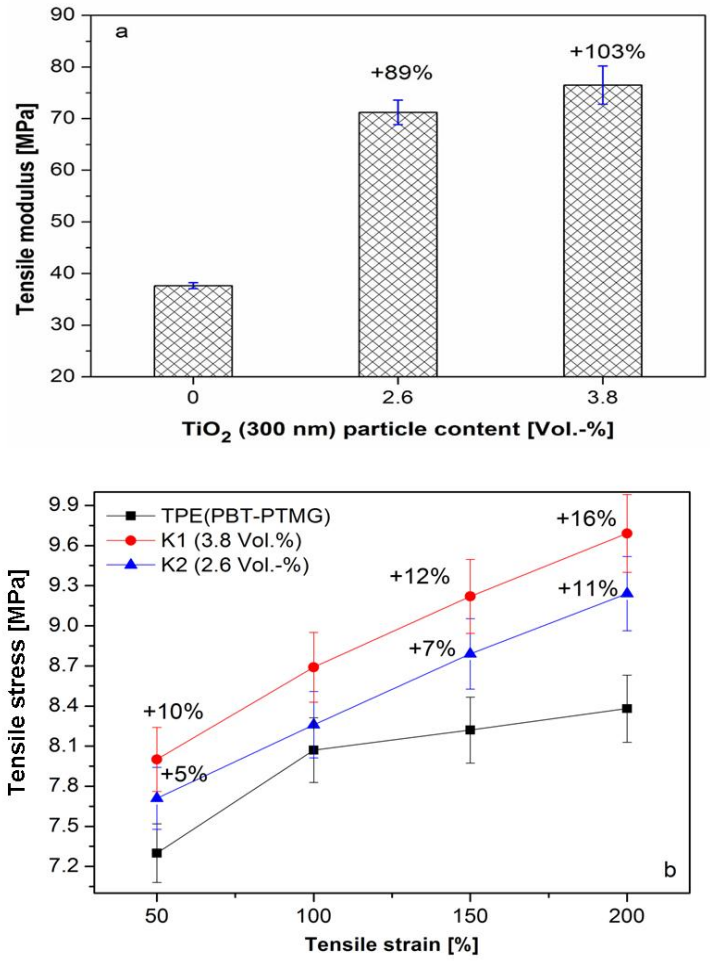

Figure 4.5.20: Tensile properties of TPE(PBT-PTMG)/TiO_2 (300 nm) composites: (a) tensile modulus as a function of particle content, and (b) tensile stress as a function of tensile strain.

Figure 4.5.20b shows the values of tensile stress of TPE(PBT-PTMG) and TPE(PBT-PTMG)/TiO_2 (300 nm) composites at different tensile strain up to 200%.

Compared to neat TPE(PBT-PTMG), the K1 and K2 composites result in significant improvements in tensile stress in the given tensile strain range. At 50% tensile strain, the improvements in tensile stress are by 5% for K2 and 10% for K1 composite. At 200% tensile strain, the improvements are extended to 11% for K2 and 16% for K1 composite. Obviously, the tensile modulus and tensile stress of TPE(PBT-PTMG)/TiO_2 (300 nm) composites are clearly increased by higher particle loading. On one hand, these remarkable improvements in tensile properties of TPE(PBT-PTMG)/TiO_2 (300 nm) composites should be attributed to strong interfacial interactions between TPE(PBT-PTMG) matrix and TiO_2 particles due to formation of “chemical bonds”. On the other hand, the high dispersion quality of TiO_2 (300 nm) particles also plays an important role in improving the mechanical properties of TPE(PBT-PTMG)/TiO_2 (300 nm) composites.

4.5.2.4 Weathering behaviour of TPE(PBT-PTMG)/TiO_2 (300 nm) composites

Figure 4.5.21 shows the samples of neat TPE(PBT-PTMG) and TPE(PBT-PTMG)/TiO_2 (300 nm, 3.8 Vol.-%) composite after exposure in air for 30 days. It is evident that the TPE(PBT-PTMG)/TiO_2 (300 nm) composite shows no photodegradation cracks in the samples. Compared to TPE(PBT-PTMG)/TiO_2 (21 nm) composites which show strong photodegradation in air, the TPE(PBT-PTMG)/TiO_2 (300 nm) composites exhibit increased weathering resistance due to surface treatment of TiO_2 (300 nm) particles.

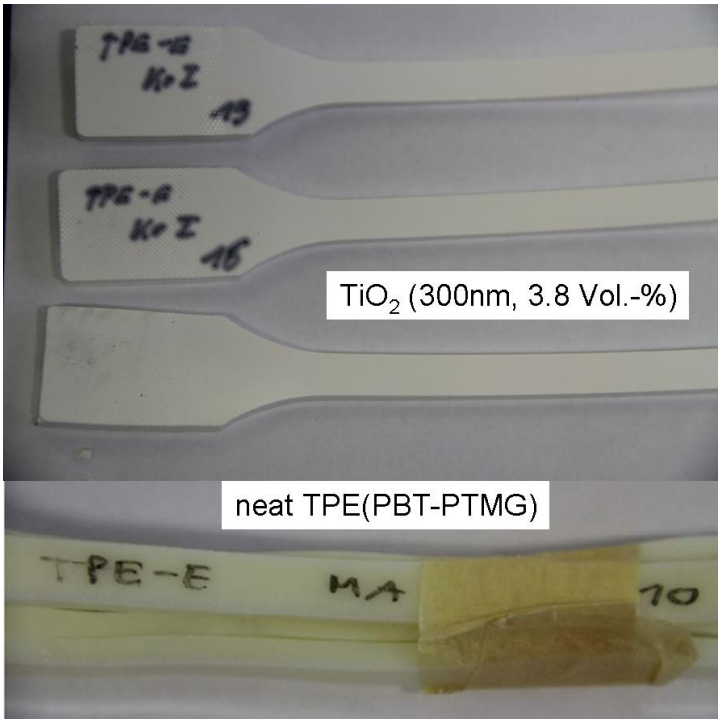

Figure 4.5.21: Neat TPE(PBT-PTMG) and TPE(PBT-PTMG)/TiO_2 (300 nm, 3.8 Vol.-%) composite samples for weathering assessment.

4.5.2.5 Conclusion

TiO_2 (300 nm) was surface pre-treated with Al_2O_3 and SiO_2 before supplying. Two TPE(PBT-PTMG)/TiO_2 (300 nm) composites containing 2.6- and 3.8 Vol.-% of TiO_2 (300 nm) particles were produced by direct melt blending in a twin-screw extruder. The thermal and mechanical properties of produced composites were characterized and discussed. The SEM and µCT micrographs show that the TiO_2 (300 nm) particles are very homogenously dispersed in TPE(PBT-PTMG) matrix as primary ones. The TGA result shows that the TPE(PBT-PTMG)/TiO_2 (300 nm) composites exhibit only slightly increased thermal stability compared to neat TPE(PBT-PTMG). However, the incorporation of TiO_2 (300 nm) particles into TPE(PBT-PTMG) significantly improves the storage modulus of both composites with improvements by 10.5% and 15.7%, respectively. In addition, the tensile properties of TPE(PBT-PTMG)/TiO_2 (300 nm) composites are remarkably increased after loading with TiO_2 (300 nm) particles. The improvements in tensile modulus of both composites are by 89% and 103%, respectively. Higher particle loading leads to higher storage moduli, tensile moduli and tensile stress of TPE(PBT-PTMG)/TiO_2 (300 nm) composites at the same time. According to DSC analysis, the crystallinity of PBT segments in composites is decreased but the crystalline temperature T_c (PBT) is increased due to nucleation effect of TiO_2 (300 nm) particles. Furthermore, the TPE(PBT-PTMG)/TiO_2 (300 nm) composites do not show photodegradation behaviour due to surface treatment of TiO_2 (300 nm) particles.

4.5.3 TPE(PBT-PTMG)/TiO_2 (15 nm) composites

According to supplier's information, the TiO_2 (15 nm, Hombitec RM 300) particles are hydrophilic and surface-modified with Al_2O_3 and polyalcohol so that the nanoparticles should be well dispersed in polymer matrix. Three TPE(PBT-PTMG)/TiO_2 (15 nm) composites with different particle contents were produced via masterbatch method. The dispersion quality of TiO_2 (15 nm) particles in TPE(PBT-PTMG) and the properties of produced composites were investigated and discussed.

4.5.3.1 Dispersion of TiO_2 (15 nm) nanoparticles in TPE(PBT-PTMG) matrix

The dispersion quality of TiO_2 (15 nm) particles in TPE(PBT-PTMG) were examined by using SEM. Figure 4.5.22 shows the SEM pictures of TiO_2 (15 nm) particle-filled TPE(PBT-PTMG) composite containing 2.6 Vol.-% of particles.

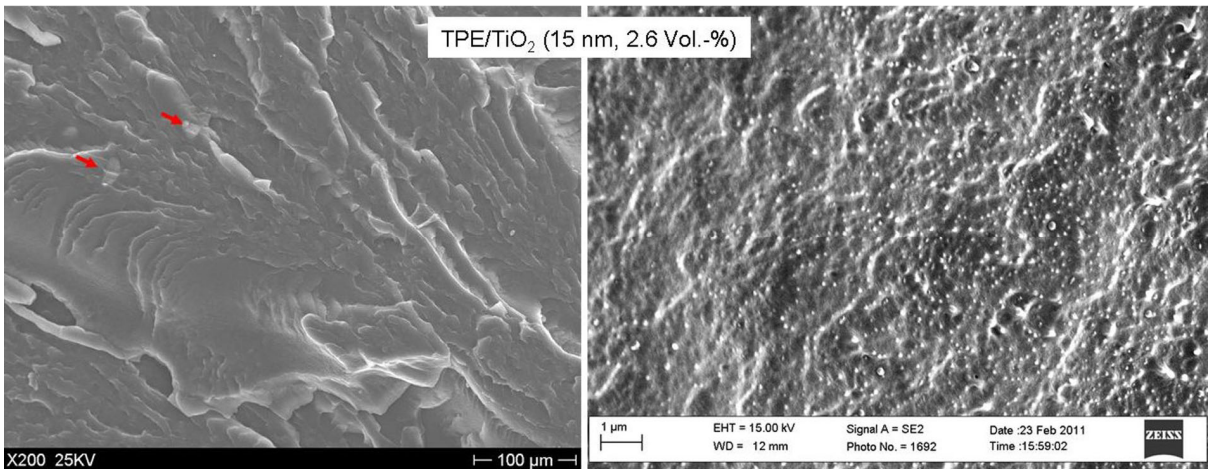

Figure 4.5.22: SEM images of TPE(PBT-PTMG)/TiO_2 (15 nm, 2.6 Vol.-%) composite. The arrows indicate large particle agglomerates in micro size up to 30 µm.

Unlike TiO_2 (21 nm) nanoparticles which show also hydrophilic surface nature and

comparable primary particle size but result in a very high degree of agglomeration, the TiO_2 (15 nm) nanoparticles are very homogenously dispersed in TPE(PBT-PTMG) within nano scale range as shown in SEM micrograph. Only a few large agglomerates are observed in TPE(PBT-PTMG)/TiO_2 (15 nm) composites. In analogy to TiO_2 (300 nm) particles, this homogenous dispersion of TiO_2 (15 nm) particles should be attributed to the surface modification before compounding process. Figure 4.5.23 shows SEM micrographs of TPE(PBT-PTMG)/TiO_2 (15 nm) composites containing 3.8- and 4.9 Vol.-% of nanoparticles. Combined with Figure 4.5.22, it is evident that the number of large agglomerates increases with increasing particle content. According to SEM examination, the adhesion between TPE(PBT-PTMG) matrix and TiO_2 (15 nm) nanoparticles is very good.

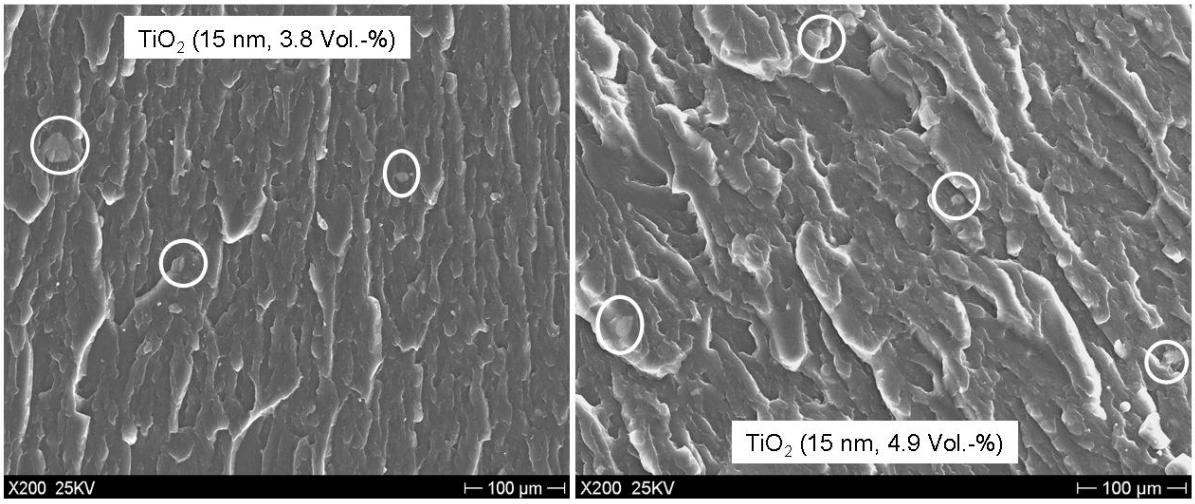

Figure 4.5.23: Increasing particle agglomeration with increasing particle content in TPE(PBT-PTMG)/TiO_2 (15 nm) composites. The white circles in pictures show large particle agglomerates.

4.5.3.2 Thermal properties of TPE(PBT-PTMG)/TiO_2 (15 nm) composites

TGA results

The thermal stability of TPE(PBT-PTMG)/TiO_2 (15 nm) composites was examined by using TGA. Figure 4.5.24 shows the weight loss curves of neat TPE(PBT-PTMG) and TPE(PBT-PTMG)/TiO_2 (15 nm) composites. The degradation temperature and the temperatures at 20- and 50 wt% weight loss of all samples are summarized in Table 4.17.

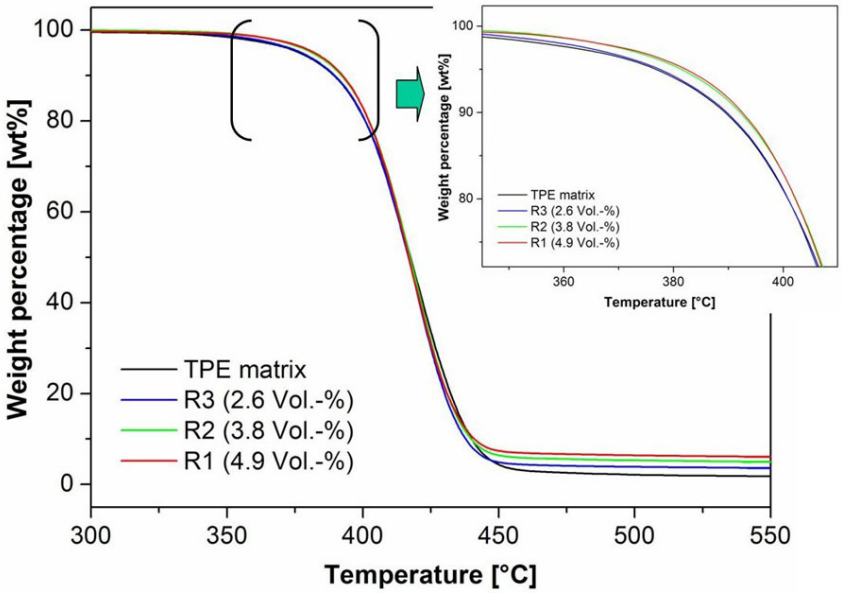

Figure 4.5.24: TGA results of TPE(PBT-PTMG)/TiO_2 (15 nm) composites.

It can be seen that the thermal stability of TPE(PBT-PTMG)/TiO_2 (15 nm) composites is not significantly increased compared to neat TPE(PBT-PTMG), because the onset decomposition temperatures of composites are comparable to that one of neat matrix. In addition, increasing particle content in TPE(PBT-PTMG) composites does not lead to significant increasing thermal stability. This result is in analogy to the TGA result of TPE(PBT-PTMG)/TiO_2 (300 nm) composites.

Table 4.17: TGA results of neat TPE(PBT-PTMG) and TPE(PBT-PTMG)/TiO_2 (15 nm) composites

Samples	T_{onset} [°C]	$T_{20\%}$ [°C]	$T_{50\%}$ [°C]
neat TPE(PBT-PTMG)	395.8	400.9	417.6
R1 (4.9 Vol.-%)	396.8	402.2	416.9
R2 (3.8 Vol.-%)	396.1	402.3	417.3
R3 (2.6 Vol.-%)	396.2	400.8	416.7

DSC results

The thermal and crystalline behaviour of TPE(PBT-PTMG)/TiO_2 (15 nm) composites were characterized by using DSC analysis. The melting and crystalline curves of all samples are shown in Figure 4.5.25. The data obtained are listed in Table 4.18.

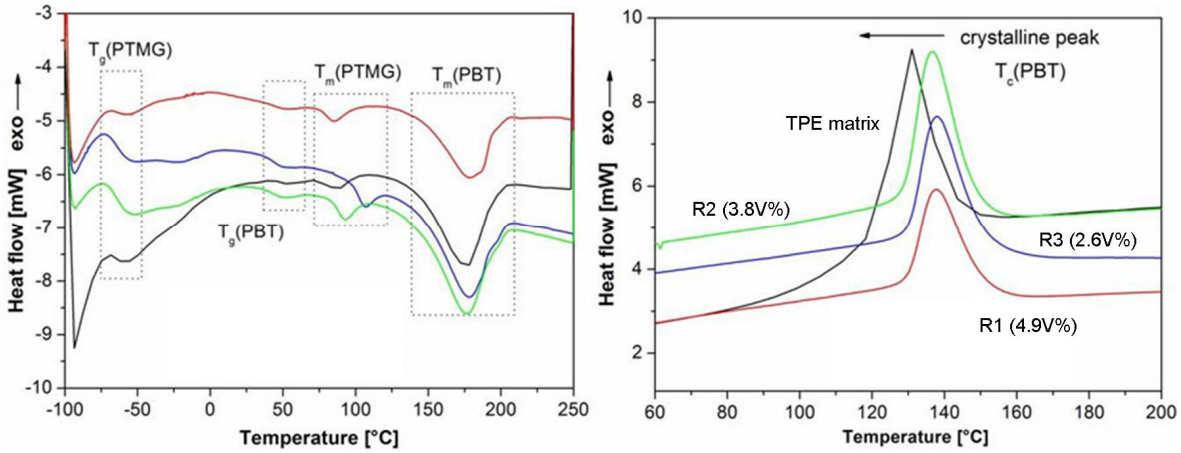

Figure 4.5.25: DSC results of TPE(PBT-PTMG)/TiO_2 (15 nm) composites: (left) melting process, and (right) crystalline process.

Table 4.18: DSC results of neat TPE(PBT-PTMG) and TPE(PBT-PTMG)/TiO_2 (15 nm) composites

Samples	T_g (PTMG) [°C]	T_g (PBT) [°C]	T_m (PTMG) [°C]	T_m (PBT) [°C]	T_c (PBT) [°C]	ΔH (PBT) [J/g]
neat TPE(PBT-PTMG)	-57.2	52.0	86.5	174.6	132.0	23.2
R1 (4.9 V%)	-55.3	50.1	84.8	179.0	137.6	18.5
R2 (3.8 V%)	-54.3	49.8	92.9	177.6	136.5	20.0
R3 (2.6 V%)	-55.4	49.9	106.4	176.8	138.0	21.7

It can be seen that the glass transition temperature of PTMG segments in TPE(PBT-PTMG)/TiO_2 (15 nm) composites obviously increases after addition of TiO_2 (15 nm) nanoparticles. The maximum improvement of T_g (PTMG) is by 2.9 °C at 3.8 Vol.-% of nanoparticles. However, the glass transition temperature of PBT segments in composites is decreased up to 2.2°C at 3.8 Vol.-% of nanoparticles. The melting temperatures of PTMG and PBT segments in TPE(PBT-PTMG)/TiO_2 (15 nm) composites show a similar tendency as in TPE(PBT-PTMG)/TiO_2 (21 nm) and TPE(PBT-PTMG)/TiO_2 (300 nm) composites, i.e. with increasing particle content T_m (PTMG) decreases from 106.4 °C to 84.8 °C whereas T_m (PBT) increases from 176.8 °C to 179.0 °C. Furthermore, the crystalline temperature T_c (PBT) in composites increases obviously compared to neat TPE(PBT-PTMG) indicating a nucleation effect of TiO_2 (15 nm) nanoparticles. In addition, the degree of crystallinity of PBT segments in TPE(PBT-PTMG)/TiO_2 (15 nm) composites decreases with increasing particle content indicated by decreasing crystalline enthalpy as shown in Table 4.18.

DMTA results

The dynamic-mechanical thermal properties of TPE(PBT-PTMG)/TiO_2 (15 nm) composites were determined by using DMTA. The curves of storage modulus and loss factor tanδ as a function of temperature are shown in Figure 4.5.26. The respective values of storage modulus and the glass transition temperature of all samples are given in Table 4.19.

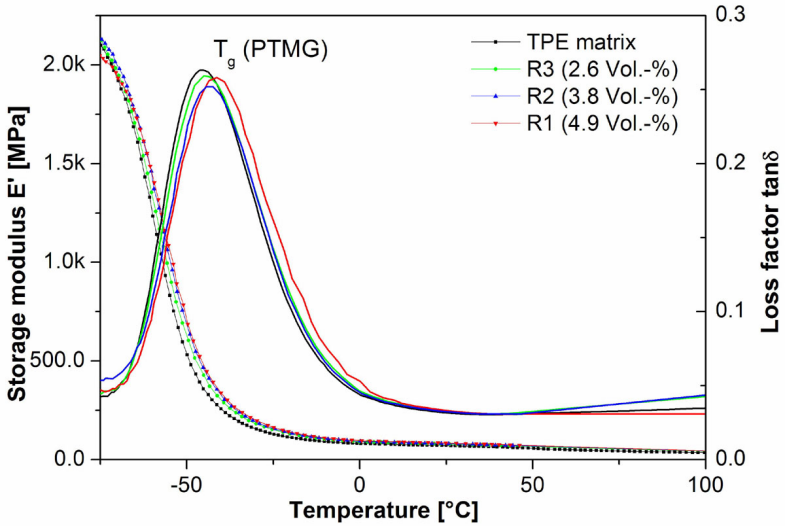

Figure 4.5.26: Storage modulus and loss factor as a function of temperature for neat TPE(PBT-PTMG) and TPE(PBT-PTMG)/TiO_2 (15 nm) composites.

Table 4.19: DMTA results of neat TPE(PBT-PTMG) and TPE(PBT-PTMG)/TiO_2 (15 nm) composites

Samples	E' at 23°C [MPa]	Improvement in E' [%]	T_g (PTMG)
TPE(PBT-PTMG)	72.7	--	-45.5
R3 (2.6 Vol.-%)	80.2	10.3%	-45.1
R2 (3.8 Vol.-%)	81.8	12.5%	-42.2
R1 (4.9 Vol.-%)	85.5	17.6%	-41.3

It is evident that all TPE(PBT-PTMG)/TiO_2 (15 nm) composites exhibit higher storage modulus in the whole temperature range than neat TPE(PBT-PTMG). The storage modulus of composites increases with increasing nanoparticle content. At 23 °C, the improvements in storage modulus are by 10.3% for R3, 12.5% for R2, and 17.6% for R1 composite as listed in Table 4.19. The tanδ curves of all samples show a clear glass transition zone of PTMG segments. The glass transition peak shifts clearly to higher temperatures after nanoparticle loading. The maximum improvement in T_g (PTMG) is by 4.2 °C at 4.9 Vol.-% of nanoparticles. The glass transition zone of PBT segments is not evident in the loss factor curves for all composites as well as neat TPE(PBT-PTMG).

4.5.3.3 Mechanical properties of TPE(PBT-PTMG)/TiO_2 (15 nm) composites

Tensile Results

The tensile properties of TPE(PBT-PTMG)/TiO_2 (15 nm) composites were performed. Figure 4.5.27 shows the stress-strain curves of neat TPE(PBT-PTMG) and TPE(PBT-PTMG)/TiO_2 (15 nm) composites. Similar to TPE(PBT-PTMG)/TiO_2 (21 nm) and TPE(PBT-PTMG)/TiO_2 (300 nm) composites, the TPE(PBT-PTMG)/TiO_2 (15 nm) composites keep ductile and are reinforced after incorporation of TiO_2 (15 nm) nanoparticles.

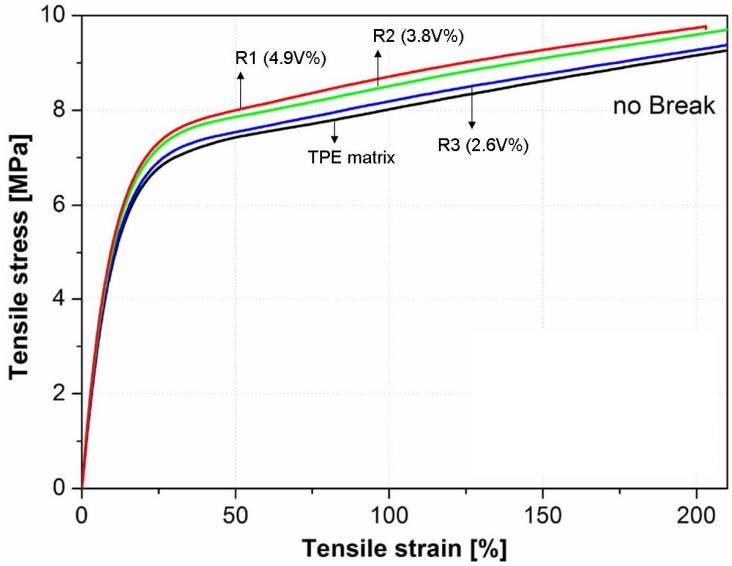

Figure 4.5.27: Stress-strain curves of TPE(PBT-PTMG) and TPE(PBT-PTMG)/TiO_2 (15 nm) composites.

The tensile moduli of all TPE(PBT-PTMG)/TiO_2 (15 nm) composites are remarkably improved compared to neat TPE(PBT-PTMG) as shown in Figure 4.5.28a. The respective improvements in tensile moduli are by 102% for R1 (4.9 Vol.-%), 96% for R2 (3.8 Vol.-%) and 90% for R3 (2.6 Vol.-%) composite. The improvements in tensile stress of TPE(PBT-PTMG)/TiO_2 (15 nm) composites are also significant. At 100% tensile strain, the improvements in tensile stress for R1, R2, and R3 are by 8%, 5%, and 1%, respectively. At 200% tensile strain, the improvements in tensile stress are achieved by 16%, 15%, and 11% for R1, R2, and R3 composites as shown in Figure 4.5.28b. In summary, increasing particle content leads to clearly increased tensile modulus and stress.

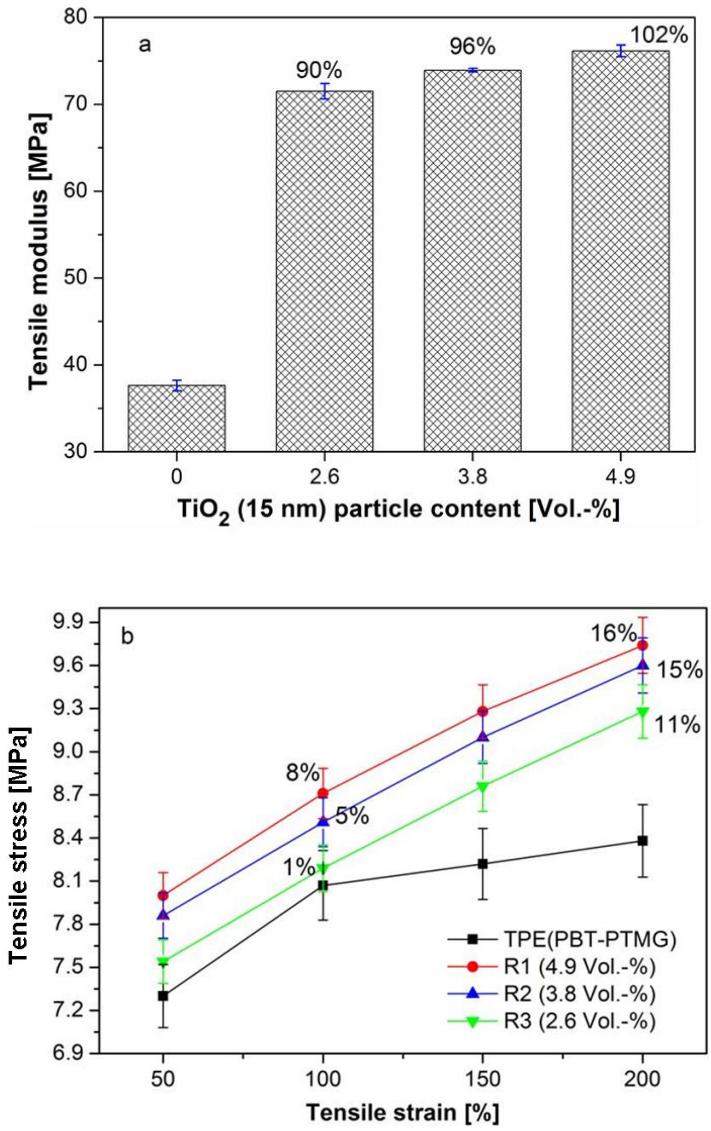

Figure 4.5.28: Tensile properties of TPE(PBT-PTMG)/TiO_2 (15 nm) composites: (a) tensile modulus as a function of TiO_2 (15 nm) particle content, and (b) tensile stress as a function of tensile strain.

4.5.3.4 Weathering of TPE(PBT-PTMG)/TiO_2 (15 nm) composites

Figure 4.5.29 shows the samples of neat TPE(PBT-PTMG) and TPE(PBT-PTMG)/TiO_2 (15 nm, 3.8 Vol.-%) composite after exposure in air for 30 days. It is evident that the TPE(PBT-PTMG)/TiO_2 (15 nm) composite shows no photodegradation cracks in the samples like TPE(PBT-PTMG)/TiO_2 (300 nm) composites. Compared to TPE(PBT-PTMG)/TiO_2 (21 nm) composites which show

strong photodegradation in air, the TPE(PBT-PTMG)/TiO_2 (15 nm) composites exhibit increased weathering resistance due to surface treatment of TiO_2 (15 nm) particles.

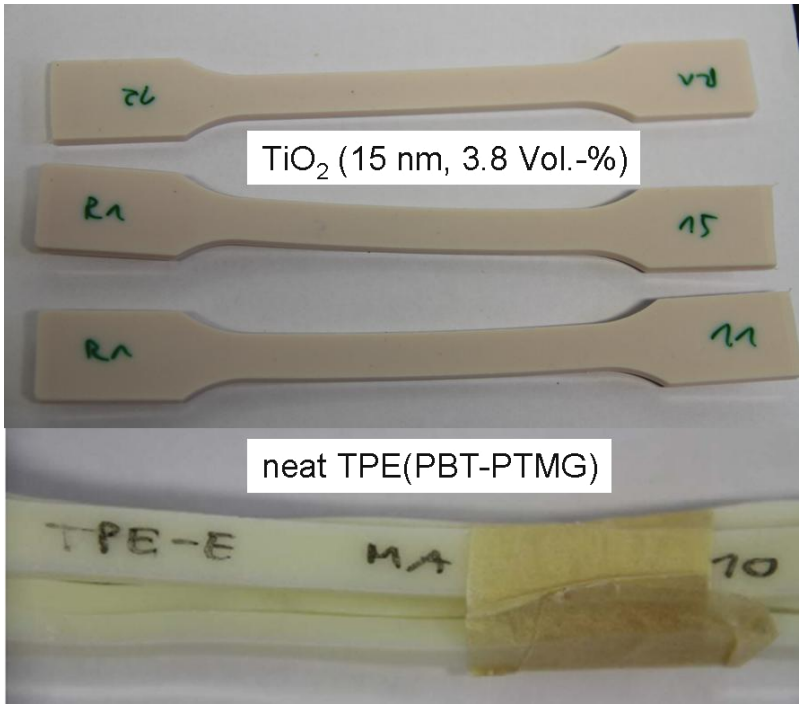

Figure 4.5.29: Neat TPE(PBT-PTMG) and TPE(PBT-PTMG)/TiO_2 (15 nm, 3.8 Vol.-%) composite samples for weathering assessment.

4.5.3.5 Conclusion

TiO_2 (15 nm) was surface pre-treated with Al_2O_3 and polyalcohol before supplying. TPE(PBT-PTMG)/TiO_2 (15 nm) composites containing 2.6-, 3.8-, and 4.9 Vol.-% of TiO_2 (15 nm) nanoparticles were prepared and characterized. The SEM examination shows that the TiO_2 (15 nm) nanoparticles are very homogenously dispersed in TPE(PBT-PTMG) matrix within nano scale range. The thermal stability of TPE(PBT-PTMG)/TiO_2 (15 nm) nanocomposites is slightly increased compared to neat TPE(PBT-PTMG) matrix. According to DSC and DMTA results, the crystallinity of PBT segments in the composites is decreased, and the glass transition temperature

of PTMG segments in TPE(PBT-PTMG)/TiO_2 (15 nm) composites is increased. Additionally, the storage modulus of composites is significantly improved. The maximum improvement is by 17.6% at 4.9 Vol.-% of nanoparticles. The tensile modulus and tensile stress of TPE(PBT-PTMG)/TiO_2 (15 nm) composites are remarkably improved in comparison with neat TPE(PBT-PTMG). Increasing particle content leads to clearly increasing tensile properties. The maximum improvements in tensile modulus and stress at 200% strain are achieved at 4.9 Vol.-% of particles by 102% and 16%, respectively. The TPE(PBT-PTMG)/TiO_2 (15 nm) composites show no photodegradation behaviour after 30 days exposure in air due to surface treatment of TiO_2 (15 nm) nanoparticles. In summary, the well dispersed TiO_2 (15 nm) nanoparticles show significant stiffening and reinforcing effects in TPE(PBT-PTMG) matrix.

4.6 Influence of different TiO_2 particles on TPE(PBT-PTMG)/TiO_2 composite properties

Depending on the type of polymer matrix, different types of particle fillers can result in different effects on the properties of polymer/filler composites. For example, Englert [147] has studied the influence of different inorganic particles on the mechanical properties of epoxy resin. The particles he used are as follows: TiO_2 (Aeroxide P25, 21 nm), TiO_2 (Hombitec RM 300, 15 nm), Al_2O_3 (Aeroxide Alu C, 13 nm) and ZrO_2 (VP Zirkonoxid PH, < 30 nm). He found that the epoxy resin composites containing different particle types show comparable tensile modulus, tensile stress, scratch resistance and hardness despite different surface pre-treatments, different sizes and chemical structures of used nanoparticles, i.e. the influence of different nanoparticles on the mechanical properties of epoxy resin is not significant.

In order to investigate the influence of different TiO_2 particles on the thermal and mechanical properties of TPE (PBT-PTMG), three types of TiO_2 particles were used as fillers in this study as shown in Table 2: unmodified TiO_2 (Aeroxide P25, 21 nm), surface modified TiO_2 (Kronos 2310, 300 nm) and TiO_2 (Hombitec RM 300, 15 nm). All three types of particles are hydrophilic and can build up chemical interactions with TPE(PBT-PTMG) matrix as introduced in chapter 1.2.3. All TPE(PBT-PTMG)/TiO_2 composites were produced by direct melt blending via masterbatch technique with the same parameters. The influence of different TiO_2 particles on thermal and mechanical properties of TPE(PBT-PTMG)/TiO_2 composites was studied and discussed in this chapter.

Table 3.2: Important characteristics of different TiO_2 particles used for TPE(PBT-PTMG)

Particle type	TiO_2 (21 nm)	TiO_2 (15 nm)	TiO_2 (300 nm)
TiO_2 content [wt%]	99.5	87	92.5
Crystal structure	rutile	rutile	Rutile
Primary particle size	21 nm	15 nm	300 nm
Density [g/cm^3]	3.8	1.47	4.0
Specific surface area [m^2/g]	50	70	17
Surface treatment	no	Al_2O_3, polyalcohol	Al_2O_3, SiO_2
Surface nature	hydrophilic	hydrophilic	Hydrophilic

4.6.1 Influence of surface pre-treatment on particle dispersion quality in TPE(PBT-PTMG)

As shown in Figure 3.2 and Figure 3.3, all three TiO_2 particles result in agglomeration in powder form before compounding into TPE(PBT-PTMG) due to interactions among particles. It is expected that the agglomerates of TiO_2 particles could be broken down by shear forces during compounding process. After compounding process, TiO_2 (300 nm) and TiO_2 (15 nm) particles show very homogenous dispersion besides only a few agglomerates in TPE(PBT-PTMG) as shown in Figure 4.5.14, 4.5.15 and 4.5.22. By contrast, TiO_2 (21 nm) particles result in a high degree of agglomeration as shown in Figure 4.5.1 and Figure 4.5.2, indicating that the shear forces during compounding process were not effective enough for this type of particles. From different dispersion quality of different TiO_2 particle types, the surface pre-treatments show a significant influence on the dispersibility of TiO_2 particles.

4.6.2 Influence of different TiO_2 particles on thermal properties of TPE(PBT-PTMG)/TiO_2 composites

According to the thermal data of TPE(PBT-PTMG)/TiO_2 composites obtained in this study, the influence of respective TiO_2 particles on thermal properties of TPE(PBT-PTMG) can be evaluated. The thermal degradation temperature T_{onset}, the storage modulus E', the glass transition temperature of PTMG segments T_g (PTMG) and the crystalline enthalpy of PBT segments ΔH (PBT) of TPE(PBT-PTMG)/TiO_2 composites containing 2.6 Vol.-% of respective TiO_2 particles are summarized in Table 4.20.

Table 4.20: Thermal properties of respective TPE(PBT-PTMG)/TiO_2 composites with 2.6 Vol.-% of particles

Samples	T_{onset} [°C] (TGA)	E' [MPa] (DMTA)	T_g (PTMG) [°C] (DMTA)	ΔH [J/g] (DSC)
TPE(PBT-PTMG)	395.8	72.7	-45.5	23.2
TPE(PBT-PTMG)/TiO_2 (21 nm)	398.7	83.5	-44.5	19.7
TPE(PBT-PTMG)/TiO_2 (300 nm)	396.5	80.3	-42.4	17.1
TPE(PBT-PTMG)/TiO_2 (15 nm)	396.2	80.2	-45.1	21.7

It is evident that the incorporation of different TiO_2 particles into TPE(PBT-PTMG) has differently affected the thermal stability of TPE(PBT-PTMG)/TiO_2 composites. The TPE(PBT-PTMG)/TiO_2 (21 nm, 2.6 Vol.-%) composite shows the highest degradation temperature and storage modulus among three composites, whereas the TPE(PBT-PTMG)/TiO_2 (300 nm, 2.6 Vol.-%) and TPE(PBT-PTMG)/TiO_2 (15 nm, 2.6

Vol.-5) composites show comparable T_{onset} and E' values to each other despite large difference in primary particle sizes. Moreover, all three composites show increased glass transition temperature of PTMG segments and decreased crystallinity of PBT segments due to chemical interactions between TiO_2 particles and TPE(PBT-PTMG) matrix compared to neat TPE(PBT-PTMG), in which TPE(PBT-PTMG)/TiO_2 (300 nm, 2.6 Vol.-%) composite shows the highest T_g (PTMG) and the lowest crystallinity of PBT segments. Based on Sumita's [106] model $\frac{W_c}{W_0} = \frac{E_c''}{E_0''} = \frac{1}{1-\varphi_e}$, the effective volume fraction φ_e of respective TiO_2 particles can be calculated according to DMTA results as given in Table 4.21. It can be seen that the calculated effective volume fractions of TiO_2 (300 nm) and TiO_2 (15 nm) particles are much larger than that one of TiO_2 (21 nm) particles at 2.6 Vol.-% due to much better particle dispersion quality in matrix.

Table 4.21: Effective volume fraction φ_e of respective TiO_2 particles in TPE(PBT-PTMG)/TiO_2 composites based on DMTA result

Particle type in TPE(PBT-PTMG)/TiO_2 composite	$\varphi_f = 2.6$ [Vol.-%]	$\varphi_f = 3.8$ [Vol.-%]
TiO_2 (21 nm)	0.102	------
TiO_2 (300 nm)	0.146	0.195
TiO_2 (15 nm)	0.169	0.198

4.6.3 Influence of different TiO_2 particles on tensile properties of TPE(PBT-PTMG)/TiO_2 composites

Figure 4.6.1 shows the tensile modulus and strength of TPE(PBT-PTMG)/TiO_2 (21 nm) and TPE(PBT-PTMG)/TiO_2 (15 nm) composites containing 2.6 Vol.-% of TiO_2 particles. It is noted that both TiO_2 nanoparticles have comparable primary particle sizes but show very different dispersion quality according to SEM examination.

From Figure 4.6.1, it is evident that the Al_2O_3-modified TiO_2 (15 nm) nanoparticles show much higher stiffening and strengthening effects in TPE(PBT-PTMG) than unmodified TiO_2 (21 nm) particles due to a higher effective volume fraction calculated above (0.169 Vol.-% vs. 0.102 Vol.-%). The higher effective volume fraction of TiO_2 (15 nm) particles can be attributed to a much better dispersion quality of these particles. This result indicates that the dispersibility of a particle type plays an important role in effective volume fraction and subsequently in stiffening and reinforcing effects for a polymer matrix.

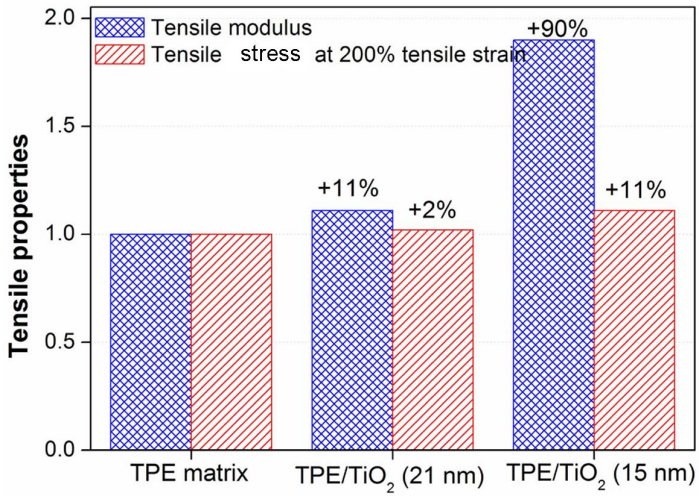

Figure 4.6.1: Comparison of tensile modulus and tensile stress between TPE(PBT-PTMG)/TiO_2 (21 nm) and TPE(PBT-PTMG)/TiO_2 (15 nm) composites containing 2.6 Vol.-% of respective TiO_2 particles.

In another case, both TiO_2 (300 nm) and TiO_2 (15 nm) particles are mainly with Al_2O_3 pre-treated. Both types of particles show very good dispersion quality in TPE(PBT-PTMG) matrix due to surface modification, but they exhibit very different primary particle sizes (300 nm vs. 15 nm). In order to investigate the influence of particle size on tensile properties of TPE(PBT-PTMG)/TiO_2 composites, the tensile results of TPE(PBT-PTMG)/TiO_2 (300 nm) and TPE(PBT-PTMG)/TiO_2 (15 nm) composites containing 2.6- and 3.8 Vol.-% of TiO_2-particles are summarized in Figure 4.6.2.

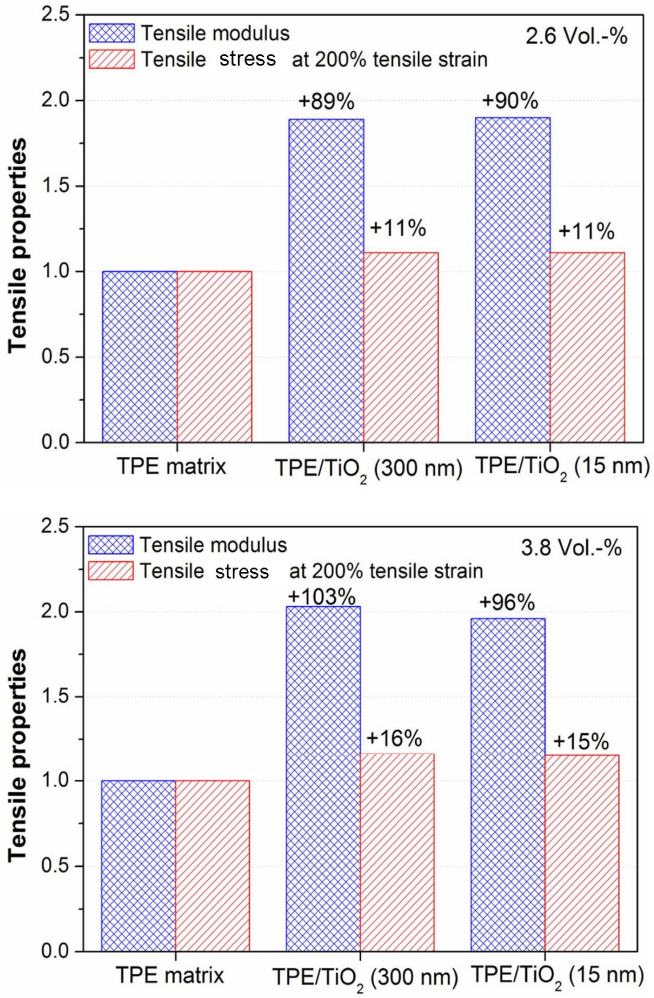

Figure 4.6.2: Comparison of tensile modulus and tensile stress between TPE(PBT-PTMG)/TiO_2 (300 nm) and TPE(PBT-PTMG)/TiO_2 (15 nm) composites containing 2.6- and 3.8 Vol.-% of TiO_2-particles.

At 2.6 Vol.-% of TiO_2-particles, both composites show comparable tensile moduli. No clear relationship between particle size and tensile modulus can be drawn because both particles reveal different effective volume fractions (0.146 vs. 0.169). However, at 3.8 Vol.-% of TiO_2-particles at which both types of TiO_2 reveal comparable effective volume fractions (0.195 vs. 0.198), the TPE(PBT-PTMG)/TiO_2 (300 nm) composite shows clearly a higher tensile modulus than the TPE(PBT-PTMG)/TiO_2 (15 nm) composite with an improvement by 7%. This indicates that larger particles show higher stiffening effect than smaller particles at similar effective particle loading.

In terms of tensile stress, both TPE(PBT-PTMG)/TiO_2 (300 nm) and TPE(PBT-PTMG)/TiO_2 (15 nm) composites exhibit comparable values to each other at the same particle loading. This indicates that both TiO_2 particles result in comparable strengthening effect in TPE(PBT-PTMG) matrix independent on particle sizes as long as both particles are well dispersed. Another explanation is that the interfacial interactions between matrix and both types of particles are similar to each other due to their surface treatment with Al_2O_3.

4.6.4 Influence of different TiO_2 particles on weathering behaviour of TPE(PBT-PTMG)/TiO_2 composites

Figure 4.6.3 shows the TPE(PBT-PTMG)/TiO_2 composites with 2.6 Vol.-% of respective TiO_2 particles. It is evident that the TPE(PBT-PTMG)/TiO_2 (21 nm) composite shows clear photodegradation cracks after 30 days exposure in air. Conversely, no evident weathering is observed in TPE(PBT-PTMG)/TiO_2 (300 nm) and TPE(PBT-PTMG)/TiO_2 (15 nm) composites under the same conditions. This can be attributed to the surface pre-treatment with Al_2O_3 of TiO_2 (300 nm) and TiO_2 (15 nm) particles. The surface pre-treatment effectively suppressed the photoactive reaction of TiO_2 particles, leading to increased weathering resistance of respective

TPE(PBT-PTMG)/TiO_2 composites.

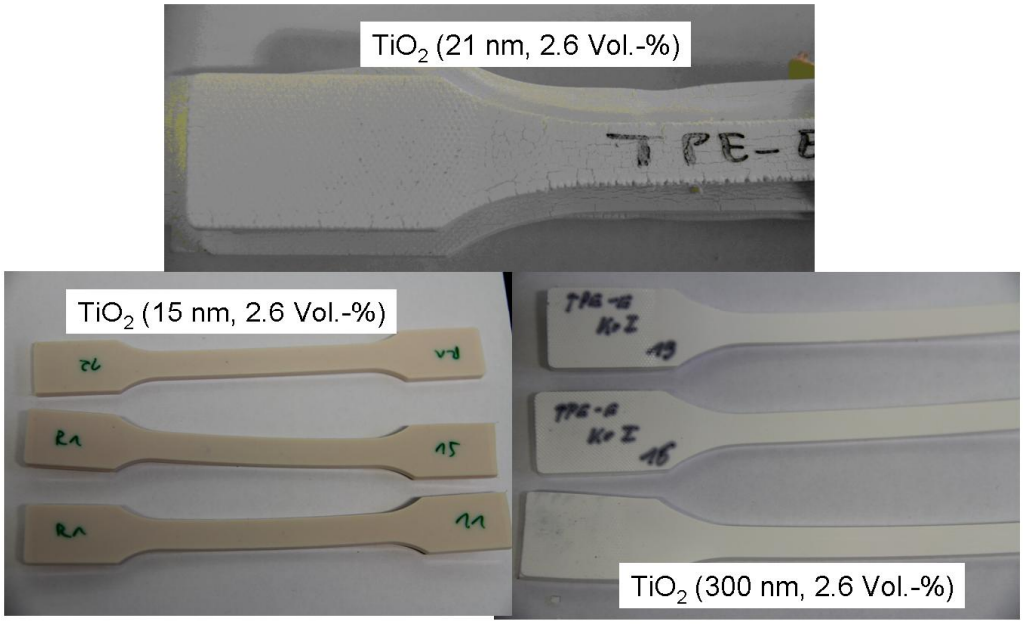

Figure 4.6.3: TPE(PBT-PTMG)/TiO_2 (2.6 Vol.-%) composites containing different TiO_2 particles show different weathering behaviour in air.

5 Summary and Outlook

In this study, a broad range of nanoparticle-filled polymer composites was investigated. The polymer composites were produced by direct melt blending in a twin-screw extruder via masterbatch method and then injection moulded. The morphological, thermal and mechanical properties of produced polymer composites were characterized and discussed. The main objective of this study was to examine the influences of particle loading, particle surface polarity, particle content and particle size as well as the chemical nature of used particles on the properties of polymer composites. According to the results obtained, the following conclusions can be drawn:

- The incorporation of octamethylcyclotetrasiloxane-modified SiO_2 (D4-SiO_2) nanoparticles into PC significantly improves overall the thermal and mechanical properties of PC/SiO_2 composites, especially the resistance against ESC in critical chemical agent toluene. The PC composite with 4 Vol.-% of D4-SiO_2 nanoparticles reveals the best results among produced PC composites. Although the light transmittance and haze of PC/D4-SiO_2 composites are deteriorated with increasing particle content, the clarity of PC composites still maintain at high level as that one of neat PC.
- The surface-modified SiO_2 and TiO_2 nanoparticles are well dispersed in iPP matrix due to increased surface hydrophobicity, which increases the dispersability and compatibility of respective nanoparticles in iPP matrix. By contrast, the

unmodified SiO_2 and TiO_2 nanoparticles with OH-groups on particle surface result in a high degree of agglomeration due to formation of hydrogen bonds among nanoparticles themselves. Among produced iPP/SiO_2 composites, the 3C1-iPP/SiO_2 composite shows the best results in dispersion quality of nanoparticles, storage modulus, fracture toughness and impact toughness due to the highest hydrophobicity of 3C1-SiO_2 nanoparticles. Increasing alkyl chain length on particle surface improves the interfacial interactions due to increased chain entanglement in matrix-particle interphase, proved by increased tensile strength of iPP/SiO_2 composites with increasing alkyl chain length. Nevertheless, the improvements in tensile strength of iPP/SiO_2 composites in this study are not significant because of the weak Van der Waals interactions. It is confirmed that the surface polarity and chemical nature of used nanoparticles have large influence on thermal and mechanical properties of iPP composites, for example, iPP exhibits much higher crystallinity in iPP/SiO_2 composites than in iPP/TiO_2 composites independent of surface modification, whereas iPP/TiO_2 composites show much higher thermal stability than iPP/SiO_2 composites at same particle loading.

- The incorporation of three TiO_2 particles with different primary particle sizes into TPE(PBT-PTMG) strongly affects the thermal and mechanical properties of TPE(PBT-PTMG) matrix due to strong chemical interactions between particles and polymer matrix. The TiO_2 (21 nm) particles show very poor dispersion quality in both iPP and TPE(PBT-PTMG) due to strong Van der Waals interactions

among particles (formation of hydrogen bonds). On the contrary, the surface pre-treated TiO_2 (300 nm) and TiO_2 (15 nm) particles are very homogenously dispersed in TPE(PBT-PTMG). Correspondingly, the TPE(PBT-PTMG)/TiO_2 (21 nm) composites reveal only slight improvements in tensile properties, whereas the TPE(PBT-PTMG)/TiO_2 (300 nm) and TPE(PBT-PTMG)/TiO_2 (15 nm) composites show much higher values of tensile modulus and tensile stress due to much better dispersion quality and subsequently larger effective volume fraction of particles in the matrix. In addition, larger TiO_2 (300 nm) particles with 300 nm primary size show higher stiffening effect in TPE(PBT-PTMG) than smaller TiO_2 (15 nm) particles, but both particles show similar strengthening effect in TPE(PBT-PTMG) due to similar surface nature and interfacial interactions with TPE(PBT-PTMG) matrix. Compared to TPE(PBT-PTMG)/TiO_2 (21 nm) composites, the TPE(PBT-PTMG)/TiO_2 (300 nm) and TPE(PBT-PTMG)/TiO_2 (15 nm) composites show increased weathering resistance due to surface pre-treatment of TiO_2 particles.

As already discussed, a big issue in this work is the very poor dispersibility of TiO_2 (21 nm) nanoparticles due to strong interactions among particles. Although the polymer composites were three times extruded via a masterbatch method, the TiO_2 (21 nm) nanoparticles show still a high degree of agglomeration in both iPP and TPE(PBT-PTMG) matrices. The presence of large agglomerates indicates that the shear forces during extrusion process were not effective enough to break them down. As a result, the large agglomerates could be the reason for

premature failures in polymer composites under imposed force, leading to decreased mechanical properties.

6 References

[1] Fornes, T. D., Yoon, P. J., Keskkula, H., Paul, D. R. (2001). Nylon 6 Nanocomposites: the Effect of Matrix Molecular Weight, Polymer, 42, 929-9940.

[2] Grigo, U., Kircher, K., Müller, P. R. (1992). Polycarbonate, in “Kunststoff Handbuch’’, 3rd ed., Hanser Verlag, München, Wien, 117-159.

[3] Domininghaus, H. (1992). Synthetische Kunststoffe, in “Die Kunststoffe und ihre Eigenschaften’’, 6th ed., VDI-Verlag, Düsseldorf, 1019-1053.

[4] Kircher, K. (2006). Herstellung der wichtigsten Kunststoffe, in “Kunststoffe: Synthese, Herstellungsverfahren, Apparaturen’’, Wiley-VCH, 181-185.

[5] N, N. (1992). Makrolon-Technische Kunststoffe, Anwendungstechnische Information, KU 46100 d, Bayer AG, Leverkusen.

[6] Chanda, M., Roy, S. K. (1998). In “Plastics Technology Handbook”, 3rd ed., Marcel Dekker, New York, 618-619.

[7] Raman, A., Farris, R. J., Lesser, A. J. (2003). Effect of stress state and polymer morphology on environmental stress cracking in polycarbonate. J. Appl. Polym. Sci., 88, 50-564.

[8] Arnold, J. C. (1995). The influence of liquid uptake on environmental stress cracking of glassy polymers. Mater. Sci. Eng., A197, 19-124.

[9] Clay, S. B., Kander, R. G. (2001). A new method to quantify crazing in various environments. Polym. Eng. Sci., 41, 01-407.

[10] Miller, G. C., Visser, S. A. D., Morecroft, A. S. (1971). On the solvent-cracking of polycarbonate. Polym. Eng. Sci., 11, 3-82.

[11] Wang, H. T., Pan, B. R., Du, Q. G., Li, Y. Q. (2003). The strain in the test environmental stress cracking of plastics. Polym. Test., 22, 5-128.

[12] Raghu, H., Bose, S., Kulkurani, M. B., Mahanwar, P. A. (2007). Effect of talc and synthetic sodium aluminium silicate on properties of polycarbonate. J. Thermoplastic Compos. Mater., 20, 345-356.

[13] Perry, D., Ward, W. J., Cussler, E. I. (1989). Unsteady diffusion in barrier membranes. J. Membrane Sci., 44, 305-311.

[14] Bosshard, A. W., Schlumpf, H. P. (1987). Fillers and reinforcements, in “Plastics Additives Handbook”, Gachter, R., Müller, H. (ed.), Hanser Publishers, München.

[15] Flores, A., Cagiao, M. E., Ezquerra, T. A., Balta, C. F. J. (2001). Influence of filler structure on microhardness of carbon black-polymer composites. J. Appl. Polym. Sci., 79, 90-95.

[16] Jancar, J. (1999), in “Minaral Fillers in Thermoplastics I”, Vol. 139: 1-65.

[17] Streller, R. C., Thomann, R., Torno, O., Mülhaupt, R. (2008), Isotactic Poly(propylene) Nanocomposites Based upon Boehmite Nanofillers, Macromol. Mater. Eng. 293, 218.

[18] Mittal, V. J. (2007), Polypropylene-Layered Silicate Nanocomposites: Filler Matrix Interactions and Mechanical Properties, J. Thermoplast. Compos. Mater. 20, 575.

[19] Yuan, Q., Wu, D. Y., Gotama, J., Bateman, S. J. (2008), Wood Fiber Reinforced Polyethylene and Polypropylene Composites with High Modulus and Impact Strength, J. Thermoplast. Compos. Mater. 21, 195.

[20] Liu, X. H., Wu, Q. J. (2001), PP/clay nanocomposites prepared by grafting-melt intercalation, Polymer 42, 10013.

[21] Nejad, S. J., Ahmadi, S. J., Abolghasemi, H., Mohaddespour, A. (2007), Thermal Stability, Mechanical Properties and Solvent Resistance of PP/clay Nanocomposites Prepared by Melt Blending, J. Appl. Sci. 7(17), 2480-2484.

[22] Vu-Khanh, T., Fisa, B. (1986), Impact fracture of glass-flake reinforced polypropylene, Polym. Compos. 7, 375-382.

[23] Zhou, H. J., Rong, M. Z., Zhang, M. Q., Ruan, W. H., Friedrich, K. (2007), Role of reactive compatibilization in preparation of nanosilica/polypropylene composites, Polym. Eng. Sci. 47, 499-509.

[24] Liang, J. Z. (2009), Impact fracture toughness and morphology of diatomite-filled polypropylene composites, Polym. Eng. Sci. 49, 1603-1607.

[25] Sarkar, M., Dana, K., Ghatak, S., Banerjee, A. (2008), Polypropylene-clay composite prepared from Indian bentonite, Bull Mater. Sci. 31, 23-28.

[26] Garcia, M., Van Vliet, G., Jain, S., Schrauwen, B. A. G., Sarkissov, A., Van Zyl, W. E., Boukamp, B. (2004), Polypropylene/SiO_2 Nanocomposites with Improved Mechanical Properties, Rev. Adv. Mater. Sci. 6, 169-175.

[27] Rong, M. Z., Zhang, M. Q., Pan, S. L., Friedrich, K. (2004), Interfacial effects in polypropylene–silica nanocomposites, J. App. Polym. Sci. 92, 1771-1781.

[28] Velasco, J. I., De Saja, J. A., Martinez, A. B. (1997), FRACTURE BEHAVIOUR OF UNTREATED AND SILANE-TREATED TALC-FILLED POLYPROPYLENE COMPOSITES, Fatigue Fract. Eng. Mater. Struct. 20, 659-670.

[29] Chan, C. M., Wu, J. S., Li, J. X., Cheung, Y. K. (2002), Polypropylene/calcium carbonate nanocomposites, Polymer 43, 2981-2992.

[30] Thio, Y. S., Argon, A. S., Cohen, R. E., Weinberg, M. (2002), Toughening of isotactic polypropylene with $CaCO_3$ particles, Polymer, 43, 3661-3674.

[31] Huang, L., Zhan, R. B., Lu, Y. F. (2006), Mechanical Properties and Crystallization Behavior of Polypropylene/Nano-SiO_2 Composites, J. Reinf. Plast. Compos. 25, 1001-1012.

[32] Zhu, L.L., Wegner, G. (1981), The morphology of semicrystalline segmented poly(ether ester) thermoplastic elastomers, Macromol. Chem. Phys., 182, 3625-3638.

[33] Cella, R. J. (1973), Morphology of segmented polyester thermoplastic elastomers, J. Polym. Sci. Symp., 42, 727-740.

[34] Phillips, R. A., Mckenna, J. M., Cooper, S. L. (1994), Glass transition and melting behavior of poly(ether-ester) multiblock copolymers with

poly(tetramethylene isophthalate) hard segments, J. Polym. Sci. B, 32, 791-802.

[35] Schmalz, H., van Guldener, V., Gabriëlse, W., Lange, R., Abetz, V. (2002), Morphology, Surface Structure, and Elastic Properties of PBT-Based Copolyesters with PEO-*b*-PEB-*b*-PEO Triblock Copolymer Soft Segments, Macromolecules, 35, 5491-5499.

[36] Stevenson, J. S., Cooper, S. L. (1988), Microstructure and property changes accompanying hard-segment crystallization in block copoly(ether-ester) elastomers, Macromolecules, 21, 1309-1316.

[37] Seymour, R. W., Overton, J. R., Corley, L. S. (1975), Morphological Characterization of Polyester-Based Elastoplastics, Macromolecules, 8, 331-335.

[38] Gabriëlse, W., Soliman, M., Dijkstra, K. (2001), Microstructure and Phase Behavior of Block Copoly(ether ester) Thermoplastic Elastomers, Macromolecules, 34, 1685-1693.

[39] Veenstra, H., Hoogvliet, R. M., Norder, B., Posthuma de Boer, A. J. (1998), Microphase separation and rheology of a semicrystalline poly(ether-ester) multiblock copolymer, Polym. Sci. B, 36, 1795-1804.

[40] El Fray, M., Slonecki, J. (1998), Influence of the chemical composition of poly[ester-*block*-ether]s on the phase structure, Macromol. Sci. Phys. B, 37, 143-154.

[41] Hagashiyama, A., Yamamoto, Y., Chujo, R., Wu, M. (1992), NMR Characterization of Segment Sequence in Polyester-Polyether Copolymers, Polym. J. Tokyo, 24(12), 1345-1349.

[42] Slonecki, J. (1992), Wpływ udziału masowego i cie_aru czasteczkowego segmentów nawarunki otrzymywania, budowe i własciwosci termoplastyczne kopoli(estroeterów) (KPEE), Polimery, 37, 19-24.

[43] Karger-Kocsis, J. (2002), in “Handbook of Condensation Thermoplastic Elastomers”, Fakirov, S. (ed.), Wiley-VCH, Weinheim.

[44] Davis, A., Golden, J. H. (1969), Stability of polycarbonate, J. Marcromol. Sci. – Revs. Marcromol. Chem., C3: 49-68.

[45] Davis, A., Golden, J. H. (1968), Thermal Degradation of Polycarbonate, J. Chem. Soc. Part B. Phy. Org., 1-7: 45-47.

[46] Streller, R. C. (2008), Boehmite als Nanofüllstoffe für Polypropylen-Nanocomposites und Nanopartikel-modifizierte Polypropylene/Kautschuk-Blends, Dissertation, Albert-Ludwigs-University Freiburg, Germany.

[47] Mcmillan, F. M. (1985), in “Applied Polymer Science”, 2nd ed., Tess, R. W., Gary, W. (ed), American Chemical Society, Vol. 285, 333–361.

[48] Ketley, A. D. (1967), in “The Stereochemistry of Macromolecules”, Marcel Dekker, New York, Vol. 1.

[49] Keij, T. (1972), in “Kinetics of Ziegler-Natta Polymerization”, Kadansha, Tokyo.

[50] Chien, J. C. W. (1975), in “Coordination Polymerization”, Academic Press, New York.

[51] Boor, J. (1979), in “Ziegler-Natta Catalysts and Polymerizations”, Academic Press, New York.

[52] Cheng, S. Z. D., Janimak, J. J., Rodriguez, J. (1985), In “Polypropylene Structure, Blends and Composites”, Karger-Kocsis, J. (ed.), Chapman & Hall, London, pp. 31-55.

[53] Kissel, W. J., Han, J. H. (1999), In “Handbook of Polypropylene and Polypropylend Composites”, Karian, H. G. (ed.), Marcel Dekker, New York, Basel, pp. 15-37.

[54] Miller, J. A., Mckenna, J. M., Pruckmayr, G., Epperson, J. E., Cooper, S. L. (1985), Chain conformation in medium- and high-ester content polyether-polyester block copolymers: a small-angle neutron scattering study, Macromolecules, 18, 1727-1736.

[55] Roslaniec, Z. (2005), In “Handbook of condensation thermoplastic elastomer”, Fakirov, S. (ed.), Wiley-VCH, Weinheim, pp 77-101.

[56] Castrovinci, A., Camino, G. (2007), Fire-Retardant Mechanisms in Polymer Nano-Composite Materials, in “Multifunctional Barriers for Flexible Structure: Textile, Leather and Paper”, Materials Science, 97, 87-108.

[57] Thostenson, E., Li, C., Chou, T. (2005), Review Nanocomposites in Context, J. Compos. Sci. Technol., 65, 491-516.

[58] Luo, J. J., Daniel, I. M. (2003), Characterization and Modelling of Mechanical Behaviour of Polymer/Clay Nanocomposites, Compos. Sci. Technol., 63, 1607-1616.

[59] Siengchin, S. (2008), Water-Mediated Melt Compounding to Produce Thermoplastic Polymer-Based Nanocomposites: Structure-Property Relationship, Dissertation, Institute for Composite Materials, Technical University of Kaiserslautern, Germany.

[60] Supaphol, S., Thanomkial, P., Junkaserm, J., Dangtungee, R. (2007), Non-isothermal melt-crystallization and mechanical properties of titanium (IV) oxide nanoparticle-filled isotactic polypropylene, Polym. Test., 26, 20-37.

[61] Kato, K., Torh, Y., Taoda, H., Kaoto, T., Butsugan, Y., Niihara, K. (1996), TiO_2 coating photocatalysts with nanostructure and preferred orientation showing excellent activity for decomposition of aqueous acetic acid, J. Mater. Sci. Lett. 15, 913-915.

[62] Gutsch, A., Krämer, M., Michael, G., Mühlenweg, H., Pridöhl, M., Zimmermann, G. (2002), Gas-Phase Production of Nanoparticles, KONA, No. 20, 24-35.

[63] Lekakou, L. et al. (2008), Processability studies of silica-thermoset polymer matrix nanocomposites. Polym. Eng. Sci., 48, 216-222.

[64] Lu, J. Z. (2003), Chemical coupling in wood-polymer composites, doctoral dissertation, Louisiana State University, Baton Rouge, LA.

[65] Ranjan, R. (2008), Surface modification of silica nanoparticles, Dissertation, University of Akron.

[66] Drzal, L. T., Rich M. J., Lloyd, P. F. (1984), Adhesion of Graphite Fibers to Epoxy Matrices: I. The Role of Fiber Surface Treatment, J. Adhesion 16, 1-30.

[67] Chappel, P. J., Williams, D. R. (1989), Determination of poly(*p*-phenylene terephthalamide) fiber surface cleanliness by inverse gas chromatography, J. Colloi. Interface Sci. 128, 450-457.

[68] Berg, J. C. (1086), in “Composite Systems from Natural and Synthetic Polymers”, Salmen, L., de Ruvo, A., Seferis, J. C., Stark, E. B. (eds.), Elsevier, New York, p. 23.

[69] Zisman, W. A. (1964), Contact Angle, Wettability, and Adhesion, Adv. Chem. Ser., 43, 1.

[70] Guggenheim, E. A. (1945), The Principle of Corresponding States, J. Chem. Phys., 13, 253-261.

[71] Wu, S. H. (1982), in “Polymer Interface and Adhesion”, Marcel Dekkar, New York, p. 70.

[72] Ehrman, S. H., Friedlander, S. K., Zachariah, M. R. (1998), Characteristics of SiO_2/TiO_2 nanocomposite particles formed in a premixed flat flame, J. Aerosol Sci., 29, 687-706.

[73] Wu, S. (1969), Surface and interfacial tensions of polymer melts: I. Polyethylene, polyisobutylene, and polyvinyl acetate, J. Colloid. Interface Sci., 31, 153-161.

[74] Wu, S. (1973), Polar and Nonpolar Interactions in Adhesion, J. Adhesion, 5, 39-55.

[75] Xu, Q. W., Leng, Y., Mai, Y. W. (1996), Injection Molding of PC/PBT/LCP Ternary in situ Composite, Polym. Eng. Sci., 36, 769-777.

[76] Fowkes, F. M. (1962), Determination of interfacial tensions, contact angels, and dispersion forces in surfaces by assuming additivity of intermolecular interactions in surfaces, J. Phys. Chem., 66, 382.

[77] Kwok, D. Y., Li, D., Neumann, A. W. (1994), Evaluation of the Lifshitz-van der Waals/Acid-Base Approach To Determine Interfacial Tensions, Langmuir, 10, 1323-1328.

[78] Eber, M. (2004), Wirksamkeit und Leistungsfähigkeit von nanoskaligen Fließregulierungsmittel. Dissertation, Universität Würzburg.

[79] Monte, S. Adhesive Solutions to the Challenges of Bonding to Low Surface Energy Surfaces, FLEXcon Industrial Park Spencer, MA 01562-2642 USA.

[80] Khaled, S. M., Sui, R. H., Charpentier, P. A., Rizkalla, A. S. (2007), Synthesis of TiO_2−PMMA Nanocomposite: Using Methacrylic Acid as a Coupling Agent, Langmuir, 23, 3988-3995.

[81] Weng, Y. X., Li, L., Liu, L., Wang, L., Yang, G. Z. (2003), Surface-Binding Forms of Carboxylic Groups on Nanoparticulate TiO_2 Surface Studied by the Interface-Sensitive Transient Triplet-State Molecular Probe, J. Phys. Chem. B, 4356-4363.

[82] Karger-Kocsis, J., Zhang, Z. (2005), Structure-Property Relationships in Nanoparticle/Semicrystalline Thermoplastic Composites, in “Mechanical Properties of Polymers Based on Nanostructure and Morphology”, CRC Press, Boca Raton, p. 559.

[83] Akelah, A., Moet, A. (1996), Polymer-clay nanocomposites: free-radical grafting of polystyrene on to organophilic montmorillonite interlayers, J. Mater. Sci., 31, 3589-3596.

[84] Wang, D., Zhu, J., Yao, Q., Wilkie, C. A. (2002), A comparison of various methods for the preparation of polystyrene and poly(methylmethacrylate) clay nanocomposites, Chem. Mater., 14, 3837-3843.

[85] Chen, G., Qi, Z., Shen, D. (2000), Shear-induced ordered structure in polystyrene/clay nanocomposites, J. Mater. Res., 15, 351-356.

[86] Siengchin, S., Karger-Kocsis, J. and Thomann, R. (2008). eXPREXX Polym. Lett., 2 (10), 746-756.

[87] Ritzhaupt-Kleissl, E., Böhm, J., Haußelt, J., Hanemann, T. (2006), Thermoplastic polymer composites for applications in optical devices, Mater. Sci. Eng., 26, 1067-1071.

[88] Willmouth, F.M. (1986), Transparency, Translucency and Gloss. In “Optical Properties of Polymers”, Meeten, G.H. (eds.), Elsevier Applied Science Publisher, London and New York, p 265.

[89] Bender, H. (1969), Kunststoffe, Vol 59, 501.

[90] Olsen, J.R., Day, D.E., Stoffer, J.O. (1992), Fabrication and Mechanical Properties of an Optically Transparent Glass Fiber/Polymer Matrix Composite, J. Comp. Mater., 26, 1181-1192.

[91] Ferry, J. D. (1980), in “Viscoelastic properties of polymers”, 3rd ed., Wiley-VCH, New York.

[92] Izer, A., Barany, T. (2010), Effect of consolidation on the flexural creep behaviour of all-polypropylene composite, eXPRESS Polym. Lett., 4, 210-216.

[93] Siengchin, S., Karger-Kocsis, J. (2006), Creep behaviour of polystyrene/fluorohectorite micro- and nanocomposites, Mocromol. Rapid Commun., 27, 2090-2094.

[94] Tajvidi, M., Falk, R.H., Hermanson, J.C. (2005), Time–temperature superposition principle applied to a kenaf-fiber/high-density polyethylene composite, J. App. Polym. Sci., 97, 1995-2004.

[95] Banik, B., Karger-Kocsis, J., Abraham, T. (2008), Flexural creep of all-polypropylene composites: Model analysis, Polym. Eng. Sci., 48, 941-948.

[96] Williams, M. L., Landel, R. F., Ferry, J. D. (1955), The temperature dependence of relaxation mechanisms in amorphous polymers and other glass-forming liquids, J. Amer. Chem. Soc., 77, 3701-3706.

[97] Palade, L. I., Verney, V., Attane, P. (1995), Time-temperature superposition and kinear viscoelasticity of polybutadienes, Macromolecules, 28, 7051-7057.

[98] Grellmann, W., Seidler, S. (2001), in Deformation and fracture behaviour of polymers, Springer-Verlag, Berlin, Heidelberg, New York, P 2-8.

[99] Kinloch, A. J., Young, R. J. (1983), in “Fracture Behaviour of Polymers”, Applied Science Publishers, Essex, UK.

[100] Lang, F. F., Radford, K. C. (1971), Fracture energy of an epoxy composite system, J. Mater. Sci. 6, 1197-1203.

[101] Rothon, R. (1995), In “Particulate-filled polymer composites”, Longman, New York.

[102] Nielsen, L. E., Landel, R. F. (1994), In “Mechanical properties of polymers and composites”. 2nd ed., Marcel Dekker, New York.

[103] Chan, C. M., Wu, J. S., Li, J. X., Cheung, Y. K. (2002), Polypropylene/calcium carbonate nanocomposites, Polymer, 43, 2981-2992.

[104] Friedrich, K., Karsch, U. A. (1981), Failure processes in particulate filled polypropylene, J. Mater. Sci., 16, 2167-2175.

[105] Arencon, D., Velasco, J.I. (2009), Fracture toughness of polypropylene-based particulate composites, Materials, 2, 2046-2094.

[106] Sumita, M., Tsukihi, H., Miyasaka, K., Ishikawa, K. (1984), Dynamic mechanical properties of polypropylene composites filled with ultrafine particles, J. App. Poly. Sci. 29, 1523-1530.

[107] Oelmüller, R., Müller, A., Meier, K. (1997), in “Teilhydrophobe Fällungskieselsäuren”, identification: DE19713316A1, Degussa AG, Germany.

[108] Razavi-Nouri, M., Ghorbanzadeh-Ahangari, M., Fereidoon, A., Jahanshahi, M. (2009). Effect of carbon nanotubes content on crystallization kinetics and morphology of polypropylene, Polym. Test. 28, 46-52.

[109] Griffth, A. A. (1920), The phenomena of rupture and flow in solids. Phil. Trans. Roy. Soc. London A, 221, 163-198.

[110] Irwin, G. R. (1957), Analysis of stress and strains near the end of a crack transversing a plate. J. Appl. Mech., 24, 361-364.

[111] Zhang, H., Zhang, Z., Friedrich, K. and Eger, C. (2006), Property improvements of in situ epoxy nanocomposites with reduced interparticle distance at high nanosilica content, Acta. Mater., 54, 1833-1842.

[112] Rinde, J. A. (1970), Poisson's ratio for rigid plastic foams, J. App. Polym. Sci., 14, 1913-1926.

[113] Miller, G. C., Visser, S. A. D., Morecroft, A. S. (1971), On the solvent-cracking of polycarbonate, Polym. Eng. Sci., 11, 73-82.

[114] Nevalainen, K., Vuorinen, J., Villman, V., Suihkonen, R., Jarvela, P., Sundelin, J., Lepisto, T. (2009), Polym. Eng. Sci., 49, 631-640.

[115] Heieh, A. J., Moy, P., Beyer, F. L., Madison, P., Napadensky, G. (2004), Polym. Eng. Sci., 44, 825-837.

[116] Ahn, S. H., Kim, S. H., Lee, S. G. (2004), Surface-modified silica nanoparticle–reinforced poly(ethylene 2,6-naphthalate, J. App. Polym. Sci., 94, 812-818.

[117] Kery, J., Friedrich, K. (1987), Fracture toughness and fatigue crack propagation of single fibre-bundle reinforced model composites, J. Mater. Sci. Lett., 6, 851-856.

[118] Yang, J. L., Zhang, Z., Zhang, H. (2005), The essential work of fracture of polyamide 66 filled with TiO_2 nanoparticles, Compos. Sci. Technol., 65, 2374-2379.

[119] Zhang H., Zhong, Z., Yang, J. L., Friedrich, K. (2006), Temperature dependence of crack initiation fracture toughness of various nanoparticles filled polyamide 66, Polymer, 47, 679-689.

[120] Yu, J. H., Wang, G. Q., Chen, J. F., Zeng, X. F., Wang, W. Y. (2007), Toughening of polypropylene combined with nanosized $CaCO_3$ and styrene–butadiene–styrene, Polym. Eng. Sci., 47, 201-206.

[121] Ismail, H., Poh, B. T., Tan, K. S., Moorthy, M. (2003), Effect of filler loading on cure time and swelling behavior of SMR L/ENR 25 and SMR L/SBR blends, Polym. Int., 52, 685-691.

[122] Yoshitsugu, M., Setsuko, I. (2001), Transparency of polymer blends, Polym. Eng. Sci., 41(11), 1987-1995.

[123] Binnewies, M., Jug K. (2000), the formation of a solid from the reaction $SiCl_4$ (g) + O_2 (g) → SiO_2 (s) + $2Cl_2$ (g), European J. of Inorganic Chem., 1127-1138.

[124] Becker, G., Witthauer, C. (1982), Moleküle- und Kristallstruktur des Lithium-bis(trimethylsilyl)-arsenids·DME, Zeitschrift für anorganische und allgemeine Chemie, 492, 28-36.

[125] Königstein, D., Jansen, M. (1996), Einkristallstrukturanalyse von Bis(trimethylsilyl)peroxid, Monatshefte für Chemie, 127, 1221-1227.

[126] Arkles, B. Hydrophobicity, Hydrophilicity and Silanes, issue 2006, Paint & Coatings Industry Magazine, Gelest Inc.,Morrisville, PA.

[127] Bagwe, R. P., Hilliard, L. R., Tan, W. H. (2006), Surface Modification of Silica Nanoparticles to Reduce Aggregation and Nonspecific Binding, Langmuir, 22, 4357-4362.

[128] Rong, M. Z., Zhang, M. Q., Zheng, Y. X., Zeng, H. M., Walter, R., Friedrich, K. (2001), Structure–property relationships of irradiation grafted nano-inorganic particle filled polypropylene composites, Polymer, 42, 167-183.

[129] Paul, S. A., Sinturel, C., Joseph, K., Gem Mathew, G. D., Pothan, L. A., Thomas, S. (2010), Dynamic mechanical analysis of novel composites from commingled polypropylene fiber and banana fiber, Polym. Eng. Sci., 50, 384-395.

[130] Ciprari, D., Jacob, K., Tannenbaum, R. (2006), Characterization of Polymer Nanocomposite Interphase and Its Impact on Mechanical Properties, Macromolecules, 39, 6565-6573.

[131] Zhou, J. P., Qiu, K. Q., Fu, L. W. (2005), The Surface Modification of ZnO and its Effect on the Mechanical Properties of Filled Polypropylene Composites, J. Compos. Mater. 39, 1931-1941.

[132] Rong, M. Z., Zhang, M.Q., Pan, S. L., Lehmann, B., Friedrich, K. (2004), Analysis of the interfacial interactions in polypropylene/silica nanocomposites, Polym. Int., 53, 176-183.

[133] Pukánszky, B., Vanes, M., Maurer, F. H. J., Vörós, G. (1994), Micromechanical deformations in particulate filled thermoplastics: volume strain measurementsm, J. Mater. Sci. 29, 2350-2358.

[134] Zhuk, A. V., Knunyants, N. N., Oshmyan, V. G., Topolkaraev, V. A., Berlin, A. A. (1993), Debonding microprocesses and interfacial strength in particle-filled polymer materials, J. Mater. Sci. 28, 4995-5606.

[135] Scheirs, J. (2000), in Compositional and failure analysis of polymers: a practical approach. John Wiley & Sons, Baffins Lane, Chichester, P 504-506.

[136] Zheng, Y. P., Zheng, Y., Ning, R. C. (2003), Effects of nanoparticles SiO_2 on the performance of nanocomposites, Mater, Lett., 57, 2940-2944.

[137] Friedrich, K. (1983), Crazes and shear bands in semi-crystalline thermoplastics, Adv. Polym. Sci., 52/53, 225-274.

[138] Ouederni, M., Philips, P. J. (1995), Influence of morphology on the fracture toughness of isotactic polypropylene, J. Polym. Sci. Part B, 33, 1312-1322.

[139] Gabriëlse, W., Soliman, M., Dijkstra, K. (2001), Microstructure and Phase Behavior of Block Copoly(ether ester) Thermoplastic Elastomers, Macromolecules, 34, 1685-1693.

[140] Banik, K., Abraham, T. N., Karger-Kocsis, J. (2007), Flexural Creep Behavior of Unidirectional and Cross-Ply All-Poly(propylene) (PURE®) Composites, Macrolmol. Mater. Eng., 292, 1280-1288.

[141] Wypych, G. (2010), in Handbook of Fillers, ChemTec Publishing, Toronto, P. 144.

[142] Braun, J. H., Baidins, A., Marganski, R. F. (1992), TiO_2 pigment technology: a review, Prog. Org. Coat., 20, 105-138.

[143] Fujii, K., Yamamoto, H., Shibata, J. (2001), Flocculation behavior of TiO_2 in aqueous solution containing hydrophilic polymers, Technol. Kansai. Univ., 43, 119-129.

[144] Grossman, R. F. (2008), in Handbook of vinyl formulating, John Wiley & Sons, New Jersey, P142.

[145] Linsebigler, A.L., Lu, G., Tates, J. T. (1995), Photocatalysis on TiO_2 Surfaces: Priciples, Mechanisms, and Selected Results, Chem. Rev., 95, 735-758.

[146] Englert, M. (2009), Einfluss mechanischer Dispergierverfahren auf Struktur und Eigenschaften duroplastischer Nanoverbundwerkstoffe, Dissertation, Technical University Kaiserslautern.

7 List of own publications

Journals

1. Zhou, R. J., Burkhart, T. (2010), Optical properties of particulate-filled polycarbonate, polystyrene, and poly/methyl methacrylate) composites, *Journal of Applied Polymer Science*, **115**, 1866-1872.
2. Zhou, R. J., Burkhart, T. (2010), Mechanical and optical properties of nanoparticle-filled polycarbonate composites, *Journal of Thermoplastic Composite Materials*, **23**, 487-500.
3. Zhou, R. J., Burkhart, T. (2010), Influence of nanoparticle loading on craze formation and crack propagation of polycarbonate in different environments, *Journal of Thermoplastic Composite Materials*, **23**, 607-621.
4. Zhou, R. J., Burkhart, T. (2010), Mechanical properties and morphology of microparticle and nanoparticle-filled polypropylene composites, *Journal of Materials Science*, **45**, 3016-3022.
5. Zhou, R. J., Burkhart, T. (2010), Polypropylene/SiO_2 nanocomposites filled with different nanosilicas: thermal and mechanical properties, morphology and interphase characterization, *Journal of Materials Science*, **46**, 1228-1238.
6. Zhou, R. J., Burkhart, T. (2010), Thermal and mechanical properties of poly(ether ester)-based thermoplastic elastomer composites filled with TiO_2 nanoparticles, *Journal of Materials Science*, **46**, 2281-2287.
7. Zhou, R. J., Burkhart, T. (2010), Influence of chemical nature and surface polarity of nanoparticles on thermal and mechanical properties of polypropylene composites, *Journal of Polymer Research*, in prepare.

Conference and symposium proceedings

1. Zhou, R. J., Schlarb, A. K. (2008), Innovative Nanocompounds für die Medizinprodukte, *IVW-Kolloquium*, September 16-17, Kaiserslautern, Germany, IVW-Schriftenreihe Band 80, p. 205.
2. Zhou, R. J., Burkhart, T. (2009), Influence of particle size and surface nature on rheology of isotactic polypropylene composites, *Bayreuth Polymer Symposium (BPS'09),* September 13-15, Bayreuth, Germany, PII 08.
3. Zhou, R. J., Burkhart, T. (2010), Thermal properties of isotactic polypropylene composites filled with nano and microparticles, *World Forum on Advanced Polymeric Materials: Polychar 18*, April 07-10, Siegen, Germany, p. 50.
4. Zhou, R. J., Burkhart, T. (2010), Struktur-Eigenschaftsbeziehungen von nanomodifizierten Thermoplasten und thermoplastischen Elastomeren, DFG GRK-814 Workshop, November 10, Maria Rosenberg, Germany.